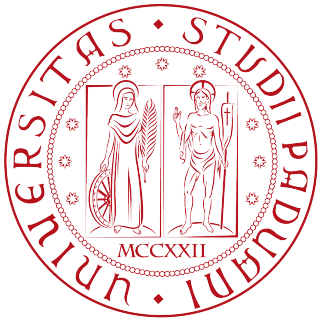

Università degli Studi di Padova

Scuola di Scienze

Dipartimento di Fisica e Astronomia "Galileo Galilei"

Corso di Laurea Magistrale in Astronomia

CO-EVOLUTION OF BLACK HOLE ACCRETION AND STAR FORMATION IN GALAXIES AT DIFFERENT COSMIC EPOCHS

CO-EVOLUZIONE DELL'ACCRESCIMENTO DEI BUCHI NERI E DELLA FORMAZIONE STELLARE NELLE GALASSIE A DIVERSE EPOCHE COSMICHE

Relatore:
Dott.ssa Giulia Rodighiero

Correlatore:
Dott.ssa Marcella Brusa

Candidato:
Rosamaria Carraro

Anno Accademico 2014-2015

Contents

List of acronyms

2dF Two Degree Field survey
ACIS Advanced CCD Imaging Spectrometer on CXO
ACS Advanced Camera for Surveys on HST
AGN Active Galactic Nuclei
ALMA Atacama Large Millimeter/submillimeter Array
ASCA Advanced Satellite for Cosmology and Astrophysics
BH Black Hole
BHAR Black Hole Accretion Rate
BHARD Black Hole Accretion Rate Density
BLR Broad Line Region
C-COSMOS Chandra Cosmic Evolution Survey
CANDELS Cosmic Assembly Near-IR Deep Extragalactic Legacy Survey
CCD Charge-Coupled Device
CDM Cold Dark Matter
CFHT Canada France Hawaii Telescope
COSMOS Cosmic Evolution Survey
CR Count Rate
CTIO Cerro Tololo Inter-American Observatory
CXC Chandra X-ray Center
CXO Chandra X-ray Observatory
ECF Encircled Counts Fraction
ESA European Space Agency
FIR Far InfraRed
FTS Fourier Transform Spectrometer
FRI and FRII Faranoff-Riley I and II radio galaxies
GALEX GALaxy Evolution eXplorer
GEMS Galaxy Evolution from Morphology and SEDs survey
GOODS Great Observatories Origins Deep Survey
HETGS High Energy Transmission Grating Spectrometer on CXO
HIFI Heterodyne Instrument for the Far Infrared on HSO
HSO Herschel Space Observatory
HR Hardness Ratio
HRC High Resolution Camera on CXO
HRMA High Resolution Mirror Assembly on CXO
HST Hubble Space Telescope
HUDF Hubble Ultra Deep Field survey
IMF Initial Mass Function
IR Infra-Red
IRAS Infra-Red Astronomy Satellite

KPNO Kitt Peak National Observatory
LETGS Low Energy Transmission Grating Spectrometer on CXO
LINER Low Ionization Nuclear Emission-line Region
LIRG Luminous Infra-Red Galaxies
LSS Large Scale Structure
MIR Medium InfraRed
MS Main Sequence
NASA National Aeronautics and Space Administration
NIR Near InfraRed
NLR Narrow Line Region
PACS Photoconductor Array Camera and Spectrometer on HSO
pBzK Passive galaxies selected with the BzK criterion
PEP PACS Evolutionary Probe
PSF Point Spread Function
QUASAR Quasi Stellar Object
RS Schwarzschild Radii
sBHAR Specific Black Hole Accretion Rate
sBzK Star-forming galaxies selected with the BzK criterion
SED Spectral Energy Distribution
SFG Star Forming Galaxies
SFH Star Formation History
SFR Star Formation Rate
SFRD Star Formation Rate Density
SIM Science Instrument Module on CXO
SMBH Super Massive Black Hole
SPIRE Spectral and Photometric Imaging REceiver on HSO
SPLASH Spitzer Large Area Survey with Hyper-Suprime-Cam
sSFR Specific Star Formation Rate
SSP Single Stellar Population
SST Spitzer Space Telescope
ULIRG Ultra Luminous Infra-Red Galaxies
UV Ultra Violet
VISTA Visible and Infrared Survey Telescope for Astronomy
VLA or JVLA Karl G. Jansky Very Large Array
VLT Very Large Telescope
XMM-Newton X-ray Multi-mirror Mission - Newton

Introduction

A causal connection between super massive black hole (SMBH, or simply BH) and galaxy growth has been suggested by a number of studies, based on empirical correlations between black hole mass and integrated galaxy properties: galaxy bulge M_*, velocity dispersion (e.g. Magorrian et al. 1998; Gebhardt et al. 2000; Ferrarese 2002; Gültekin et al. 2009). In addition, the cosmic star formation history and the black hole accretion history follow parallel evolutionary paths, peaking at $z \simeq 2$ and declining towards the local Universe (Boyle & Terlevich 1998; Shankar et al. 2009; Madau & Dickinson 2014; Delvecchio et al. 2014). A profound relationship between the history of star-forming galaxies and a concomitant activity of active galactic nuclei (AGN) BH accretion was indicated already in Franceschini et al. (1999) and later confirmed by many authors.

Despite the mutual dependence on a common cold gas supply, a connections between star formation (SF) and AGN is not trivial given the vastly different spatial scales at which star formation (many kpc) and SMBH accretion (sub-pc) typically operate. Different scenarios have been proposed to justify the necessary loss of gaseous angular momentum, such as nuclear bars, minor and major merger events (e.g. García-Burillo et al. 2005). However, the detailed mechanisms responsible for triggering black hole accretion and star formation are still poorly understood (e.g. see comprehensive review by Alexander & Hickox 2012).

While the role of violent mergers is still considered as an important triggering mechanism for BH growth (observed as AGN), in particular in very luminous quasars (Hopkins et al. 2008; Treister et al. 2012), the emerging observational framework supports the idea that secular processes are responsible for both star formation and SMBH growth in a large majority of galaxies displaying moderate nuclear activity (Cisternas et al. 2011; Kocevski et al. 2012). As such, it is now clear that processes other than galaxy mergers, such as gas turbulence or disk instabilities, play an important role in triggering BH accretion (Bournaud et al. 2012). However, with many studies finding no clear correlation between instantaneous BH growth and star formation (Silverman et al. 2009; Shao et al. 2010; Rosario et al. 2012; Mullaney et al. 2012a; Azadi et al. 2014; Stanley et al. 2015), measuring the contribution of these different triggering processes to the BH growth budget has proven a significant challenge. A key step forward in this area has been achieved by studies that have adopted X-ray stacking analyses to derive the *average* BH accretion rate (BHAR) of large samples of galaxies (i.e., including undetected, low accretion rate BHs). In doing so, these studies have demonstrated that the average BHAR is tightly correlated with both M_* and star formation rate (SFR) (Mullaney et al. 2012b); Chen et al. 2013) and mimics the SFR-M_* relation of normal star-forming galaxies (Elbaz et al. 2007; Daddi et al. 2007; Rodighiero et al. 2014, 2015). These apparently contradictory results have been interpreted by Hickox et al. (2014) as due to different variability time scales between nuclear activity and SF. According to this scenario, both components are intimately connected at any time: while star formation is relatively stable over $\sim$ 100 Myr, the AGN might vary over $\sim$ 5 orders of magnitude on very short (about 105 yr) time scales (Hickox

et al. 2009; Aird et al. 2012; Bongiorno et al. 2012). All episodes of star formation are accompanied by SMBH growth, but only when smoothing over the variations of individual sources the average properties of AGN and their hosts do show a consistent evolution, as stated by Mullaney et al. (2012b).

Up to now, few studies have discriminated between different types of galaxies, whereas it is known that different levels of SFR are triggered by different events (mergers vs secular processes for starburst and normal star-forming galaxies) which may also trigger different levels of BH growth. The interesting result found is that starburst galaxies show higher levels of BHAR with respect to normal SF galaxies at fixed M_* (Delvecchio et al. 2014; Rodighiero et al. 2015). By contrast quiescent galaxies show a deficit in BHAR (Rodighiero et al. 2015).

In the first part of this thesis work we take advantage of new Chandra X-ray *COSMOS-Legacy* (Civano et al. in prep.) survey which allows to exploit the unique depth/area combination of the COSMOS field (Scoville et al. 2007) in its entirety to extend the analysis performed in Rodighiero et al. (2015) at $z \sim 2$ to higher statistics and we confirm their results. In the second part we also take advantage of the new COSMOS2015 catalogue (Laigle et al. in prep), comprising the new UVista Ultra-deep observations in COSMOS. This allows to make an analysis in a broad redshift interval with unprecedented statistics. Our results support the idea that the same secular processes feed and sustain both SFR and BHAR from the galaxies' gas reservoirs and show that the BH accretion process is more efficient than the SF.

In chapter 1 we describe the physical context in which our analysis is inserted. Starting from the description of fundamental physical quantities such as the stellar mass (M_*), the SFR and the important relation between them, the "main sequence of star-forming galaxies" (MS). In the second part, we discuss the properties of different AGN classes in the picture of the unified model. Finally, we report a brief discussion of the principal issues concerning the interactions between AGN and host galaxy. In chapter 2 we introduce the COSMOS survey, the main instruments with which the observations were led, the catalogs used and the sample selection. In chapter 3 we introduce the X-ray data: the X-ray telescope Chandra, its observations in COSMOS and the tool for stacking, CSTACK. In chapter 4 we perform the first part of the work, extending the analysis of Rodighiero et al. (2015) on the entire COSMOS field. With doubled statistics we confirm the previous results for the three subsamples of galaxies and we are able to state that the hardness ratio is compatible between the MS and the starburst subsample, implying that starburst galaxies are on average, as obscured as the MS ones. In chapter 5 we report the main results of this thesis, which are performed with the COSMOS2015 catalogue sample. We confirm the $L_X - M_*$ relation—analogous to the SFR–M_* relation—at all considered redshifts and that the quiescent galaxies have a lower X-ray luminosity. Then we focus our attention on the SF sample, we estimate its SFR and study the co-evolution of galaxy and BH growth. We find that their trends are very similar, even though we find a M_* dependence in the BHAR/SFR ratio, suggesting that the BH accretion efficiency is higher. We find this result in the evolution of sSFR and sBHAR too, and here we find evidence for the downsizing of BH accretion and SF. This implies that more massive galaxies (BH) accrete most of their mass at early cosmic epoch, while low mass galaxies' (BHs') accretion is less time dependent. Finally in chapter 6 we report the future prospects of this work, which would allow to make these results more solid and to get new insights into this field.

Chapter 1

Star formation and AGN activity

When the star formation rate (SFR) and the central super-massive black hole accretion rate (BHAR) of a galaxy reach appreciable values, they enter the regime of the so called "active galaxies".

The rapid accretion of the super massive black hole (SMBH or simply BH) in the core of the galactic center, that defines an active galactic nucleus (AGN), is usually observable at various wavelengths, since it involves, directly or indirectly, a large number of physical mechanisms. Nowadays, the differences among AGNs showing different observational characteristics are explained in the context of the unified model (Rowan-Robinson 1977; Antonucci 1984; Antonucci & Miller 1985; Antonucci 1993; Urry & Padovani 1995), as due to the orientation with respect to the observer.

During the secular evolution of a galaxy, its SFR seems to be regulated by a simple empirical relation: the bigger the galaxy is, in terms of stellar mass M_*, the higher the SFR is. This law, usually referred to as main sequence (MS) of star-forming galaxies (Brinchmann et al. 2004; Elbaz et al. 2007; Daddi et al. 2007; Noeske et al. 2007a; Rodighiero et al. 2014), seems to be valid for local as well as for distant galaxies, for a wide range of stellar masses, and considering different SFR tracers. A galaxy can be considered as "active" by the point of view of the star formation, when its SFR is consistent or higher, than that of the main sequence. A galaxy is then "passive" (or equivalently "quiescent") when the SFR is very low or absent. This is a common case among red elliptical galaxies. At the opposite side of the main sequence, a special class of SFG is represented by the so called "starbursts", which show SFRs even ten times, or higher than that of the main sequence. These rare objects, represent a very peculiar and still not well known phase of galaxy evolution. Their role in the star formation rate density (SFRD), at the peak of the cosmic star formation ($z \sim 2$) seems to be secondary (Rodighiero et al. 2011). This means that the majority of the stars were formed during the secular evolution of the galaxies. However, this does not clarify how and why a phase of enhanced SFR can appear during the lifetime of a galaxy. What is the role played by the AGN activity during this phase? Is it responsible for the successive quenching of the star formation activity? These questions bring us to the contents of this chapter, that is a review of the main issues concerning the star formation, the AGN activity and their interconnections.

1.1 Stellar masses and star formation rates

The study of star formation properties, such as the relation between SFR and stellar masses M_* and the specific SFR (sSFR = SFR/M_*) is fundamental to understand the process of galaxy formation and evolution.

We will better describe the observed relation between stellar mass and SFR below. Before going on, we need to better clarify the meaning of stellar mass. The total mass of gas burnt into stars from the the epoch of the formation of the galaxy to its age t_z corresponds to the integration of the SFR over these two extremes:

$$M_{\rm SFR}(t) = \int_0^{t_z} \dot{M}_*(t')\ {\rm d}t' \tag{1.1}$$

To obtain the mass contained at any epoch into still surviving stars and dead remnants, it is necessary to subtract the mass of gas $M_{\rm loss}(t')$ returned to the interstellar medium from stars at any epoch t'.

$$M_*(t) \equiv M_{\rm star}(t) = \int_0^{t_z} \dot{M}_*(t')\ {\rm d}t' - \int_0^{t_z} \dot{M}_{\rm loss}(t'){\rm d}t' \tag{1.2}$$

Finally, to obtain the mass that at any epoch is contained into still surviving stars, we have to subtract the mass of the remnants $M_r(t)$:

$$M_{\rm alive}(t) = \int_0^{t_z} \dot{M}_*(t')\ {\rm d}t' - \int_0^{t_z} \dot{M}_{\rm loss}(t'){\rm d}t' - M_r(t) \tag{1.3}$$

The stellar mass $\rm M_*$ expressed in Equation (1.2) is the most common definition adopted in literature and in the following we will always refer to this definition. The stellar mass $\rm M_*$ of a galaxy is often computed through a spectral energy distribution (SED) fitting procedure. In these cases The photometric data are fitted using template spectra derived from single stellar population (SSP) synthesis models (e.g. Bruzual & Charlot 2003; Maraston 2005; Maraston et al. 2009).

The stellar mass resulting from a SED fitting also depends on the IMF, that specifies the mass distribution of the newly formed stars:

$$\phi(\log m) = \frac{d\,(N/V)}{d\log m} = \frac{dn}{d\log m} \tag{1.4}$$

where n represents the stellar numerical density and is expressed in units of [$\rm pc^{-3}$]. The IMF is usually represented by a power law:

$$\phi(m) = \phi_0 M^{-(1+x)} \tag{1.5}$$

This power law is usually defined in a specified range of mass, such as e.g. M_1=0.1$\rm M_\odot$ and M_2=125$\rm M_\odot$ for the Salpeter (1955) IMF, for which x=1.35. The IMF has a rapidly decreasing cut above the characteristic mass M_2. Other commonly used IMFs are the Chabrier (2003), and the Kroupa (2001).

The effects of using a Salpeter (1955) or a Chabrier (2003) IMF on the computed stellar masses and SFR can be quantified through a constant correction (Santini et al. 2012b; Béthermin et al. 2013)

$$\log(\rm M^*_{Chab}) = \log(M^*_{Salp}) - 0.24 \tag{1.6}$$

$$\rm M^*_{Chab} = M^*_{Salp}/1.74 \tag{1.7}$$

$$\log(\rm SFR^*_{Chab}) = \log(SFR_{Salp}) - 0.24 \tag{1.8}$$

$$\rm SFR^*_{Chab} = SFR_{Salp}/1.74 \tag{1.9}$$

1.2 Normal star-forming galaxies, starbursts and the main sequence of star-forming galaxies

Approaching the observed relation between stellar masses and SFR from a historical point of view can help to understand why, for example, a simple classification based on the luminosity of the galaxies is not enough to describe the physics behind the galaxy evolution. This approach also helps to define some general properties that allow to better understand the overall physical picture. The first identification of starburst sources dates back to the studies of Rieke & Lebofsky (1979) and Weedman et al. (1981). The interest in these sources increased during the 80s thanks to the discovery of a large population of IR ultra luminous starburst galaxies (ULIRGs) by the Infrared astronomy satellite (IRAS). We can refer to starburst galaxies as those systems with a so high SFR that it cannot be sustained for their entire lifetime (Weedman et al. 1981; Harwit & Pacini 1975). Compared with a common spiral galaxy, starburst galaxies show SFRs even two or three orders of magnitude higher. Given their mass they would be able to sustain such a high rate of star formation only for $10^7 - 10^8$ years. In the local universe, starbursts may be the result of major mergers (Sanders & Mirabel 1996). They are commonly associated with gas-rich discs galaxies with a concentration of molecular gas in the central Kpc, where the starburst activity takes place, that can be compared to the stellar densities in ellipticals (Bryant & Scoville 1999; Downes & Solomon 1998).

At high redshifts, it is quite common to observe galaxies actively forming stars with SFRs of the order of hundreds of $M_\odot$/yr, which are caught during their secular evolution. In the local Universe, galaxies with such a high SFR are instead quite rare and represent a transitory starburst phase. Following the definition of Sanders et al. (1988), both the local starbursts and the distant secularly evolving galaxies can be classified as "ultra-luminous infrared galaxies" (ULIRGS), having luminosities $L_{IR} > 10^{12}\,\mathrm{erg\,s^{-1}}$. Therefore this simple definition cannot represent the overall evolutionary picture in which galaxies evolve. For analogy with the local galaxies, the distant ULIRGS were first classified as starburst as well, until new studies begun to delineate the new physical evolutionary properties of the cosmic star formation. The major growth of galaxies, in terms of stellar masses, is observed between $z \sim 1$ and $z \sim 3$ (Dickinson et al. 2003; Rudnick et al. 2003). Using K20 survey spectroscopic data (Mignoli et al. 2005), Daddi et al. (2004) found that a reddening independent and relatively clean selection of massive galaxies at $z \sim 2$ can be obtained by selecting outliers in the $(B - z)$ versus $(z - K)$ diagram (see section 2.3.1). Following this selection criterion, Daddi et al. (2005) found that more than the 80% of a *BzK* mass selected sample of $z \sim 2$ galaxies have to be considered ULIRGs. Despite their luminosities, $z \sim 2$ galaxies could not be at the same time and altogether in the transient starburst phase. As resulting from the observations, the high SFRs measured were not an exception at high redshifts and, for this reason, their values were more probably related to the secular evolution than to a transient phase.

This picture was indeed confirmed when the existence of a tight correlation between SFR and stellar mass M_* was discovered both at low (Brinchmann et al. 2004) and at high redshifts (Elbaz et al. 2007; Daddi et al. 2007; Noeske et al. 2007a). This relation represents the so called Main sequence of the star-forming galaxies, mathematically expressed as:

$$\mathrm{SFR} = f(z) \cdot M_*^{1+\beta} \tag{1.10}$$

The observed dispersion is around 0.3 dex. In the previous equation, $1 + \beta$ represents the slope of the relation in the logarithmic plane, at a given redshift, while $f(z)$ is a an increasing function of the redshift that following Sargent et al. (2012), can be described

as:

$$f(z) = (1+z)^{2.8} \tag{1.11}$$

Thanks to the previous equations, the preponderant fraction of high redshift galaxies with high SFRs can be explained in the context of a secular evolution regime rather than by a transient phase. In Figure 1.1 we report the main sequence computed at $z \sim 2$ using different SFR indicators (Rodighiero et al. 2014).

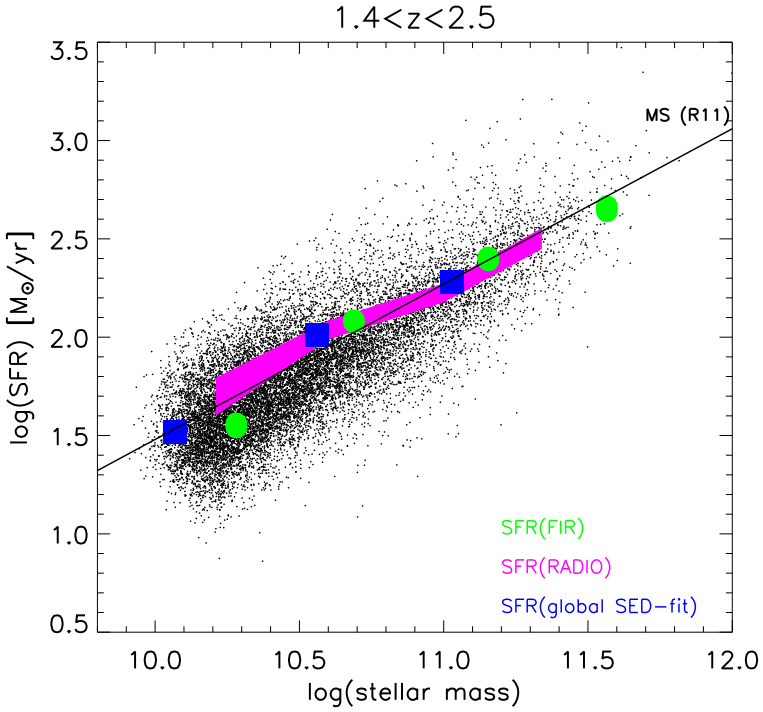

Figure 1.1: Main sequence of star-forming galaxies as computed at $z \sim 2$, using different SFR indicators. Black points represent SFRs computed using the ultra-violet (UV) emission as SFR indicator Rodighiero et al. (2014), the magenta shaded region corresponds to SFRs from stacked radio data Karim et al. (2011), the green data points refer to stacked far-IR based SFRs (*sBzK* selection) and the blue squares results from a global SED fit applied to *sBzK* selected data (Magdis et al. 2012). This image is taken from Rodighiero et al. (2014).

The existence of this main sequence has several implications on the cosmic evolution. First of all, it allows to better define the starburst phase: the observed high SFR, high redshift galaxies are not starbursts but normal galaxies in a steady evolution. At any redshift, the starburst phase is better identified by the sSFR than by the total luminosity, as it is for the ULIRG definition. The logarithmic distribution of galaxies' SFR at fixed M_*, can be described by a Gaussian curve, with starbursts representing a deviation, visible at high SFRs, from this behaviour. At the peak of the cosmic star formation ($z \sim 2$), considering SFRs four times above the main sequence value, the starbursts represent the 2% of a total mass selected sample of galaxies and the 10–15% of the cosmic SFRD. Again, the numerical fraction of these outliers seems to be more or less stable between $0 < z < 2$ (Rodighiero et al. 2011; Sargent et al. 2012; Schreiber et al. 2015). The cosmic star formation is mainly fueled by a steady accretion of material (Dekel & Birnboim 2006; Daddi et al. 2007; Dekel et al. 2009; Lilly et al. 2013), rather than by catastrophic major mergers of gas-rich galaxies that represent very vigorous but short-lived episodes of star

formation.

This sSFR based definition of the starburst systems complements the differences in the IR (∼3–500µm) SEDs between secularly evolving and starburst galaxies observed at $0 < z < 2.5$ (Elbaz et al. 2011), and the different efficiency with which the two classes of objects convert molecular gas into stars (Daddi et al. 2010a; Genzel et al. 2010). All these peculiarities give rise to the notion of "bimodal" star formation.

The inclination $1 + \beta$ of the main sequence is indeed an important factor in the evolutionary context. With $\beta = 0$, all star-forming galaxies have the same sSFR, meaning a star formation rate directly proportional to the stellar content of a galaxy; in this case the fractional growth of galaxies would not depend on the stellar mass. The observed value of β ranges from shallow slopes such as $\beta \sim 0.1$ (Elbaz et al. 2007; Daddi et al. 2007; Dunne et al. 2009; Peng et al. 2010) or $\beta \sim 0.2$ (Rodighiero et al. 2011), to steeper values as $\beta \sim 0.4$ (Noeske et al. 2007b; Karim et al. 2011). This inclination parameter regulates the differential growth of high mass galaxies versus low mass ones and then the galaxy mass (in stars) function. However, the importance of this parameter is even greater, for it is responsible of the slope of the stellar mass function inside single galaxies (Peng et al. 2014; Lilly et al. 2013).

Nowadays, the existence of the main sequence is widely accepted. There remain however some differences in the slope (as we saw above) and width values reported in literature. These differences can depend on many issues. First of all, the sample selection. Given the direct relation between FIR and SFR (Kennicutt 1998), selecting galaxies in a FIR band introduces a Malmquist bias, so that only galaxies with above-average SFRs are observable at the lowest masses. The resulting effect is a flattening of the main sequence. This is indeed observed when using *Herschel* selected samples, as in Rodighiero et al. (2010, 2011); Reddy et al. (2012). The same flattening effect is observed when the selection is performed in a UV band. As for the FIR selection, the UV luminosity, at the neat of the extinction, is directly correlated to the SFR (Kennicutt 1998). The result of an UV/optical selection is an almost flat SFR selection. This is what happens for example in Reddy et al. (2006) or in Erb et al. (2006) where no correlation between stellar mass and SFR was found ($1 + \beta = 0$), for a spectroscopic sample of UV-selected galaxies at $z \sim 2$.

The MS parametrization differences observed among various literature works can also depend on the SFR estimator used (see Section 1.3). As demonstrated in Stringer et al. (2011), little errors in the conversion from observables to physical quantities, and no corrections for the selection biases are responsible for misrepresentations of the main computed parameters (M_* and SFRs) and finally, of the main sequence. Whitaker et al. (2012) found differences in the slope of the main sequence, when considering a whole sample of star-forming galaxies and when selecting blue galaxies only. The latter selection removes the red, dusty star-forming galaxies causing a steepening of the main sequence's slope.

1.3 SFR indicators

There are many ways in which the SFR can be inferred from the integrated light emitted by a galaxy. Calibrations of SFR indicators have been presented in the literature for almost 30 years, derived across the full electromagnetic spectrum, from the X-ray, through the ultraviolet (UV), via the optical and infrared (IR), all the way to the radio, and using both continuum and line emission. Extensive reviews of this topic are reported in (e.g., Kennicutt 1998; Kennicutt & Evans 2012; Vattakunnel et al. 2012). The basic goal is to identify emission that probes newly or recently formed stars, while avoiding as much as possible contributions from evolved stellar populations.

In unresolved systems, SFR indicators are merely measures of luminosity, either monochromatic or integrated over some wavelength range, with the goal of targeting continuum or line emission that is sensitive to the short-lived massive stars. The conversion from the luminosity of massive stars to a SFR is performed under the assumption that: (1) the star formation has been roughly constant over the time-scale probed by the specific emission being used; (2) the stellar IMF is known (or is a controllable parameter) so that the number of massive stars can be extrapolated to the total number of high+low mass stars formed; and (3) the stellar IMF is fully sampled, meaning that at least one star is formed in the highest-mass bin, and all other mass bins are populated accordingly with one or more stars.

SFR indicators in the UV/optical/near-IR range (∼0.1–5 µm) probe the direct stellar light emerging from galaxies, while SFR indicators in the mid/far-IR (∼5–1000 µm) probe the stellar light reprocessed by dust. In addition to direct or indirect stellar emission, the ionising photon rate, as traced by the gas ionised by massive stars, can be used to define SFR indicators; photo-ionised gas usually dominates over shock-ionised gas in galaxies or large structures within galaxies (e.g., Calzetti et al. 2004; Hong et al. 2011). Tracers include hydrogen recombination lines, from the optical, through the near-IR, all the way to radio wavelengths, forbidden metal lines, and, in the millimetre range, the free-free (Bremsstrahlung) emission. The X-ray emission produced by high-mass X-ray binaries, massive stars, and supernovae can also, in principle, be used to trace SFRs. Finally, the synchrotron emission from galaxies can be calibrated as a SFR indicator (Condon 1992), since cosmic rays are produced and accelerated in supernova remnants, and core-collapse supernovae represent 70% or more of the total supernovae in star-forming galaxies (Boissier & Prantzos 2009).

1.3.1 UV light

The IMF of a newly formed population of stars is numerically dominated by the low mass stars. Also the fraction of integrated mass represented by high mass stars is marginal. However, massive stars dominate the emission at UV wavelengths. This remains true for the whole lifetime of this class of stars, i.e. for less than 1 Gyr.

Obscuration is, in general, the principle drawback for the SFR measurements based on all the UV emission. Extinction is stronger in the UV range of the spectra and even small amounts of dust can suppress the UV emission. The SFR can be determined only after correcting for the absorption effects.

The SFR value can be obtained from the FUV luminosity using a direct correlation:

$$\mathrm{SFR} = K_{\mathrm{FUV}} \times L_{\nu}(\mathrm{FUV}) \tag{1.12}$$

with K_{FUV} depending on the IMF, metal enrichment and star formation histories. The wavelength (e.g. 1500Å, 2300Å or 2800Å) has few importance. The original and widely used conversion factor proposed by Kennicutt (1998) is $K_{\mathrm{FUV}} = 1.4 \times 10^{-28}$.

In order to correct for the dust extinction, the UV spectral slope can be used. For example, the Calzetti et al. (2000) extinction law can be used to derive such attenuation.

1.3.2 IR emission

The UV light absorbed by dust in the star-forming regions and in the diffuse gas is re-radiated at longer wavelengths, in the mid and far-IR. Since the light absorbed by dust at IR wavelengths is negligible, the total infrared emission (usually considered between 8 and 1000µm) can be considered important tracer of ongoing SFR. Beside the older stellar

populations, that mostly contribute in older galaxies with lower SFRs (and therefore especially in the near universe), another source of contamination is represented by the AGN torus emission. As we will see in section 1.4, the dusty torus surrounding the accretion disk is responsible for a light reprocessing similar to that involving the star formation (SF) activity. The high energy radiation emitted by the inner regions of an AGN are absorbed by the dusty torus and re-emitted at MIR and FIR wavelengths. For the most star-forming galaxies, with emissions not dominated by the AGN contribution, the total IR light can be assumed, with good approximation, as directly related to the SFR.

Apart for low mass stars and AGN contamination, the total IR emission is the result of different components. Most of the dust in a galaxy is cold (15–60 K) and is responsible for the emission between 30 and 1000 µm. Other components with lower temperatures, as in the interstellar medium (ISM) or with higher temperature as in the SF regions are also present. Below 30 µm, the IR emission is dominated by the warm component in the star-forming regions. This is a complicated range of the spectrum, since spectral features due to polycyclic aromatic hydrocarbons (PAH) emission and silicate absorptions are also present. The silicate absorption is observed both in presence of AGN and in nuclear starburst regions, while the strength of the PAH features strongly depend on the ISM metallicity and field intensity (Smith et al. 2007; Engelbracht et al. 2005, 2008). The AGN contamination in this region is higher than elsewhere and can dominate over the SF component. This spectral region is well sampled, through cosmological distances, by instruments such as *Spitzer*-MIPS, at 24 µm or the IRC instruments of the *Akari* space observatory. Given the complexity of this spectral region, the SFR cannot simply be deduced from the total MIR luminosity, since more information about the type of the galaxy is needed for this conversion. The FIR emission does not present such problems and it is more directly related to the SFR. This region has been explored by the *Herschel space observatory*, thanks to its instruments, PACS and SPIRE, that cover the spectral range between 100 and 500 µm (see section 2.2.1).

As for the UV derivation, the SFR can be derived from the total IR emission using a direct correlation:

$$\mathrm{SFR_{IR}} = K_{\mathrm{IR}} \times L_{\mathrm{IR}} \tag{1.13}$$

where L_{IR} is the total IR luminosity, integrated over the 8–1000 µm range, expressed in units of [erg $\mathrm{s^{-1}}$]. Following Kennicutt (1998) and considering a Salpeter (1955) IMF, $K_{\mathrm{IR}} = 4.5 \cdot 10^{-44} \mathrm{M_\odot\,yr^{-1}\,erg^{-1}\,s}$. In this equation, as described above, the total IR luminosity is completely ascribed to the dust reprocessed light originally emitted by young massive stars and therefore to the instantaneous star formation activity. The contribution of a possible AGN torus emission or the light emitted by less massive stars is not kept into account. Another drawback of this equation is that all the UV emission is considered as absorbed by the dust. This is however a good approximation for starburst galaxies, for which this formula was presented by Kennicutt (1998). For the other cases, alternative equations where presented, for example in Papovich et al. (2007) or in Santini et al. (2009), where the UV light and the FIR total emission where complementary considered as follows:

$$\mathrm{SFR_{tot}} = K_{\mathrm{IR}} \cdot L_{\mathrm{IR}} + K_{\mathrm{FUV}} \cdot L_{\mathrm{FUV}} \tag{1.14}$$

In this case, L_{FUV} is the total FUV luminosity without an absorption correction, expressed in [$\mathrm{L_\odot}$] or in [erg $\mathrm{s^{-1}}$ $\mathrm{Hz^{-1}}$]. The values computed in Madau & Dickinson (2014) for the proportionality constants are $K_{\mathrm{FUV}} = 1.3 \times 10^{-28} \mathrm{M_\odot\,yr^{-1}\,erg^{-1}\,s\,Hz}$ and K_{IR} is the value proposed by Kennicutt (1998) of $K_{\mathrm{IR}} = 4.5 \times 10^{-44} \mathrm{M_\odot\,yr^{-1}\,erg^{-1}\,s}$.

1.4 AGN Activity

In this section we briefly describe the main characteristics of AGNs, in order to present the final and, for our purposes, most important introductory section, that refers to the interaction and co-evolution between AGNs and actively star-forming galaxies.

Active galactic nuclei are the ensemble of physical and observational phenomena that occur at the very center of galaxies and ascribable to the presence of a SMBH accreting matter at high rates. Their emission encompasses the whole electromagnetic spectrum and cannot be explained by stars, gas and dust alone, the presence of a SMBH is therefore required. Luminosity variability measurements allow to determine the size of these sources that are not bigger than few parsecs. AGNs are the most powerful emitting sources in the universe and for quite a long time, they were the only kind of source that was detectable at high redshifts. Nowadays, they represent one of the important mechanisms, together with the SF, that seem to drive the evolution of galaxies and the environment in which they evolve.

An overall explanation of such objects required almost a century, from the first spectroscopic observation of the "NGC 1068 spiral nebula", carried out by Fath (1909), that showed a peculiar spectrum with both emission and absorption lines, to the unified model presented by Urry & Padovani (1995), widely accepted today. The wide taxonomy used to describe AGNs is indicative of the vast amount of observational differences that these objects show. Many of them are now well represented by inclination effects in the context of the unified model, but it took long time before beeing able to relate Seyfert galaxies and quasars as the same type of objects. Nowadays, while the nature of AGNs and the unified model used to explain them as the same physical mechanism are widely accepted, the structure of the emitting regions and the reasons for which the AGN phenomenon appears in some galaxies rather than in others are still debated.

1.4.1 AGN properties

In this section we summarize the common peculiarities that characterize the majority of the AGNs. This will allow to introduce the differences, that we will present in the following section, as different expression of the same underlying mechanism. The common characteristics will be presented in a schematic list, in order to give a more clear overview of the physical and observational picture.

High bolometric luminosity

The bolometric luminosity of an AGN is not an easy physical quantity to be computed. Many AGNs are strongly obscured by the dust in the surrounding toroidal structure and they can be sometimes fainter than the host galaxy, making their detection extremely difficult. It seems however that the most luminous sources are as bright as 10^{48} erg s^{-1}, while for the faintest, a minimum of 10^{42} erg s^{-1} is observed. The total luminosity is the combination of a "primary" emission, that is directly observed, and a "secondary" emission, represented by the light absorbed by the toroidal dusty structure and then re-emitted in the infrared.

Small physical size compared to the host galaxy

AGNs represent, as the name says, the nuclei of their host galaxies, occupying the few inner parsecs. For optically resolved galaxies, this results in a correspondent small angular size, compared to the extension of the outer parts of the galaxy. In some cases, the brightest

nuclei can overwhelm the surface brightness of the galaxy which otherwise would not be detected, being below the flux limit of the observations.

Emission lines

AGN spectra are characterized by intense emission lines, among which the Ly$-\alpha$ line, the Balmer series, the CIV pair at 1549 Å the [OIII] line at 5007 Å the K_α Fe line at 6.4 KeV (Padmanabhan 2002). The most important distinction is based on the line width, which corresponds to a different velocity field of the emitting region. Broad lines are emitted in the inner regions and given the high velocity field ($\sim 10^3 \div 10^4$ Km/s) they show an important Doppler effect enlargement. Narrow lines are emitted in regions characterized by lower velocity fields ($\sim 10^2$ Km/s). Both permitted and forbidden lines are observed, but these last ones are more commonly observed with a narrow profile.

Wide multi-band emission

In an AGN, many thermal and non-thermal mechanisms interplay to create the final observed spectrum of these sources. The continuum emission spans from the gamma domain to the radio bands and sometimes without strong discontinuities. A typical galactic spectrum is instead the result of combined black body emission at different characteristic temperatures. However, neither stars nor dust emit in a range wider than an order of magnitude in frequency (Padmanabhan 2002).

In the **radio** wavelengths, AGN taxonomy refers to radio "quiet" and radio "loud" sources. In the first case, the radio spectrum is the continuation, at longer wavelengths, of the FIR thermal emission peak due to the dust (sub-mm break). Only ∼10% of AGNs belong to the second category. In this case, the strong radio emission observed is emitted by a compact radio source and by an extended structure, referred as "radio lobes" that depart from the compact object. In both cases, the radio luminosity is due to synchrotron emission of accelerated charges (Beckmann & Shrader 2012). The synchrotron emission by a homogeneous source with a constant magnetic field can be described by a power law:

$$F_\nu \propto \nu^{-\alpha} \tag{1.15}$$

with F_ν in units of erg s^{-1} cm^{-2} Hz^{-1} and $\alpha = (s-1)/2$ derived from the electron energy distribution:

$$N(E)dE = N_0 E^s dE \tag{1.16}$$

Typically, for the lobe emission and at high frequencies $\alpha \sim 0.7$, while at lower frequencies $\alpha \sim 5/2$ (Peterson 1997). For a compact source, $\alpha < 0.5$.

In the **infrared**, the AGN's spectrum is dominated by dust emission between 1 and 300 µm. This thermal emission is due to the dusty torus surrounding the central engine which is eaten by the high energy radiation and re-emits at longer wavelengths causing the observed black body type emission. In the radio loud sources, this wavelength range can be still dominated by synchrotron emission. the dusty torus, is also responsible for the PAH and silicate emission and absorption lines that contribute to the spectral shape between 5 and 24 µm.

In the **optical** bands, the observed spectrum strongly depends on the inclination of the object (following the unified model of Urry & Padovani 1995, see section 1.4.2). If the dusty torus inclination allows to observe the inner regions, the optical continuum shows a power law spectrum and an emission that increases towards the UV. The Fe emission line and the Balmer continuum creates the so called "small blue bump", in contrast with the

more important "big blue bump" observed in the UV. This spectral shape makes AGNs "bluer" than inactive galaxies. Important emission lines such as the Ly$-\alpha$, Balmer series, Helium, Carbon and Magnesium lines, are emitted in regions spatially close to the central engine, where the Doppler effect due to the strong velocity field makes them broad. Other narrow lines are instead emitted in more distant and colder regions, where the Doppler effect is less effective. No important variability is observed in these regions.

The **UV** emission is characterized by the continuation of the increasing optical spectrum. The emission shows a peak, the so called "big blue bump" thought to be associated with the thermal emission of the accretion disk at the very center of the AGN structure (Shields 1978), where the temperature reaches values of $10^4 \div 10^5$ K (Beckmann & Shrader 2012). The measured emission lines provide a high precision measure of the inner region dynamics.

At the **X-ray** wavelengths, between 10^2 to 10^5 eV, the physical mechanism responsible of the emission is the black hole accretion process (see also section 1.5.1). The UV photons emitted in the accretion disk gain energy through inverse Compton effect, during scattering processes with highly energetic particles (Haardt & Maraschi 1993). The particles' combined emission generates the so called "soft X-ray excess". Given the high velocity variation observed for this emission, in the order of the day, the emitting region has to be very small. Broad Fe emission lines are observed in the spectra at these wavelengths and another small "hump" of emission is observed in the hard X-ray region, between 20 and 30 KeV (Beckmann & Shrader 2012).

In the γ**-ray** spectral region, the emission is a peculiarity of a certain class of AGNs called "BLAZARs". At $\sim$MeV energetic scales, the inverse Compton effect dominates the photon-matter interaction, while above 100 MeV, the pair production interactions become predominant. The high energy jets observed in the BLAZARs are the responsible for such emission. In this case, electrons are more energetic than those in the accretion disk. The relativistic motion of these particles in the direction of the observer can further amplify the observed energy.

High variability

The optical luminosity of an AGN is highly variable (10% in a year following Krolik 1999), with an increasing variability at shorter wavelengths. Using variability time-scales, it is possible to quantify the maximum size of the inner emitting regions, which result smaller than a parsec. In the IR continuum, the variability is due to the dust surrounding the inner accretion disk. Since the dust cannot stay closer than a certain distance, called "sublimation radius", due to the high temperatures of the inner regions, the time difference between the optical/UV and the IR luminosity variations allow to measure the inner radius of the dusty torus. Following for example the results of Clavel et al. (1989) this distance resulted $R_i \sim$400 light days.

1.4.2 AGN taxonomy and the unified model

The classification here reported is the result of mainly observational characteristics that each class of AGN shows. Before the advent of the unified model of Urry & Padovani (1995), all these differences were interpreted as intrinsic physical differences of the various objects. Nowadays it is possible to re-interpret the classification and explain the main differences as a consequence of the inclination between the AGN structure and the observer. In this section we present the taxonomy of AGNs. This classification does not have to be intended in a restrictive way since there is not a clean distinction among the different

classes of objects here described.

Radio galaxies

AGN identified as radio sources are usually associated with giant elliptical galaxies. The radio emission is concentrated in a compact nuclear region but radio emitting jets and extended "lobes" are also present. These components extend to the outer galactic regions, from tens of Kpc, to 1Mpc from the central source. There exist more than a classification method, each of which is based on a different observed parameter.

On the basis of their 1.4 GHz luminosity, they can be classified as "*Weak*" ($L_{1.4} < 10^{25}$ W/Hz) or "*Powerful*" ($L_{1.4} > 10^{25}$ W/Hz) radio sources. The weak sources are associated to optically luminous elliptical galaxies and with strong emission lines. The powerful sources show lower optical luminosities and fainter or absent emission lines.

Using the α spectral index at 1 GHz (see Equation (1.15)), radio galaxies can be classified as "*steep*" ($\alpha > 0.4$) or "*flat*" ($\alpha < 0.4$) spectrum sources. The steep spectrum sources show larger extension and appear optically thin, while the "flat" look more compact, variable and optically thick.

Considering the ratio q between the the lobes separation and the total source's size, measured at 178 MHz, radio galaxies can be classified as "*Faranoff-Riley I*" (FRI) when $q < 0.5$ and "*Faranoff-Riley II*" (FRII) when $q > 0.5$. While FRI shows edge darkening effects and redio lobes with a smoothed surface brightness, FRII are edge-bright with lobes characterized by high surface brightness extremes.

Quasars

The quasi stellar radio sources, as they where indicated in the first observations, show a very high luminosity and compact emission. Their extragalactic nature was clarified only after the identification of highly redshifted emission lines. Quasars are classified using the loudness parameter $R = F_r/F_o$ (Kellermann et al. 1994), that represents the ratio between the luminosities measured at 5 GHz and in the B band (4400 Å). The "radio-loud quasars" ($R > 10$) show a strong unresolved radio emission and an optically luminous nucleus ($M_V > -23$). The radio emission is associated with relativistic jets. The "radio-quiet quasars" ($R < 10$) represent the 90% of the entire population. Their radio emission is weaker and with an unclear physical nature, although the most likely explanation is the synchrotron emission from accelerated electrons in shocks (Ishibashi & Courvoisier 2011).

Seyfert galaxies

Seyfert galaxies show quasar-like nuclei, with very high nuclear luminosities but with a detectable host galaxy. Their optical spectrum shows strong emission lines due to both hydrogen recombination and other prohibited transitions, such as oxygen, iron, nitrogen and sulphur.

Seyfert galaxies can be classified on the basis of their optical spectra: type 1 Seyfert galaxies show broad permitted and narrow forbidden lines, while type 2 are characterized by the presence of narrow emission lines only. Most of the spiral galaxies belong to the first typology.

The permitted broad emission lines show widths with values up to 10^4 Km/s. Instead, narrow lines widths are in the order of several hundreds of Km/s and are emitted in low density ionized regions ($n_e \sim 10^3 \div 10^6\,\mathrm{cm}^{-3}$), where both permitted and forbidden emissions are observed. Basing its classification on the optical spectral appearance Os-

terbrock (1981) introduced new Seyfert typologies as: 1.5, 1.8, 1.9, where higher numbers correspond to stronger narrow lines.

Blazars

This class of AGN is characterized by fast optical, X-ray and radio variability and high polarization levels in the continuum and is usually associated with elliptical galaxies and the typical variability time-scale is on the order of the day. In the optical, the polarization degree ranges between 5% and 40%.

Two sub-classes are recognized: the "*BL Lacertae*" type, with strong radio emission, as radio loud quasars, but without strong emission and absorption lines in their spectra, and the "*optically violent variables*", that show some broad emission lines (weaker than those of quasars).

LINERS

Low ionization nuclear emission-line regions (LINERs) represent a low nuclear luminosity class of AGNs. These sources are the most commonly observed class of AGNs. Emission lines due to the Balmer series and to low ionization levels of oxygen and sulphur are observed in the spectra. These last characteristics make this class different from Seyfert galaxies, which show instead higher ionization levels.

Unified model and AGN components

Comparing the IR continuum of Seyfert-1 and Seyfert-2 classes, Rowan-Robinson (1977) found an excess of emission of the Sy2 galaxies with respect to the Sy1. Considering also the differences in the emission line widths, these effects were interpreted as due to the presence of a dusty structure surrounding the central engine of the Sy2 class. In the same work, the possibility of an inclination effect was also argued. Analysing the Sy2 prototype NGC 1068, Antonucci & Miller (1985) observed polarized broad lines in its spectrum. This was possible since, thanks to the reflection by dust, broad lines can be *indirectly* observed. Broad lines cannot be *directly* observed since a dusty structure is interposed between the central engine and the observer. Reflection instead, polarizes the light allowing to observe the effect (Antonucci 1984; Antonucci & Miller 1985; Antonucci 1993). The dusty structure surrounding the central black hole has a toroidal shape. This would explain the observed differences between type 1 and type 2 AGNs (or Seyfert galaxies), through an inclination effect: the broad lines, emitted in the very inner regions close to the accretion disk, are absorbed in a range of inclination values when the circular structure is seen edge-on, and are directly observable when the dusty torus is observed face-on. Narrow lines are emitted above the accretion disk but at higher distances. In this case, the probability to observe this kind of emission lines is higher. See Figure 1.2 for a representation of the unified model.

On the basis of the UV spectra, following the explained unified scheme, all the AGN typologies can be summarized in two simpler classes:

Type 1 AGN : characterized by luminous continuum with both narrow and broad lines. The AGN structure is observed "face-on".

Type 2 AGN : characterized by faint continuum with narrow lines only. The AGN structure is observed "edge-on".

In the unified model picture, almost all the AGNs present similar physical characteristics and components. All of them contain a SMBH at their very center. Its mass can vary

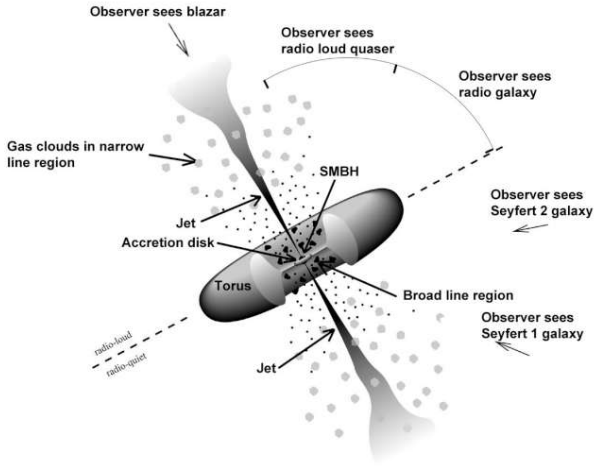

Figure 1.2: Schematic diagram of the AGN paradigm. AGN observative taxonomy does not correspond to physical differences but is the consequence of the inclination between the dusty torus structure surrounding the accretion disk and the observer.

in the range $10^6 \div 10^9$ $M_\odot$ and can be measured using for example the rotational curves of circumnuclear medium. This can be achieved thanks to high resolution HST images (Marconi et al. 2006), or ground based adaptive adaptive optic systems (Häring-Neumayer et al. 2006).

Surrounding the close vicinity of the black hole, an **accretion disk** is responsible of the AGN primary emission. The matter lying in the disk loses angular momentum through viscous and turbulent processes emitting UV radiation. The accretion disk is geometrically thin and optically thick (Shakura & Sunyaev 1973).

Close to the accretion disk, the **hot corona** of highly energetic particles emits in the X-rays through inverse Compton effect of the UV photons emitted by the primary source Haardt & Maraschi (1993).

Broad line regions (BLR) are clouds of gas (N$\sim 10^7 \div 10^8$, Arav et al. 1998) in rapid rotation at a distance of about 0.1 to 1 pc from the center and with a density $n_e \sim 10^9 \div 10^{10}$ cm^{-3}.

At higher distances (~ 100 pc) from the center, the **narrow line regions** (NLR) are characterized by the presence of ionized gas with lower densities than those of the BLRs ($n_e \sim 10^4 \div 10^{55}$ cm^{-3}). This allows for the production of forbidden lines. Compared with the BLR, the lower velocity of the NLR (< 1000 Km/s, Antonucci 1993) determines the narrower width of the lines. The spatial distribution seems to form axisimmetric cones that depart from the inner region towards opposite directions.

The **toroidal dusty torus** that occupies the outer regions of the AGN is responsible for the absorption of the primary emission and for the hiding of the radiation emitted from narrow line regions but it is also responsible for the thermal emission in the FIR spectral region. The presence of this structure was proven for the first time by Antonucci & Miller (1985) through the observation of polarized broad lines in a Seyfert-2 galaxy. The origin of the polarization is due to the reflection of the dust which prevents the direct observation of such lines.

Relativistic Jets are observed in radio loud AGNs. The reason for which jets are present in some AGNs and absent in others is probably related to the collimation of these

structures with the angular momentum of the accretion disk, together with its prominence. Some radio-galaxies show only one outflowing jet. These structures depart from the central black hole and extend to $\sim 10^5 \div 10^6$ pc where they possibly form extended **radio lobes**.

1.5 AGN X-ray Observations

1.5.1 X-ray spectrum

In the immediate vicinity of the SMBH there originates the intrinsic X-ray emission of the AGN. The X-ray continuum arises via inverse Compton scattering in an accretion-disk "corona" over a broad X-ray band, and also perhaps via accretion disk emission at low X-ray energies (e.g. Mushotzky et al. 1993; Reynolds & Nowak 2003; Fabian 2006; Turner & Miller 2009; Done 2010; Gilfanov & Merloni 2014). AGNs hosting powerful jets furthermore often show strong jet-linked X-ray continuum emission (e.g. Worrall 2009; Miller et al. 2011). This intrinsic X-ray emission may then interact with matter throughout the nuclear region to produce, via Compton "reflection" and scattering, more distributed X-ray emission. In some cases, when the intrinsic X-rays are obscured, such reflected/scattered emission may dominate the observed luminosity.

The X-ray properties of bright, optically selected quasars have been intensively studied in the last 25 years (Elvis et al. 1978; Zamorani et al. 1981), mostly with broadband but low resolution spectra. The X-ray emission from quasars extends from the Galactic absorption cut-off at ~ 0.1 keV up to ~ 300 keV. Laor et al. (1997) analyzed the ROSAT soft X-ray (0.5–2 keV) observations of the sample of local ($z < 0.4$) PG quasars, and a subsample of these objects has been studied with ASCA in the 2–10 keV band (George et al. 2000) and with BeppoSAX in the 1–100 keV band (Mineo et al. 2000). Recent studies of samples of bright Seyfert 1 galaxies are reported in (George et al. 1998, ASCA observations) and in (Perola et al. 2002, BeppoSAX observations). The main properties of the X-ray spectra of type I AGN are briefly summarized below and are shown in Fig. 1.3.

1.5.2 X-ray surveys

General utility of X-ray surveys for studies of active galactic nuclei

Cosmic X-ray surveys have now achieved sufficient sensitivity and sky coverage to allow the study of many distant source populations including active galactic nuclei (AGNs), starburst galaxies, normal galaxies, galaxy clusters, and galaxy groups. Among these, AGNs, representing actively growing supermassive black holes (SMBHs), dominate the source number counts as well as the received integrated X-ray power. This has led to an impressive literature on the demographics, physics, and ecology of distant growing SMBHs found in X-ray surveys (Brandt & Alexander 2015).

Cosmic X-ray surveys of AGNs offer considerable utility for several reasons:

1. X-ray emission appears to be nearly universal from the luminous AGNs that dominate SMBH growth in the Universe. When AGNs have been reliably identified using optical, infrared, and/or radio techniques, they almost always also show X-ray AGN signatures (e.g., Avni & Tananbaum 1986; Brandt et al. 2000; Mushotzky 2004; Gibson et al. 2008). Thus, the intrinsic X-ray emission from the accretion disk and its corona empirically appears robust, even if its detailed nature is only now becoming clear (e.g., Done 2010; Schnittman & Krolik 2013).

2. X-ray emission is penetrating with reduced absorption bias. The high-energy X-ray

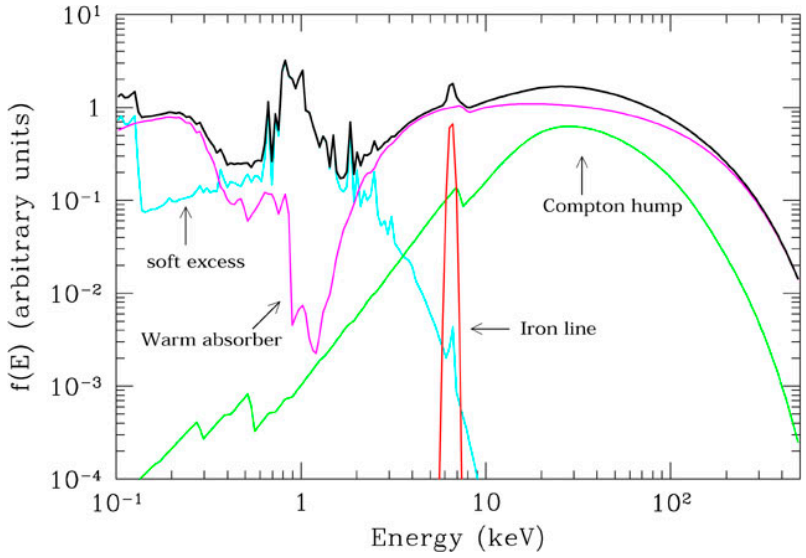

Figure 1.3: Average total spectrum (thick black line) and main components (thin grey lines) in the X-ray spectrum of a type I AGN. The main primary continuum component is a power law with an high energy cut-off at E $\sim 100-300$ keV, absorbed at soft energies by warm gas with $N_H \sim 10^{21} - 10^{23}\,cm^{-2}$. A cold reflection component is also shown. The most relevant narrow feature is the iron K_α emission line at 6.4 keV. Finally, a "soft excess" is shown, due to thermal emission of a Compton thin plasma with temperature kT $\sim 0.1 - 1$ keV.

emission observed from AGNs is capable of directly penetrating through substantial columns with hydrogen column densities of $N_H = 10^{21}$–$10^{24.5}$ cm^{-2} (e.g., Wilms et al. 2000, and references therein)[1]. This is critically important, since the majority of AGNs in the Universe are now known to be absorbed by such column densities. X-ray surveys thus aid greatly in identifying the majority AGN populations and, moreover, in allowing their underlying luminosities to be assessed reliably (in a regime where optical/UV luminosity indicators are generally unreliable). Only in the highly Compton-thick regime ($N_H \gg 1/\sigma_T$, corresponding to $N_H \gg 1.5 \times 10^{24}$ cm^{-2}) does direct transmission become impossible, but here one can still investigate the (much fainter) X-rays that are reflected or scattered around the absorber (e.g., Comastri 2004; Georgantopoulos 2013). An additional relevant advantage of X-ray studies is that, as one studies objects at increasing redshift in a fixed observed-frame band, one gains access to increasingly penetrating rest-frame emission (i.e., higher rest-frame energies are probed); note the opposite generally applies in the optical and UV bandpasses where dust-reddening effects increase toward shorter wavelengths (e.g., Cardelli et al. 1989).

3. X-rays have low dilution by host-galaxy starlight (i.e., emission at any wavelength associated with stellar processes). AGNs generally have much higher ratios of L_X/L_{Opt} and thus f_X/f_{Opt} than stars (e.g., Maccacaro et al. 1988). Thus, X-rays provide excellent contrast between SMBH accretion light and starlight, allowing one to construct pure samples of AGNs even down to relatively modest luminosities. This

[1]For purposes of basic comparison, the column density through your hand is $N_H \sim 10^{23}$ cm^{-2}, while that through your chest is $N_H \sim 10^{24}$ cm^{-2} (with significant variation depending upon the amount of bone

aspect of X-ray surveys is critical, for example, at high redshift where it is often unfeasible, at any wavelength, to resolve spatially the AGN light from host starlight. For weak or highly obscured AGNs, such dilution by host starlight can make AGNs difficult to separate from galaxies in the optical/UV regime (e.g., Moran et al. 2002; Hopkins et al. 2009).

4. The X-ray spectra of AGNs are rich with diagnostic potential that can be exploited when sufficient source counts are collected. At a basic level, the distinctive X-ray spectral characteristics of AGNs can often aid with their identification, improving still further the purity of AGN samples (see the previous point). Furthermore, measurements of low-energy photoelectric absorption cut-offs, underlying continuum shapes, Compton reflection continua, fluorescent line emission (e.g., from the iron Kα transition), and absorption edges (e.g., the iron K edge) can diagnose system luminosity, obscuration level, nuclear geometry, disk/corona conditions, and Eddington ratio ($L_{\rm Bol}/L_{\rm Edd}$).

While these basic points of utility have led to great success for the enterprise of X-ray surveys, such surveys do have their shortcomings; e.g., in the regime of highly Compton-thick absorption or in cases of intrinsically X-ray weak AGNs. Thus, when possible, it is critical to complement X-ray surveys with suitably matched multi=wavelength surveys in the area of sky under study. These can help considerably in filling the small chinks in the armor of X-ray surveys, thereby allowing nearly complete identification of all significant SMBH growth.

The survey capabilities of relevant distant-universe missions: *Chandra*, *XMM-Newton*

Over the past 15 yr there has been an intensive activity in X-ray (0.5–100 keV) surveys research, mainly focusing on missions that can make sensitive "blank-field" surveys of typical AGNs in the distant ($z = 0.1$–5) universe. The main observatories working in this kind of survey are the *Chandra X-ray Observatory* (hereafter *Chandra*; (e.g., Weisskopf et al. 2000)), the *X-ray Multi-Mirror Mission* (hereafter *XMM-Newton*; e.g., Jansen et al. 2001), and the *Nuclear Spectroscopic Telescope Array* (hereafter *NuSTAR*; e.g., Harrison et al. 2013). The new results from these missions rest squarely upon a rich heritage of X-ray survey studies with several superb earlier X-ray missions.

In terms of basic survey capability, both *Chandra* (launched in 1999 July) and *XMM-Newton* (launched in 1999 December) provide X-ray *spectroscopic imaging* over broad bandpasses (0.3–8 keV and 0.2–10 keV, respectively) and over respectable fields of view (290 arcmin^2 for *Chandra* ACIS-I, and 720 arcmin^2 for *XMM-Newton* EPIC-pn).[2] Their imaging point spread functions are excellent (an on-axis half-power diameter of 0.84 " for *Chandra*) or good (15 " for *XMM-Newton*), though these degrade significantly with increasing off-axis angle. Their most sensitive surveys reach about 80–400 times deeper than those of previous X-ray missions, and excellent source positions (accurate to 0.5–4 ") allow effective multiwavelength follow-up studies even at the faintest X-ray fluxes. Typical survey projects with *Chandra* and *XMM-Newton* generate hundreds-to-thousands of detected

intercepted).

[2]Note that many X-ray detectors, including those used on *Chandra* and *XMM-Newton* to perform cosmic surveys, *simultaneously* obtain imaging, spectral, and timing data for the collected photons (e.g., Strüder et al. 2001; Turner et al. 2001; Garmire et al. 2003). Such X-ray observations are qualitatively different from those generally taken in the optical/infrared where, e.g., imaging and spectroscopy are largely distinct.

AGNs, allowing powerful statistical studies of source populations. Furthermore, systematic public data archiving practices allow effective survey combination, so that source populations spanning wide ranges of luminosity and redshift can be studied together.

1.6 Interplay between AGN and SF activity

AGN and star formation activity coexist in galaxies at all redshifts (Farrah et al. 2003; Alexander et al. 2005). While the small dimension of an AGNs seems to prevent from possible strong interactions between the few inner parsecs and the rest of the host galaxy, various observations suggest a different scenario. In this section we briefly explore the various clues on the co-evolution of the two mechanisms which motivate our work, and the possible physical connection that relates them.

One of the most important relations between AGNs and host galaxies is the observed correlation between the mass of the SMBH and the mass of the galaxy bulge (e.g. Marconi & Hunt 2003).

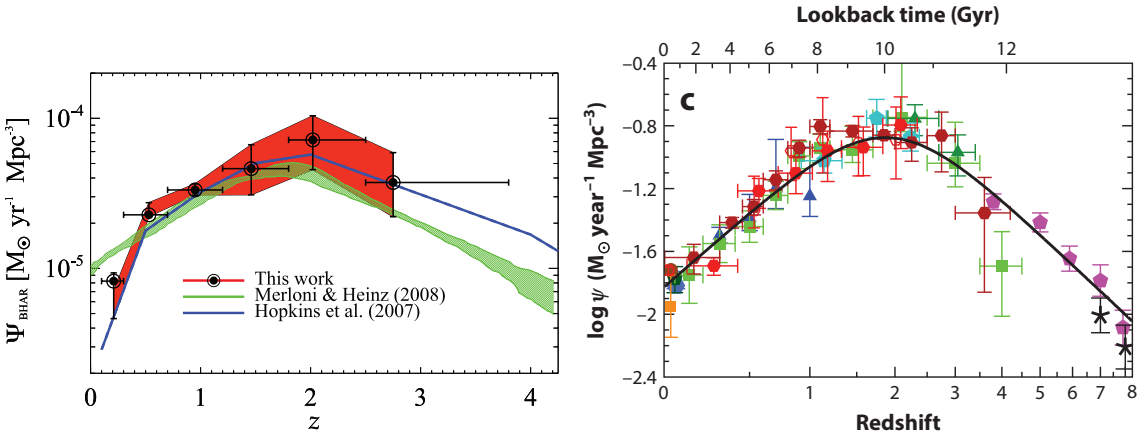

Figure 1.4: Evolution of the BHAR density (Madau & Dickinson 2014, left panel) and of the SFR density (Delvecchio et al. 2014, right panel). (*Left panel*) Black Hole Accretion Rate Density estimate from the *Herschel* selected AGN luminosity function, as a function of redshift (black circles). The red shaded area shows the 1σ uncertainty region. Previous estimates from different selection wavelengths (from Merloni & Heinz (2008), and Hopkins et al. (2007)) are reported for comparison. (*Right panel*) Cosmic star formation from FUV+IR rest-frame measurements. All UV luminosities have been converted to instantaneous SFR densities using the factor $K_{FUV} = 1.15 \times 10^{-28}$, valid for a Chabrier (2003) IMF. FIR luminosities (8–1000 µm) have been converted to instantaneous SFRs using the factor $K_{IR} = 4.5 \times 10^{-44}$, also valid for a Salpeter (1955) IMF.

As suggested for the first time by Franceschini et al. (1999), the evolution of the global star formation rate density (i.e. the SFR per unit of comoving space) looks similar to that characterizing the black hole accretion rate density (BHARD). In particular, as can be seen in Fig. 1.4, both the SFRD and the BHARD show a peak of activity at $z \sim 2$ (Lilly et al. 1996; Madau et al. 1996; Hopkins & Beacom 2006; Hopkins et al. 2007; Merloni & Heinz 2008; Delvecchio et al. 2014).

The observed main sequence of star-forming galaxies (see Section 1.2) has a counterpart when considering the BHAR (Mullaney et al. 2012b): both the star formation rate and the central black hole accretion rate are correlated to the mass in stars M_* of the host galaxy.

Figure 1.5: Comparison between the SFR and BHAR from Rodighiero et al. (2015) at $1.5 < z < 2.5$. The cyan squares are from Mullaney et al. (2012b). These results are going to be the starting point of our work.

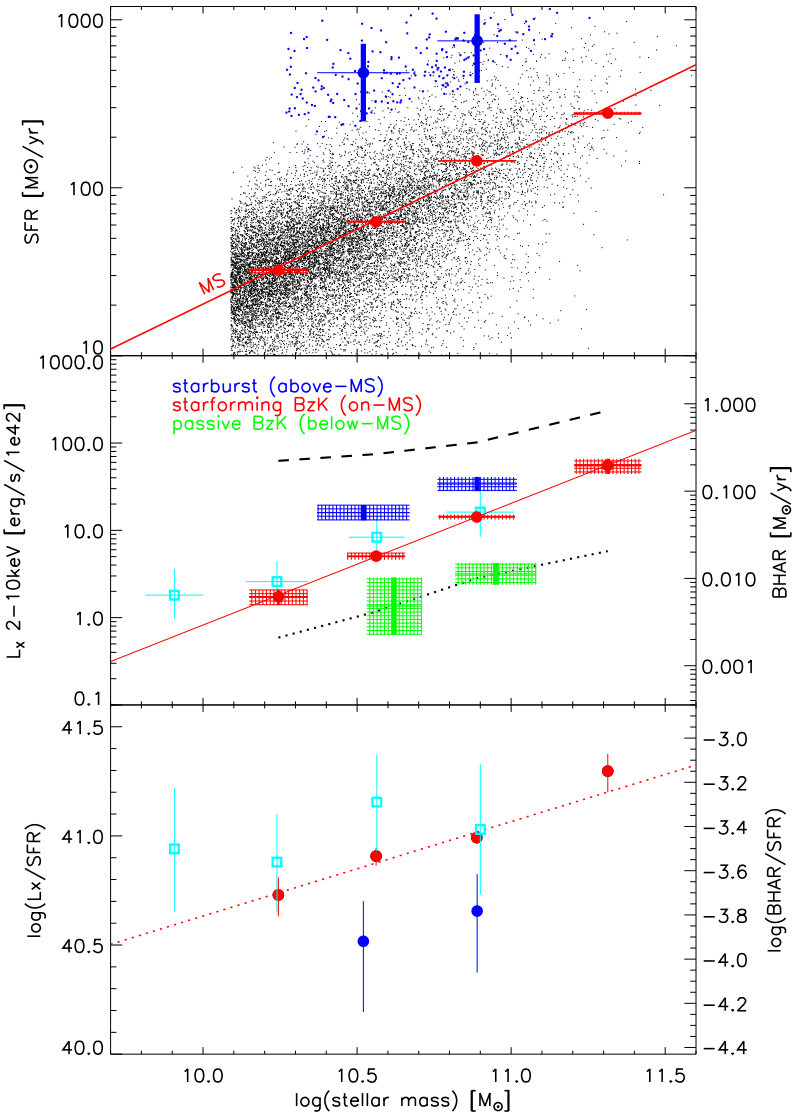

An even more direct relation between the star formation and the black hole accretion is observed for example in (Rodighiero et al. 2015, whose Fig. 1 we report in Fig. 1.5), where the BHAR increases with the sSFR. These two works are going to be the starting point of this thesis, in particular we are going to start with the sample of galaxies of Rodighiero et al. (2015) and take advantage of the new Chandra data, *COSMOS-Legacy*. Then we will expand our work to a new sample, the COSMOS2015 catalogue.

Physically, one important issue concerning the interaction between AGN and star formation is the concept of "AGN feedback". The AGN role in the star formation activity can be both positive and negative depending on the evolutionary stage. While at early times the presence of an AGN may trigger the star formation, at later stages it is one of the responsible factors of its quenching. This is indeed observed in deep surveys (e.g. Page et al. 2012). A luminous AGN causes the heating and the photo-ionization of the surrounding medium, and the radiation pressure can push the gas to outer galactic regions with a resulting lack of fuel for further star formation (Springel et al. 2005; Farrah et al.

2012; Cano-Díaz et al. 2012; Pope et al. 2012). A negative feedback is also required by semi-analytical models and cosmological simulations, in order to suppress the star formation activity (Granato et al. 2004; Springel et al. 2005; Bower et al. 2006; Croton et al. 2006; Booth & Schaye 2009). On the other hand, a positive feedback would explain the circumnuclear starbursts observed in local AGNs (Genzel et al. 1998; Schweitzer et al. 2006).

One of the most popular explanations of the AGN-starburst connection is given by Hopkins et al. (2008). In this scenario, the connection between the two mechanisms is found in major mergers between galaxies. These drive new fuel to the inner regions, enhancing both the star formation and the black hole accretion. After a rapid growth, the central black hole begins to dominate the total luminosity. Gas and dust are heated, ionized and then removed by radiation pressure, quenching the star formation.

Given the relations observed and discussed between AGNs and host galaxies, it becomes crucial to quantify the relative importance of the two mechanisms. This can be obtained, for example, through the ratio between the emission of AGN and the rest of the galaxy, at different wavelengths. In this thesis we are going to estimate the AGN emission from the X-ray flux in the 2–10 keV band and the SFR from FIR 160 µm band. This will allow us to to expand our knowledge of how these two mechanisms are related.

Throughout this thesis we are going to use Chabrier (2003) IMF and a flat cosmology with $H_0 = 71$, $\omega_\lambda = 0.73$, $\omega_0 = 0.27$.

Chapter 2

Data and sample selection

In this chapter we introduce the COSMOS survey, which is the field where the observations used in this thesis were carried out, the principal instruments used for the observations, the individual survey programs and the sample selection. We reserve a special treatment for the X-ray data, about which we are going to talk in chapter 3, since it is the most important part of this thesis.

2.1 The COSMOS survey

COSMOS (Scoville et al. 2007) is an astronomical survey designed to probe the formation and evolution of galaxies as a function of cosmic time (redshift) and large scale structural environment.

COSMOS is a pan-chromatic—radio to X-ray—survey of a patch of the sky both large enough (2 $\deg^2$) and deep enough (AB$\sim$ 26 at the optical wavelength) to study galaxy and quasar evolution up to high redshifts in typical environments, with minimal "cosmic bias". Almost all major telescopes have observed this field deeply. From space—Hubble, Spitzer, Herschel, GALEX, XMM-Newton—and ground-based—VLA, Subaru, CTIO, KPNO, CFHT, Magellan, VLT. The central region ($\sim$ 1 $\deg^2$) has been targeted with even deeper surveys by Chandra, VLT, HST (CANDELS), VISTA. The location of COSMOS near the equator (central coordinates: 10^h, $+02^\circ$) allows access by all future facilities (esp. JVLA, ALMA). The COSMOS survey involves almost 100 scientists in a dozen countries.

The aim of COSMOS is to thoroughly map the morphology of galaxies as a function of local environment (density) and epoch, all the way from high redshift ($z > 3$) to the nearby ($z < 0.5$) Universe. Substantial Large Scale Structure (LSS) exists on scales up to 100 Mpc (co-moving), influencing galaxy evolution and morphological mix. Therefore, the field size is adopted to encompass comoving areas of 50×50 Mpc at $z = 0.5$, 137×137 Mpc at $z = 2$ and 170×170 Mpc at $z = 3$, fully sampling all scales currently envisaged for LSS. The comoving volume to $z = 4$, covered by the COSMOS, is $9 \cdot 10^7$ Mpc^3, comparable to those sampled in the local Universe by the SLOAN and 2dF surveys. Imaging in F814W (broad filter in the NIR mounted on Wide Field Camera (WFC) instrument on HST) will provide sufficiently deep data to fully characterize morphology, multiplicity and interaction of L* galaxies to z$\sim$ 2 (I$\sim$ 26mag), measure structural parameters of galaxies and perform bulge/disk decomposition.

Combined with the follow-up observations from space and ground-based facilities, COSMOS addresses fundamental issues in observational cosmology, including:

- the evolution of LSS, galaxies, clusters and CDM on scales up to $> 10^{14}\,\mathrm{M}_\odot$, well

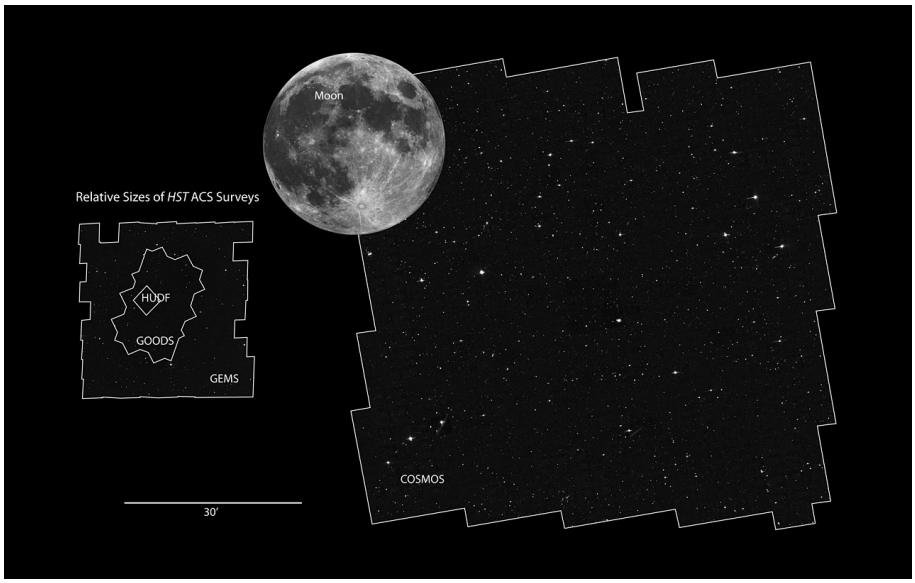

Figure 2.1: Illustration of the COSMOS field (right) relative to the full moon and the GEMS, GOODS, and HUDF fields. Image credit: NASA, ESA, and Z. Levay.

sampled as a function of redshift;

- the formation, assembly and evolution of galaxies and star formation as a function of LSS environment, morphology and redshift;
- the dark matter distributions and properties out to $z \sim 1$ using gravitational lensing shear maps;
- evolution of AGNs and the relationship between black hole growth and galaxy evolution, which is also the aim of this thesis.

2.2 Key observations for the selection

In this section we introduce *Herschel* Space Observatory, whose observations will be fundamental for the SFR computation and the catalogue COSMOS2015, based on NIR observations, which will be the starting point for the new sample.

2.2.1 *Herschel* Space Observatory

Herschel (formerly known as FIRST) was an ESA space observatory with science instruments provided by European-led Principal Investigator consortia and with important participation from NASA. It was launched on 14 May 2009, reaching the second Lagrangian point (L2) of the Earth–Sun system, and was an operational ESA space observatory offering unprecedented observational capabilities in the far-infrared and submillimetre spectral range 55−671 µm. *Herschel* was active from 2009 to 2013, and was the largest infrared telescope ever launched (see Fig. 2.2), carrying a 3.5 metre diameter passively cooled Cassegrain telescope, which is the largest of its kind and utilised a novel silicon carbide technology. The science payload comprised three instruments: two direct detection cameras/medium resolution spectrometers, PACS and SPIRE, and a very high-resolution heterodyne spectrometer, HIFI, whose focal plane units were housed inside a superfluid helium cryostat. The mission lifetime was determined by the cryostat hold time. Nom-

inally approximately 20,000 hours were available for astronomy (to around the end of 2012), but it continued to operate until 29 April 2013. 32% was guaranteed time and the remainder was open to the worldwide general astronomical community through a standard competitive proposal procedure (Pilbratt et al. 2010).

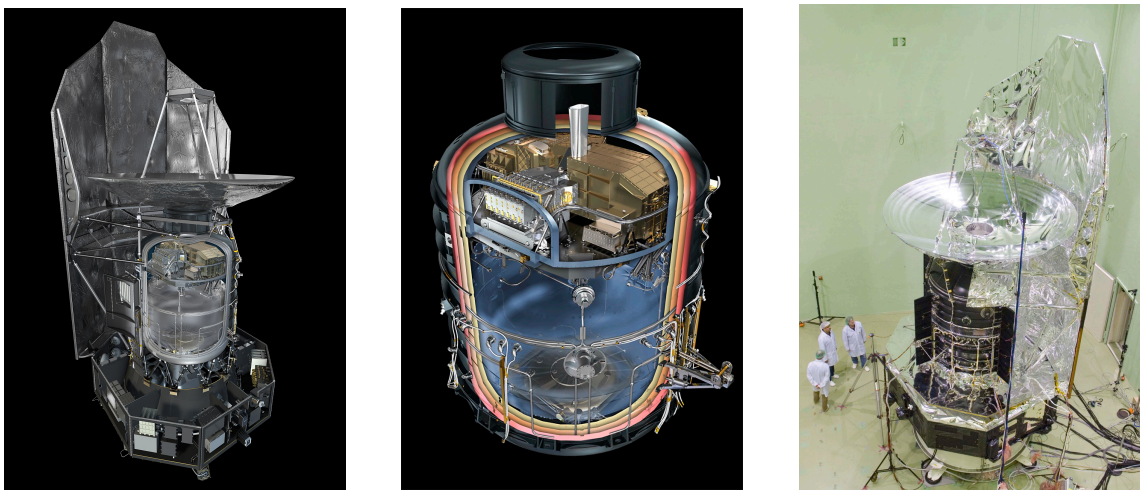

Figure 2.2: Left: The *Herschel* spacecraft features the 'payload module' (PLM) with the cryostat housing the instrument focal plane units (FPUs), the telescope, the 'service module' (SVM) with 'warm' electronics, and the sunshield/sunshade. Middle: Close-up of the PLM displaying the optical bench with the instrument FPUs on top of the main helium tank. The focal plane cover and the three vapour-cooled shields inside the cryostat vacuum vessel (CVV) are also shown. Right: *Herschel* being prepared for acoustic testing in the Large European Acoustic Facility (LEAF) in the ESTEC Test Centre in June 2008, providing a good view of the telescope (ESA).

Spacecraft description

The *Herschel* spacecraft (see Fig. 2.2) provides the appropriate working environment for the science instruments, points the telescope with required accuracy, autonomously executes the observing timeline, and performs onboard data handling and communication with the ground. It has a modular design, consisting of the "payload module" (PLM) supporting the telescope, the sunshade/sunshield, and the "service module" (SVM).

Telescope

The *Herschel* telescope (Doyle et al. 2009) was constructed to be as large as possible and still be compatible with no inflight deployable structures and as cold as possible with passive cooling. At the same time it needed to have a low mass and the required mechanical and thermal properties.

The optical design is that of a classical Cassegrain telescope with a 3.5 m physical diameter primary and an "undersized" secondary, yielding an effective primary diameter of 3.28 m. The telescope is constructed almost entirely (∼90% by mass) of silicon carbide (SiC). The primary mirror has been made out of 12 segments, "brazed" together to form a monolithic mirror blank, which was machined and polished. The secondary is a single piece, machined with an integral "scattercone" to suppress standing waves and the narcissus effect. The M1 and M2 optical surfaces have been coated with a high reflectivity/low

emissivity aluminium layer, covered by a thin protective "plasil" (silicon oxide) coating which allows cleaning.

The telescope internal alignment and WFE performance were measured in cold conditions. Similar to ISO, a fully passive design was adopted, with no means of inflight adjustments such as e.g. focusing.

Science instruments

The science payload consists of three instruments, provided by consortia of institutes led by their Principal Investigators (PIs):

- The Photodetector Array Camera and Spectrometer (PACS), PI: A. Poglitsch, Max-Planck-Institut für extraterrestrische Physik (MPE), Garching.
- The Spectral and Photometric Imaging REceiver (SPIRE), PI: M. J. Griffin, Cardiff University.
- The Heterodyne Instrument for the Far Infrared (HIFI), PI: T. de Graauw, in late 2008 succeeded by F. Helmich, SRON Netherlands Institute for Space Research, Groningen.

Table 2.1: Science instrument main characteristics. Acronyms relating to the detectors: superconductor-insulator-superconductor (SIS), hot electron bolometer (HEB), gallium-doped germanium (Ge:Ga), and neutron transmutation doped (NTD).

HIFI	heterodyne spectrometer
Wavelength coverage	157−212 & 240−625 µm
Field-of-view (FOV)	single pixel on sky
Detectors	5×2 SIS & 2×2 HEB mixers
Spectrometers	auto-correlator & acousto-optical
Spectral resolving power	typically 10^6
PACS	2-band imaging photometer
Wavelength coverage	60−85 or 85−130, 130−210 µm
Field-of-view (FOV)	$0.5F\lambda$ sampled $1.75' \times 3.5'$
Detectors	64×32 & 32×16 pixel bol. arrays
PACS	integral field spectrometer
Wavelength coverage	55-210 µm
Field-of-view (FOV)	$(5 \times 5$ pixel$) \sim 47' \times 47'$
Detectors	two 25×16 pixel Ge:Ga arrays
Spectral resolving power	1000−4000
SPIRE	3-band imaging photometer
Wavelength bands ($\lambda/\Delta\lambda \sim 3$)	250, 350, 500 µm
Field-of-view (FOV)	$2F\lambda$ sampled $4' \times 8'$
Detectors	139, 88 & 43 pixel NTD bol. arrays
SPIRE	imaging fourier transf. spectrometer
Wavelength coverage	194−324 & 316−671 µm
Field-of-view (FOV)	$2F\lambda$ sampled circular $2.6'$
Detectors	37 & 19 pixel NTD bol. arrays
Spectral resolving power	370−1300 (high) / 20−60 (low)

The three instruments complement each other (Table 2.1), enabling *Herschel* to offer its observers broad band photometric imaging capability in six bands with centre wavelengths

of 70, 100, 160, 250, 350, and 500 µm, imaging spectroscopy over the entire *Herschel* wavelength coverage, and very high resolution spectroscopy over much of this range.

A number of observing modes are provided, including point source photometry, small, and large area photometric imaging, and the observation of a single spectral line, or one or more spectral ranges, in either a single position or in various mapping modes.

PACS is a camera and low to medium resolution spectrometer for wavelengths in the range 55-210 µm. It employs four detector arrays, two bolometer arrays and two Ge:Ga photoconductor arrays. The bolometer arrays are dedicated for wideband photometry, while the photoconductor arrays are to be employed exclusively for spectroscopy with a resolution of a few thousand. PACS can be operated either as an imaging photometer, or as an integral field line spectrometer.

SPIRE is a camera and low to medium resolution spectrometer complementing PACS for wavelengths in the range 194-672 µm. It comprises an imaging photometer and a Fourier Transform Spectrometer (FTS), both of which use bolometer detector arrays. There are a total of five arrays, three dedicated for photometry and two for spectroscopy.

HIFI is a very high resolution heterodyne spectrometer covering the 490-1250 GHz and 1410-1910 GHz bands. It utilises low noise detection using superconductor-insulator-superconductor (SIS) and hot electron bolometer (HEB) mixers, together with acousto-optical and autocorrelation spectrometers. HIFI is not an imaging instrument, it observes a single pixel on the sky at a time.

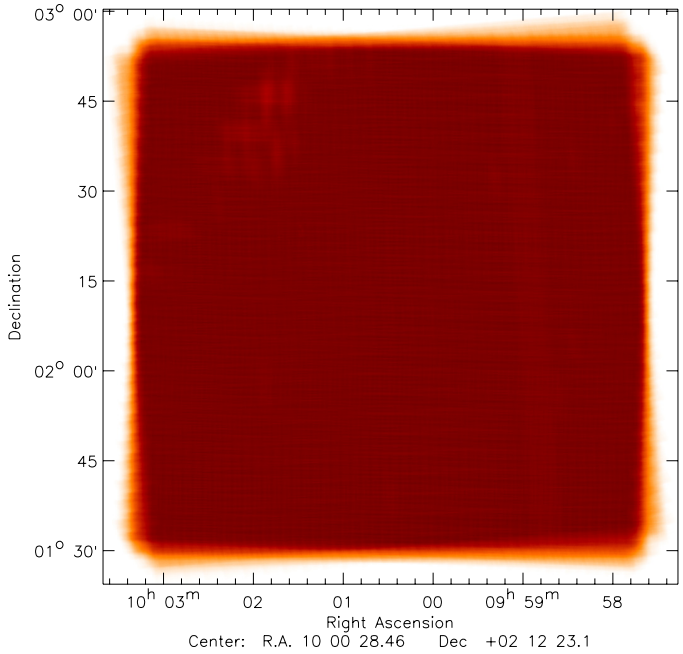

Figure 2.3: Actual *Herschel* 160 µm coverage map of the COSMOS field.

Herschel's COSMOS data

The COSMOS field was observed by Herschel as part of the PACS Evolutionary Probe (PEP) guaranteed time key program (Lutz et al. 2011). It was the largest field of the

program, observed for about 200 h to a 3σ depth at 160 µm of 10.2 mJy (see Fig. 2.3) and at 100 µm ∼5 mJy. At this level, integral number counts reach one source per 24 beams (Berta et al. 2010, 2011), similar to the 5σ 40 beams/source definition of the "confusion limit" used by, e.g., Rowan-Robinson (2001).

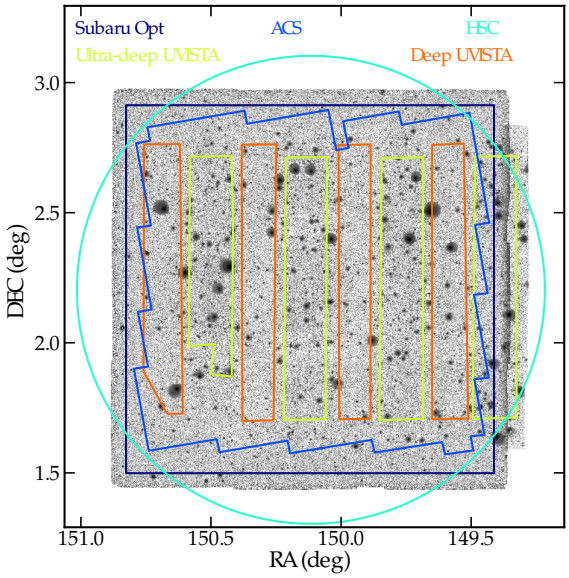

Figure 2.4: Schematic diagram of the COSMOS field, showing all the optical (dark blue and turquoise) and near-infrared (green and orange) observations used. The background image corresponds to the chi-squared YKHK$_s$-z^{++} detection image. For reference, the region covered by COSMOS-Advanced Camera for Surveys (ACS) HST data is shown in cyan.

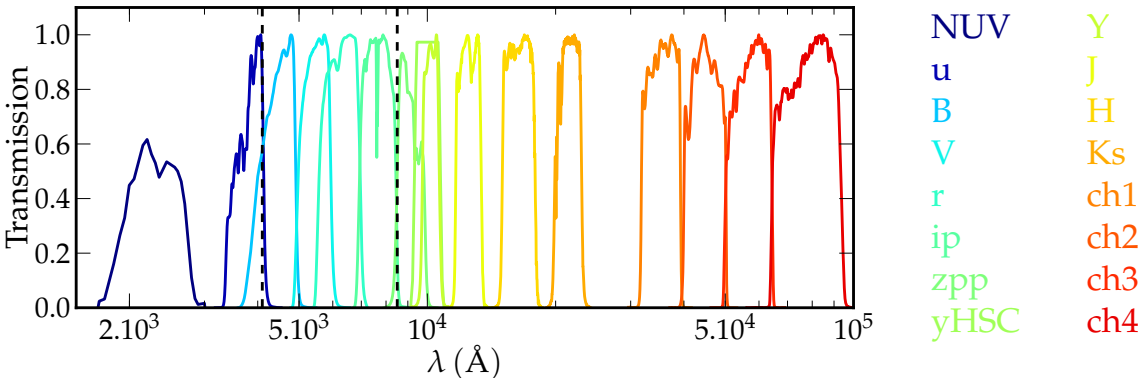

Figure 2.5: Transmission curves corresponding to the photometric bands used in this work. For clarity, intermediate and narrow bands are not represented, but the region of the spectrum covered by these bands is marked by dashed lines.

2.2.2 COSMOS2015 catalog description

The COSMOS2015 catalogue (Laigle et al., in prep.) contains 30-band photometry and precise photometric redshifts for more than one million objects over the 2 deg^2 COSMOS

Figure 2.6: COSMOS2015 available data in each band and the average limiting magnitudes computed from variance betweern 2 and 3″ diameter apertures on the homogenised images (Table from Laigle et al. in prep.).

Instrument /Telescope (Survey)	**Filter**	**Central λ (Å)**	**Width (Å)**	**3σ depth** [a] **(3″/2″)** ±0.1
GALEX	NUV	2306.5	789.1	25.5 [b]
MegaCam/CFHT	u^*	3911.0	538.0	26.6/ 27.2
SuprimeCam	B	4439.6	806.7	27.0/ 27.6
/Subaru	V	5448.9	934.8	26.2/ 26.9
	r	6231.8	1348.8	26.5/ 27.0
	i^+	7629.1	1489.4	26.2/ 26.9
	z^{++}	8800	1200	25.9/ 26.4
	$IA427$	4256.3	206.5	25.9/ 26.5
	$IA464$	4633.3	218.0	25.9 / 26.5
	$IA484$	4845.9	228.5	25.9/ 26.5
	$IA505$	5060.7	230.5	25.7/ 26.2
	$IA527$	5258.9	242.0	26.1/ 26.6
	$IA574$	5762.1	271.5	25.5/ 26.0
	$IA624$	6230.0	300.5	25.9/ 26.4
	$IA679$	6778.8	336.0	25.4/ 26.0
	$IA709$	7070.7	315.5	25.7/ 26.2
	$IA738$	7358.7	323.5	25.6/ 26.1
	$IA767$	7681.2	364.0	25.3/ 25.8
	$IA827$	8240.9	343.5	25.2/ 25.8
	$NB711$	7119.6	72.5	25.1/ 25.7
	$NB816$	8149.0	119.5	25.2/ 25.8
HSC/Subaru	Y	10027.3	1398.5	24.4/ 24.9
VIRCAM	$Y^{\rm UD}$	10200	1000	**25.3**/ 25.8
/VISTA	$Y^{\rm Deep}$			24.8/ 25.3
(UltraVISTA DR2)	$J^{\rm UD}$	12500	1800	**24.9**/ 25.4
	$J^{\rm Deep}$			24.7/ 25.2
	$H^{\rm UD}$	16500	3000	**24.6**/ 25.0
	$H^{\rm Deep}$			24.3/ 24.9
	$K_{\rm s}^{\rm UD}$	21537.2	3120	**24.7**/25.2
	$K_{\rm s}^{\rm Deep}$			24.0/ 24.5
WIRCam	$K_{\rm s}$	21537.2	3120	23.4/ 23.9
/CFHT	H	16500	3000	23.5/ 24.1
IRAC/*Spitzer*	ch1	35262.5	7412.0	25.5/ o [c]
(SPLASH)	ch2	44606.7	10113.0	25.5/ o[c]
	ch3	56764.4	13499.0	23.0/ o[c]
	ch4	77030.1	28397.0	22.9/ o [c]

[a] 3σ depth in $m_{\rm AB}$ computed on PSF-matched images from around 800 apertures at 2 and 3″(apertures containing an object having already been discarded).
[b] Value given in Zamojski et al. (2007) corresponding to a 3σ depth.
[c] 3σ depth in $m_{\rm AB}$ computed from the RMS maps, after masking area containing an objects based on the segmentation map.

field. Including new YJHK$_s$ images from the UltraVISTA-DR2 survey, Y-band fom Hyper Suprime-Cam and infrared data from SPLASH Spitzer legacy program, this near-infrared selected catalog is highly optimised for the study of galaxy evolution and environments in the early Universe.

The main improvement compared to previous COSMOS data is the addition of new, deeper near-infrared and infrared data from the UltraVISTA and the SPLASH (Spitzer Large Area Survey with Hyper-Suprime-Cam) projects. All images and noise maps have been resampled to the same tangent point RA,DEC= (150:116; 2:201). The entire catalogue covers a square of 2 deg^2 centered on this tangent point. Figure 2.4 shows the footprint of all observations. Figure 2.5 shows the transmission curves of all filter (filter, atmosphere and detector) and are available electronically from Caltech[1]. COSMOS near-infrared data comes from several sources: WIRCam (McCracken et al. 2010) covering the entire field and UltraVISTA (McCracken et al. 2012) data covering the central 1:5 deg^2. The UltraVISTA data is DR2 "deep" and "ultra-deep" stripes, the depth and completeness in our final catalogue is not the same over the whole COSMOS field because it is

[1] `http://www.astro.caltech.edu/capak/filters/index.html`

derived in part from these data.

2.3 Samples

For this thesis' work we use two samples. For the first part of the work we use the same starting sample as Rodighiero et al. (2015) in the whole COSMOS field (in their case it was then restricted to the Chandra *C-COSMOS* area) in the redshift interval $1.5 < z < 2.5$. This sample is composed by the BzK selected star-forming and quiescent galaxies and by the HSO selected stabursts. For the second part of the work we use the COSMOS2015 catalog to select with the NUV-r/r-J criterion, star-forming and quiescent galaxies in the redshift interval $0.1 < z < 3.5$.

2.3.1 Sample of Rodighiero et al. (2015)

The BzK criterion

The BzK criterion (Daddi et al. 2004) is a simple two color selection based on B-, z-, and K- band photometry. Its aim is to cull galaxies at $1.4 \lesssim z \lesssim 2.5$ in K-selected samples and to classify them as star-forming or passive systems. The method is calibrated on the highly complete spectroscopic redshift database of the K20 survey (Cimatti et al. 2002a,b,c; Daddi et al. 2002; Pozzetti et al. 2003; Fontana et al. 2004), in combination with stellar evolutionary tracks. As k-corrections in K band are insensitive to galaxy type over a wide redshift range, near-infrared-selected samples provide a fairly unbiased census of galaxy populations at high redshifts. Requiring

$$BzK = (z - K)_{AB} - (B - z)_{AB} > -0.2$$

allows to select actively star-forming galaxies at $z \gtrsim 1.4$ (hereafter $sBzK$), independently on their dust reddening (this is because the reddening vector in the BzK plane is approximately parallel to the $sBzK$ selection criteria). Instead, objects with

$$BzK < -0.2 \quad \text{and} \quad (z - K)_{AB} > 2.5$$

colors include passively evolving galaxies at $z \gtrsim 1.4$ (hereafter $pBzK$), often with spheroidal morphologies. Stars have colors that are clearly separated from the regions occupied by galaxies and can be efficiently isolated with the criterion

$$(z - K) < 0.3 \cdot (B - z) - 0.5.$$

BzK selected galaxies from the COSMOS-WIRCam near infrared imaging survey

We use the K-band selected sample of $1.5 < z < 2.5$ galaxies from the COSMOS-WIRCam near infrared imaging survey (McCracken et al. 2010) in the 2 deg^2 of the COSMOS field. The survey takes advantage of the WIRCam at the Canada–France–Hawaii Telescope (CFHT) in order to provide K_s-band imaging in the COSMOS survey. The sample contains 143,466 galaxies with magnitude $\mathrm{K}_{s,\mathrm{AB}} < 23$ which are selected according to the BzK criterion (see Fig. 2.7).

Starburst sample from the Herschel PEP observations

For the starburst sample we start from the Gruppioni et al. (2013) sample selected from the Herschel PEP observations in the COSMOS field (Lutz et al. 2011). We refer to Berta et al. (2010) for a detailed description of the data catalogues and source counts.

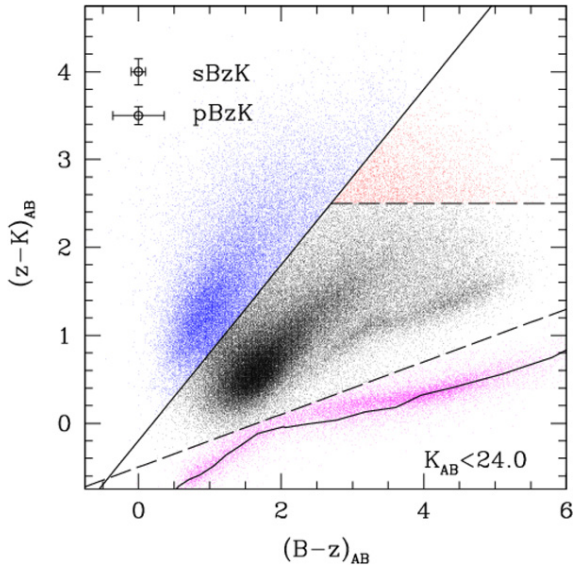

Figure 2.7: $(B-Z)_{AB}$ vs. $(z-K)_{AB}$ diagram for all galaxies in the COSMOS field in the work of McCracken et al. (2010). Four distinct regions are shown: stars (violet, lower part of the diagram), galaxies at $z < 1.4$ (black, middle), star-forming galaxies (blue, left), and passively evolving galaxies (red, top right). The solid line shows the colors of stars in the BzK filter set of Daddi et al. (2004).

Stellar masses have been derived by fitting the broad-band SEDs of our sources using a modified version of MAGPHYS (da Cunha et al. 2008; Berta et al. 2013). Such M_* are consistent with those derived with the formalism of (Daddi et al. 2007, zero offset and a dispersion of ∼0.3dex). The SFRs of these galaxies are derived from the total IR luminosities (estimated via SED fitting, see Gruppioni et al. (2013)).

To classify a sample of starburst galaxies lying above the MS, we have applied the same criterion as (Rodighiero et al. 2011, i.e., sSFR 0.6 dex above the MS) over the whole $1.5 < z < 2.5$ range. This selection provides a total number of 231 candidate starbursts with $\log(M_*) > 10.27$ $M_\odot$.

2.3.2 COSMOS2015 sample selection—NUV-r/r-J criterion

For the COSMOS 2015 catalogue, which is in a wider redshift interval than that where the BzK is effective, we need a different selection technique in order to divide the sample into quiescent and star-forming galaxies. Using more than a single selection criterion would bring about some bias between the samples at different redshifts, so we choose to use the NUV-r/r-J criterion which is already provided by the COSMOS2015 catalogue in the redshift range $0.1 < z < 3.5$ which is also the range of our work.

The NUV-r/r-J criterion is a two-colour selection technique which is justified in Ilbert et al. (2013) and is a slightly modified version of the technique proposed by Williams et al. (2009). Following Ilbert et al. (2010), we use the rest-frame two-colour selection $\mathrm{NUV}-r^+$ versus $r^+ - J$ instead of $U - V$ versus $V - J$. In fact, $\mathrm{NUV} - r^+$ is a better indicator of the current versus past star formation activity (e.g. Martin et al. (2007); Arnouts et al. (2007))[2]. Moreover, the dynamical range covered by the $\mathrm{NUV} - r^+$ rest-frame colour is larger than the one covered by $U-V$, making the $\mathrm{NUV}-r^+$ rest-frame colour less sensitive

[2]NUV corresponds to the GALEX filter centred at $0.23\mu m$

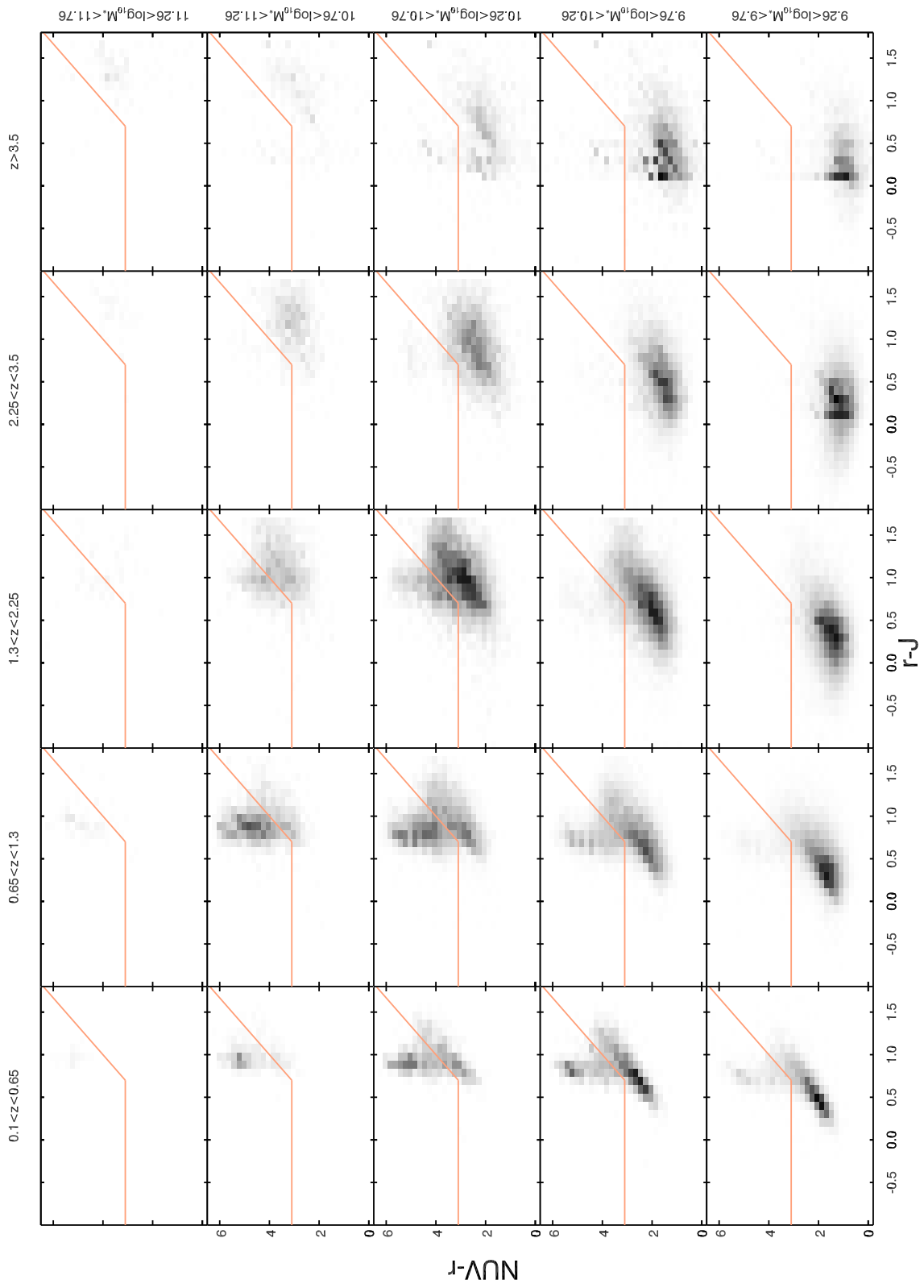

Figure 2.8: Galaxy classification based on the two colour selection from the NUV-r/r-J diagram. The orange top left box allows to select quiescent galaxies.

to uncertainties linked to observations. Finally, the NUV rest-frame is still sampled by optical data at $z > 2$ which is no longer true for the rest frame U band.

Figure 2.8 shows the two-colour criterion used to select the quiescent population for each of the mass and redshift intervals we are going to use in the rest of this work (we report $z > 3.5$ even tough we chose not to study this sample). Galaxies with $\mathrm{M_{NUV}} - \mathrm{M_r} > 3(\mathrm{M_r} - \mathrm{M_J}) + 1$ and $\mathrm{M_{NUV}} - \mathrm{M_r} > 3.1$ are considered as quiescent. The advantage of this classification is that it avoids a mix between dusty star-forming galaxies and quiescent galaxies: extinction moves star-forming galaxies along a diagonal axes from the bottom left to the top right of Fig. 2.8.

Chapter 3

X-ray data

3.1 Chandra X-ray Observatory

NASA's Chandra X-ray Observatory (CXO, or Chandra) is a space telescope designed to detect X-ray emission from high energy regions of the universe such as stellar remnants, clusters of galaxies, and matter around black holes. Because X-rays are absorbed by Earth's atmosphere, space-based telescopes are required to make these observations. Chandra is an Earth satellite in a 64-hour orbit, it was launched on Space Shuttle Columbia on July 23, 1999 and its mission is ongoing as of 2015. The Smithsonian's Astrophysical Observatory in Cambridge, MA (USA), hosts the Chandra X-ray Center (CXC) which operates the satellite, processes the data, and distributes it to scientists around the world for analysis.

The Observatory has three major parts: (1) the X-ray telescope, whose mirrors focus X-rays from celestial objects; (2) the science instruments which record the X-rays so that X-ray images can be produced and analysed; and (3) the spacecraft, which provides the environment necessary for the telescope and the instruments to work.

3.1.1 Telescope system

Chandra uses a Wolter telescope consisting of four pairs of nested cylindrical paraboloid and hyperboloid mirrors coated with iridium or gold, together with their support structure, called the High Resolution Mirror Assembly (HRMA); the mirror substrate is 2 cm-thick glass, with the reflecting surface a 33 nm iridium coating, and the diameters are 65 cm, 87 cm, 99 cm and 123 cm. The thick substrate and particularly careful polishing allowed a very precise optical surface, which is responsible for Chandra's unmatched angular resolution of $0.5''$; between 80% and 95% of the incoming X-ray energy is focused into a $1''$ circle.

3.1.2 Science instruments

The Chandra X-Ray Observatory combines the mirrors with four science instruments to capture and probe the X-rays from astronomical sources. The incoming X-rays are focused by the mirrors on the focal plane about 10 m away. The Science Instrument Module (SIM) holds the two focal plane instruments, the AXAF CCD Imaging Spectrometer (ACIS) and the High Resolution Camera (HRC), moving whichever is called for into position during an observation.

HRC has two micro-channel plate components and images over the range of 0.1–10 keV. It also has a time resolution of 16 µs. ACIS is an X-ray imager, it consists of 10 CCD

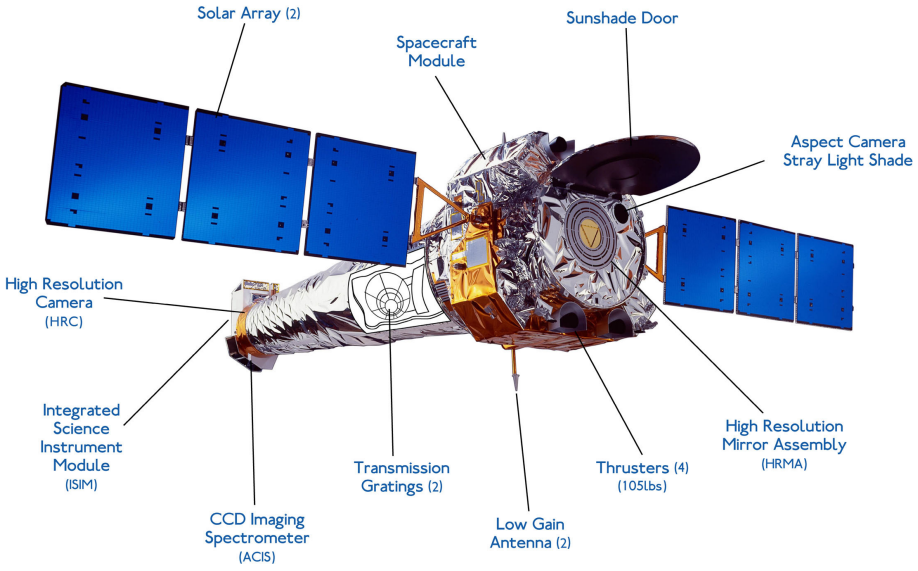

Figure 3.1: Labeled illustration of the Chandra X-ray Observatory.

chips and operates in the range of 0.2–10 keV. X-ray photons hitting the camera are detected individually and their position, energy and arrival time recorded. This allows for high resolution ($\sim 1''$) imaging, moderate resolution spectroscopy and timing studies. The instrument layout is shown in Fig. 3.3. The back illuminated S3 chip offers the best spectral resolution without using a grating. For this reason, many observers choose the back illuminated S3 chip for high resolution imaging over small (few arcminutes) fields. The largest field of view is obtained by turning on the 4 ACIS-I front illuminated chips. This configuration is often used for surveys, and was used for the COSMOS' surveys. Both ACIS and HRC can be used on their own or in conjunction with one of the Observatory's two transmission gratings.

The transmission gratings, which swing into the optical path behind the mirrors, provide Chandra with high resolution spectroscopy. The High Energy Transmission Grating Spectrometer (HETGS) works over 0.4–10 keV and has a spectral resolution of 60–1000. The Low Energy Transmission Grating Spectrometer (LETGS) has a range of 0.09–3 keV and a resolution of 40–2000.

3.2 Chandra's COSMOS data: *C-COSMOS* and *COSMOS-Legacy*

Chandra has observed the entire COSMOS field to a depth of $\sim 2 \cdot 10^{-16}\,\mathrm{erg\,cm^{-2}\,s^{-1}}$ with ACIS-I in the $0.5 - 2$ KeV band, spending nearly 2 days at each location (~ 160 ks exposure).

The first phase was the "Chandra COSMOS Survey" (*C-COSMOS*), a 1.8 Ms GO program (PI: Martin Elvis, Cycle 8) covering the central 0.9 deg^2: C-COSMOS imaged the central 0.5 deg^2 of the COSMOS field (centered at 10^h, $+02°$) with an effective exposure of ~ 160 ks, and an outer 0.4 deg^2 area with an effective exposure of ~ 80 ks (see Fig. 3.4). The limiting source detection depths are $1.9 \cdot 10^{-16}\,\mathrm{erg\,cm^{-2}\,s^{-1}}$ in the soft (0.5–2 keV) band, $7.3 \cdot 10^{-16}\,\mathrm{erg\,cm^{-2}\,s^{-1}}$ in the hard (2–10 keV) band, and $5.7 \cdot 10^{-16}\,\mathrm{erg\,cm^{-2}\,s^{-1}}$ in the full (0.5–10 keV) band. From these observations a 1761 X-ray sources catalog was

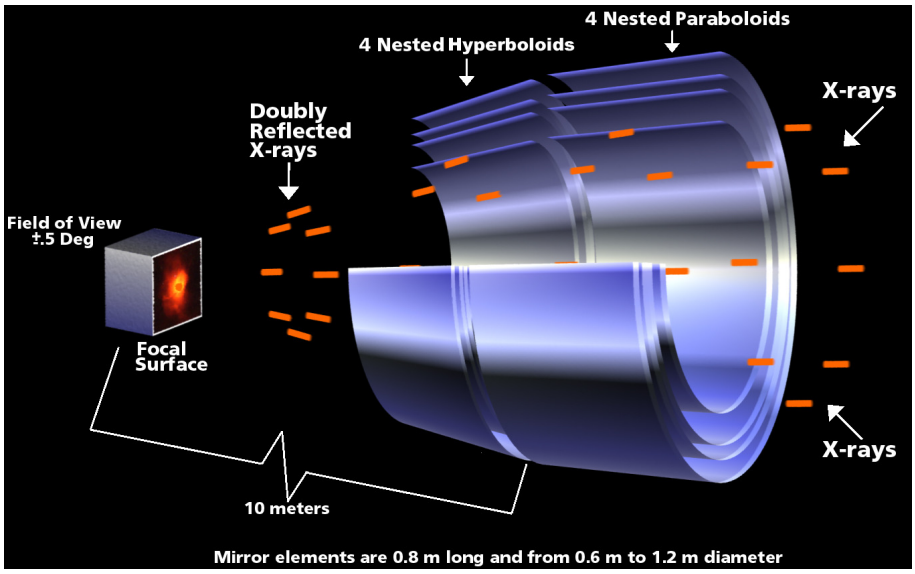

Figure 3.2: Design of the High Resolution Mirror Assembly (HRMA) on Chandra.

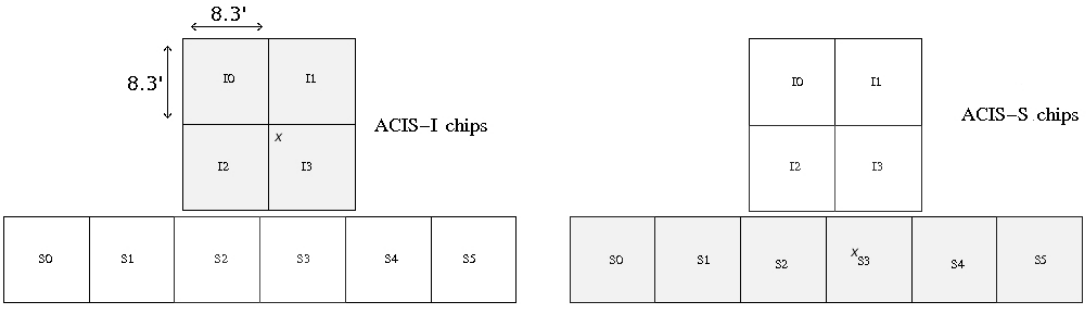

Figure 3.3: A schematic drawing of the ACIS focal plane, not to scale. The ACIS-I array consists of chips I0-I3 (shaded gray in the left figure). The ACIS-S array consists of chips S0-S5 (shaded gray in the right figure).

obtained, 97% of them having optical or infra-red counterparts. Only 2 sources are truly empty fields (Elvis et al. 2009).

The second phase was approved in Chandra Cycle 14: the 2.8 Ms "Chandra COSMOS Legacy Survey" (*COSMOS-Legacy*) (PI: Francesca Civano), the second largest Chandra GO program awarded in 14 years. *COSMOS-Legacy* uniformly covered the 1.7 deg^2 COSMOS/HST field to the same depth during 2013–2014, expanding the deep *C-COSMOS* area by a factor of ∼3 at $\sim 3 \cdot 10^{-16}$ erg cm^{-2} s^{-1} (1.45 vs 0.44 deg^2). A total area of 2.2 deg^2 has been covered (see Fig. 3.5) (Civano & Chandra COSMOS Legacy Survey Team 2013).

The Chandra COSMOS Survey has the great advantage of being deep enough to find obscured AGNs with optical galaxy continua and wide enough to have large samples and to find unusual, rare objects. Yet, the Chandra COSMOS Survey sources are bright enough that virtually all X-ray sources can be identified and followed up across their spectral energy distributions (SED).

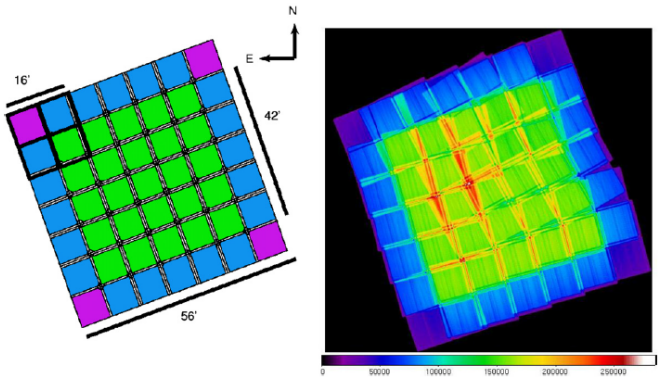

Figure 3.4: Left: the "as designed" *C-COSMOS* tiling for the 36 50 ks pointings. The thick black box (top left) represents one ACIS-I pointing, the thin boxes all the pointings. Different colors show areas with different number of overlapping pointings: green—4 overlapping pointings; blue—2 overlapping pointings; purple—1 pointing. The black bars show roughly the relative dimensions of one pointing ($\sim 16'$), of the inner area with larger exposure ($\sim 42'$), and of the total field ($\sim 56'$). Right: the as "executed" exposure map for the *C-COSMOS* survey in the soft band. The color bar gives the achieved effective exposure in units of seconds (Elvis et al. 2009) .

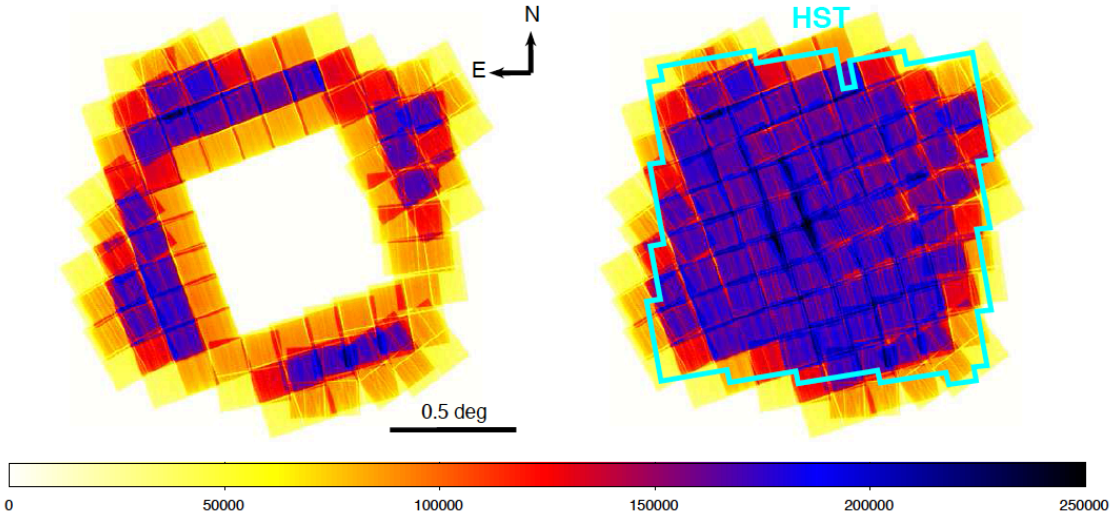

Figure 3.5: *COSMOS Legacy*: the exposure maps of the new observations (left) and the whole *COSMOS-Legacy* survey (right) in the full band. The color bar gives the achieved effective exposure in units of seconds.(Civano et al., in prep.)

3.3 X-ray sources catalogue

We start from an updated CXO COSMOS catalogue comprising all the detected sources from the two COSMOS' surveys and from the previous sample from the whole COSMOS field in the $1.5 < z < 2.5$ redshift range, divided in starbursts, normal star-forming galaxies and quiescent galaxies and in mass bins.

The new Chandra catalog is obtained from the merging of the *C-COSMOS* sources catalogue and the new *COSMOS-Legacy* catalogue. The merging catalogue contains 4054

unique X-ray sources. Sources detected in *C-COSMOS* have an identification number (ID) $< 10,000$ while sources detected in the new observvations have an ID $> 10,000$. The catalogue contains the X-coordinates of each source in degrees, a count-rate both in the soft (0.5–2 keV) and in the hard-band (2–7 keV) in units of counts s^{-1}, a flux in units of erg cm^{-2} s^{-1}, the ID of the optical counterpart as identified in Ilbert et al. (2009) catalogue and its optical coordinates.

3.4 X-ray stacking with C-STACK

Not all the optically selected sources have an X-ray counterpart, therefore we use stacking technique to determine the average count-rate of each population of undetected objects. Stacking is a powerful technique that combines the signal of multiple sources at various positions on the images. This effectively increases the signal to noise ratio of the measurement, allowing us to probe fainter fluxes than can be reached by the usual source extraction (see Fig. 3.6a). The price to pay is that we lose information about each individual source and only recover statistical properties of the sample (Schreiber et al. 2015). In our case this is not a limitation because the correlation between AGN activity and star formation can be masked if the AGN varies on much shorter time-scales than the star formation across the galaxy. In fact, observational studies (e.g. Mullaney et al. 2012b; Delvecchio et al. 2014, 2015; Rodighiero et al. 2015) have shown that when the average AGN luminosity is calculated as a function of SFR (i.e. taking the average of the more variable quantity as a function of the more stable quantity) a positive relationship is found, suggesting AGN activity and star formation are correlated on long timescales (Stanley et al. 2015).

For the X-stacking we used the CSTACK tool v4.2 developed by Takamitsu Miyaji[1] (while in Rodighiero et al. (2015) CSTACK tool v3.0 was used). CSTACK performs a stacking analysis of Chandra images from deep/wide survey data. The project started as a *C-COSMOS* consortium effort to provide a tool for COSMOS members who have catalogs of objects to obtain stacked X-ray fluxes of these objects. In addition to *C-COSMOS*, the tool currently includes *COSMOS-Legacy*, Chandra Deep Field South+North, the Extended Chandra Deep Field South and Akari NEP deep field.

The main differences between the two versions (v4.2 and v3.0) concern the source exclusion scheme. For each source position in the input list, the program looks for the nearest resolved source that meets the selection criteria. For each of the overlapped observations (fields) that have exposure at that position, it calculates the exclusion radius r_{exc}. For a given source position, each field has a different off-axis angle, and therefore a different point spread function (PSF). CSTACK version v3.0 (and before) used the 90% encircled counts fraction (ECF), r_{90} for r_{exc}. From v3.1, also the total photon count of the contaminating source in computing r_{exc} is used as:

$r_{exc} = \min\left(\max\left(r_{90}, r_{90} \cdot \sqrt{\frac{c}{c_0}}\right), r_{max}\right)$,

where c is the total photon count in the resolved source, and $c_0 = 50$ is set, and $r_{max} = 25''$. If the distance to the nearest resolved source is smaller than $r_{exc} + rad\_src$, the source/field is not included in the stacking analysis and the source/field is flagged as "X-src" in the file "stat_cts_XXXX_XXXX.dat". Also the r_{exc} regions around the resolved sources that meet the background criteria are excluded from the calculation of the background level in the stacking procedure.

The tool requires as input the dataset onto which perform the stacking analysis (*C-COSMOS* or *COSMOS-Legacy* in our case), a file containing stack positions and a set of

[1] `http://cstack.ucsd.edu/cstack`

Table 3.1: Default input parameters for the X-stacking with CSTACK.

	v4.2	v3.0
Energy Bands	Standard 2-band	Standard 2-band
Maximum off-axis angle	$8'$	$8'$
Size of the stacked image	$30''$	$12''$
Source region radius	-9	-9
Inner radius for background	$7''$	$4''$
Weight	1 for all sources	1 for all sources

parameters. These are the detailed explanations of each input field:

Root name of this job A name should be given to the job.

Energy Bands *bands* The tool has three options on the selection of energy bands: standard 2-band (0.5–2 & 2–8 keV), 6-band (0.5–0.75,0.75–1.25,1.25–2,2–3,3–5 & 5–8 keV), rest frame (3.6–4.4,4.4–5.2,5.2–6.0,6.0–6.8,6.8–7.6 & 7.6–8.4 keV rest frame).

Maximum off-axis angle *maxoff* (arcminutes) The stacking will be made over multiple observations. Only the data within this off-axis angle (at the position of the input object) of this value for each observation will be used.

Size of the stacked image *img_size* (arcseconds) The size of a side of the square field around each object, in which a stamped image and an exposure map are created.

Source region radius *rad_src* (arcseconds) The size of the circular region around this position where the image counts are extracted. If this field is -9 (-5), the source region radius varies with the off axis angle, corresponding to the 90% (50%) ECF radii, with a minimum of $1.0''$ and a maximum of *rad_bkg* (see below).

Inner radius for background *rad_bkg* (arcseconds) Background counts are accumulated from the region of the stamped image that lies outside of the circular region of this radius.

Source Exclusion Objects affected by resolved sources (either the object itself is a resolved X-ray source or the source count is heavily affected by the X-ray source) should be excluded from the stacking analysis for most sensitive stacking analysis. The source list is internal to the system.

Input file containing stacking positions The file can either be a FITS file or an ASCII file and the program automatically checks which format.

The parameters we used are reported in table 3.1 and are the default parameters. Even though we already excluded sources at $< 10''$ distance, CSTACK was allowed to discard extra objects which it found to risk to be contaminated.

We also report some details of the data and analysis procedures:

Stored data A full resolution ACIS I0–I3 image ($0.492 \times 0.492\,\mathrm{arcsec}^2$ pixels) for each of the 0.5–2 and 2–8 keV band for each observation and a corresponding exposure map, generated assuming a monochromatic 1 or 4 keV incident photons.

Data extraction For each position from the input file, for each observation, the program checks if this position is within the *maxoff* from the optical axis and it is unaffected by resolved sources. In this case, for each band, a $img\_size \times img\_size$ square post-stamp image centred at the input position (see Fig.3.6a for an example) and an exposure map covering the same area are extracted from the database.

Image counts For each band, the followings are made:

- For each object, fields (i.e. Chandra observation), the pointing centers (optical axes) of which are within *maxoff* of the object, are selected.
- For each selected field, check if the source extraction region is contaminated by the X-ray sources (see the explanation for the Source Exclusion above). If the 90% ECF region of the sources meeting the given criteria overlap with the source extraction circle, this will be flagged as "X-src".
- Count the event in the source extraction circle *rad_src*. Also extract the mean exposure of this field.
- Define the background region as the entire post-stamp image excluding 1) the circle centred at the source and the radius *rad_bkg*, and 2) the 90% ECF region around the X-ray sources meeting the exclusion from background criteria. If sufficient background area has not remained after these exclusions ($> 50\%$ of the source area), it is flagged as "bad_bkg". Get event counts and mean exposure in the background region.
- The count-rate of the source for this field is:

$$src\_rate = \frac{\frac{cts\_src}{exp\_src} - cts\_bkg/exp\_bkg/px\_bkg * px\_src}{\mathrm{ECF}}$$

- The statistics are recorded in each row of stat_cts_[band].out. The statistics on each field is designated by lbl=n, where n=1,2,3... If the neither source/background is contaminated by the X-ray sources, it is flagged as "OK".

Stacking for one object For each object, calculate exposure*weight - weighted (and normalized) mean of the rates for the "OK" fields. The statistics on each object is also added to stat_cts_[band].out, designated as lbl="sum". The Field/Comm column shows the number of the "OK" fields, or "Obj_rejected" flag if no "OK" field exist.

Stacking for all objects Similarly, calculate exposure*weight - weighted (and normalized) mean of the rates for the accepted objects. The final stacked statistics are also added to stat_cts_[band].out, designated as lbl="All".

Bootstrapping A simple photon-counting statistics is not a good way of determining the significance of the stacking, especially in case a small fraction of the objects dominate the signal. As one of the good measures, we provide the results of a bootstrap re-sampling analysis. Suppose there are N objects accepted for our stacking. Out of these, N objects are selected at random, allowing duplication and the net count-rate for these are averaged as the (exposure*weight)-weighted mean value. This defines a re-sampled stacked count-rate. The program provides the distribution of 500 such re-sampled stacked count-rates, a sorted list of these, and a histogram (for each band, see Fig.3.6b for an example).

As output CSTACK returns a tarball including the following:

results.html An output web page showing key products of the analysis results and product retrieval information.

stack_[band .img] A stacked image in raw count units (or weighted, but unnormalized, raw counts if all weights are not unity).

stack_[band .exp] A stacked effective exposure map in units of seconds. If all weights are not unity, it is a weighted, but un-normalized, exposure map.

stat_cts_[band .out] A plain ASCII file showing map statistics at each stacked position.

boot_sorteddump_[band .out] A plain ASCII file showing the stacked net count-rates for 500 bootstrap runs, incrementally sorted.

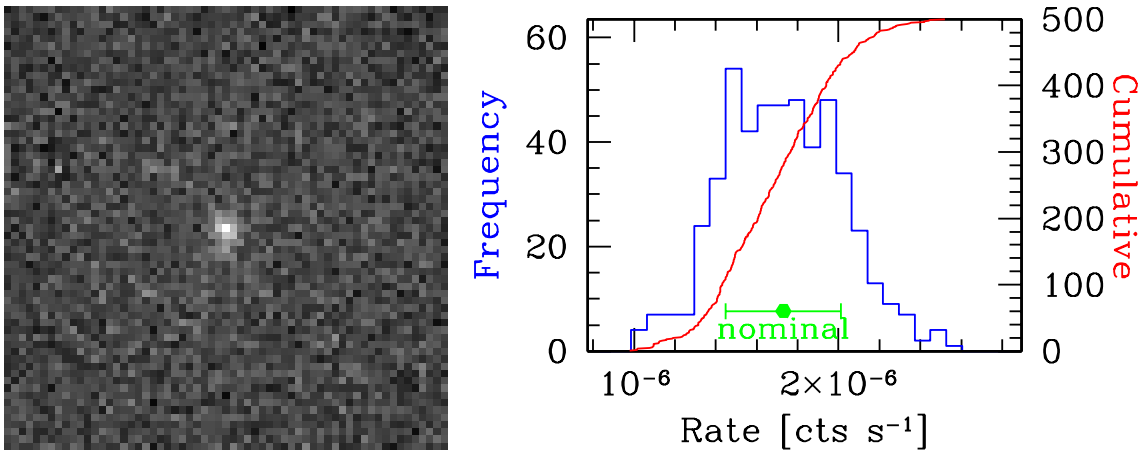

Figure 3.6: Example CSTACK output files: stack_2000_8000.exp (*Left*) and histogram created with boot_histo_2000_8000.sm (*Right*) for the COSMOS2015 data in $1.3 < z < 2.25$ and $10.5 < \log(\mathrm{M}/\mathrm{M}_{\odot}) < 11$ redshift and mass bins.

boot_histo_[band .out] A plain ASCII file showing the resulting bootstrap histogram.

rand_sorteddump_[band .out] A plain ASCII file showing the stacked net count-rates for 500 random stack, incrementally sorted.

rand_histo_[band .out] A plain ASCII file showing the resulting random stack histogram.

plot_histo_[band .sm] A SuperMongo script which produces the bootstrap/random stack histogram plots.

stackanalysis.log A detailed log of the stacking analysis which has been made at the server.

finished.txt This file is created when the job is finished. Useful for the users who use their own automated script to run this tool at the client side.

Chapter 4

Extension of Rodighiero et al. (2015) work to COSMOS-Legacy

In this chapter we extend the work of Rodighiero et al. (2015) on the *C-COSMOS* area to the *COSMOS-Legacy* survey. In order to do this we first repeat the X-stacking analysis for the sample of Rodighiero et al. (2015) (section 2.3.1) on *C-COSMOS* with the new version of the stacking tool to check for concordance. Then we extend the analysis to the whole COSMOS field to obtain better statistics and we transform the count-rates from the stacking and from the CXO detected sources into fluxes and average them. From this we obtain the luminosities of each population of objects and compare them to the previous results.

4.1 X-detected and stacking sources

The sample used in Rodighiero et al. (2015) is sorted in sub-catalogue files between galaxy type (star-forming, quiescents, starburts) and mass intervals.

For the first stacking on C-COSMOS, whose only aim is to check for concordance between the old (v3.0) and the new (v4.2) version of the stacking tool, we simply use as input stacking positions the sub-catalogue as they are and leave to the tool the source exclusion. For the stacking on COSMOS-Legacy we proceed as follows.

We notice that not all of the Chandra sources are detected both in the hard and in the soft band. For these sources we estimate the missing band count-rate assuming a power-law spectrum with spectral index $\Gamma = 1.4$ and we convert the ACIS-I count-rate from 0.5–2 keV to 2–8 keV (or vice-versa) using WebPIMMS tool[1]. The conversion factors are:

$$\mathrm{CR}(0.5-2\,\mathrm{keV}) = 1.182 \times \mathrm{CR}(2-8\,\mathrm{keV}),$$

$$\mathrm{CR}(2-8\,\mathrm{keV}) = 0.8463 \times \mathrm{CR}(0.5-2\,\mathrm{keV}).$$

For these sources we consider only the half of the estimated count-rate, for we have estimated a count-rate upper limit.

In order to calculate the average X-ray luminosity of each sub-catalogue we need to first separate the X-ray detected sources from the not detected ones and to discard the objects near an X-detected source, because they risk of being contaminated from the source's flux. The not X-detected sources are going to be stacked as explained in section 3.4.

Using a catalogue handling macro for IDL (cccpro.pro, written by Mattia Vaccari) we

[1] `http://heasarc.gsfc.nasa.gov/cgi-bin/Tools/w3pimms/w3pimms.pl`

Table 4.1: Comparison between stacking on C-COSMOS with CSTACK v3.0 (from Rodighiero et al. (2015)) and v4.2. $N_{stacked}$ is the number of stacked sources of the sub-catalogue, $CR_{2-8\,keV}$ is the count-rate obtained from the stacking and PE is the associated Poissonian error.

	v.3.0		v.4.2	
log(Mass range)	$N_{stacked}$	$CR_{2–8\ keV}[s^{-1}]$	$N_{stacked}$	$CR_{2\text{-}8\ keV}[s^{-1}]$
Main sequence				
10.09–10.42	3215	1.40e-6 ± 5.10e-7	3474	1.17e-06 ± 4.97e-07
10.42–10.75	2158	2.78e-6 ± 6.37e-7	2302	3.80e-06 ± 6.24e-07
10.75–11.25	984	6.71e-6 ± 9.78e-7	1068	5.62e-06 ± 9.38e-07
11.25–12	36	1.37e-5 ± 5.18e-6	38	1.35e-05 ± 5.20e-06
Starbursts above MS				
10.5–11.0	48	4.13e-7 ± 3.98e-5	50	-5.02e-07 ± 4.36e-06
11.0–12.0	25	1.38e-5 ± 6.05e-6	28	1.12e-05 ± 6.13e-06
Quiescents below MS				
10.42–10.75	381	2.89e-6 ± 1.60e-6	411	3.71e-06 ± 1.57e-06
10.75–11.25	627	1.34e-6 ± 1.18e-6	680	-1.39e-07 ± 1.14e-06

matched each sub-catalogue with the Chandra Catalogue of section 3.3 and created two sub-sub-catalogues, one with X-detected sources only and one with sources to be stacked only. To obtain the X-detected sources only catalogue we matched the X-ray coordinates from the Chandra catalogue with the optical coordinates in the sub-catalogue and kept sources within a $0.5''$ distance. For the stacking catalogue we discarded objects within a $10''$ distance from the optical counterpart of an X-detected source.

4.2 Stacking results

4.2.1 Accordance between CSTACK v3.0 and v4.2

For all the sub-catalogue (stacking only sources) we perform stacking analysis first in the *C-COSMOS* field and then in the whole *COSMOS-Legacy*. The *C-COSMOS* analysis is repeated because in Rodighiero et al. (2015) the stacking analysis was performed using former CSTACK v3.0[2] and we need to check for accordance with the new one, v4.2[3].

Stacking on *C-COSMOS* with CSTACK v4.2 returned almost identical results as with v3.0 (results from Rodighiero et al. (2015)) as can be seen in the comparative table 4.1. We notice that the new exclusion scheme led to systematically higher number of stacking sources, but the results remain almost unchanged.

4.2.2 Comparison between stacking on C-COSMOS and COSMOS-Legacy

We performed the stacking again, this time with *COSMOS-Legacy* and in table 4.2 we report a comparison between the stacking on C-COSMOS and COSMOS-Legacy. As expected the number of stacked sources has doubled and consequently the Poissonian error has decreased

[2] `http://cstack.ucsd.edu/cstack_v3/`
[3] `http://cstack.ucsd.edu/cstack_v4.2/`

Table 4.2: Comparison between stacking on C-COSMOS and stacking on COSMOS-Legacy both with CSTACK v4.2. $N_{stacked}$ is the number of stacked sources of the sub-catalogue, $CR_{2-8\,keV}$ is the count-rate obtained from the stacking and PE is the associated Poissonian error.

	C-COSMOS		COSMOS-Legacy (clean)	
log(Mass range)	$N_{stacked}$	$CR_{2–8\ keV}[s^{-1}]$	$N_{stacked}$	$CR_{2\text{-}8\ keV}[s^{-1}]$
Main sequence				
10.09–10.42	3474	1.17e-06 ± 4.97e-07	7121	1.07e-06 ± 2.99e-07
10.42–10.75	2302	3.80e-06 ± 6.24e-07	4563	2.88e-06 ± 3.79e-07
10.75–11.25	1068	5.62e-06 ± 9.38e-07	2131	5.68e-06 ± 5.72e-07
11.25–12	38	1.35e-05 ± 5.20e-06	71	1.43e-05 ± 3.42e-06
Starbursts above MS				
10.5–11.0	50	-5.02e-07 ± 4.36e-06	108	3.15e-06 ± 2.53e-06
11.0–12.0	28	1.12e-05 ± 6.13e-06	57	8.36e-06 ± 3.55e-06
Quiescents below MS				
10.42–10.75	411	3.71e-06 ± 1.57e-06	803	3.04e-06 ± 9.10e-07
10.75–11.25	680	-1.39e-07 ± 1.14e-06	1347	1.91e-06 ± 7.01e-07
11.25–12.00	94	5.11e-06 ± 3.43e-06	188	5.20e-06 ± 1.89e-06

4.3 Average flux and luminosity calculation

We then calculated the average flux for the 2–10 keV band in the same way as in Rodighiero et al. (2015) with the formula

$$F_{\rm ave} = \frac{\sum_{i=1}^{n_{\rm detected}} F_{i,\rm detected} + n_{\rm stacked} \cdot F_{\rm stacked}}{n_{\rm detected} + n_{\rm stacked}}. \tag{4.1}$$

In order to do this we had to first convert count-rates (observing 2–8 keV band) into rest-frame fluxes (standard 2-10 keV band) and propagate the error associated with each count-rate measure. For the conversion from count-rate to flux we assume a power law spectrum for the AGN with index $\Gamma = 1.4$, an average redshift $z = 2$ and no hydrogen absorption ($N_H = 0\,cm^{-2}$). We used the formula:

$$F = CR \cdot K_{corr} \cdot CF \tag{4.2}$$

where CR is the count-rate, K_{corr} is the K correction due to the redshift, calculated as

$$K_{corr} = (1+z)^{\Gamma-2}, \tag{4.3}$$

which for our parameters is $K_{corr} = 0.52$ and CF$= 2.75 \cdot 10^{-11}$ is the conversion factor from count-rate to flux, calculated using WebPIMMS (in the above bands and for the given parameters).

For the error propagation we used the Monte Carlo method performing $N_s = 10^5$ simulations for each measure. For the detected sources we assumed a Gaussian probability distribution centred on the $F_{\rm detected}$ with a standard deviation $\sigma = 0.25 \cdot F_{\rm detected}$ (25% of the measure). For the stacked sources we used the bootstrap probability distribution obtained from CSTACK's output "boot_sorteddump_2000_8000.out", we interpolate its

Table 4.3: Fluxes for each sub-catalogue, $< F_{\text{stacked,2-10 keV}} >$ is the obtained flux from stacked sources only and $< F_{\text{total,2-10 keV}} >$ is the average flux obtained considering both stacked and detected sources.

Mass range $\log_{10}(M_\odot)$	$< M_* >$ $\log_{10}(M_\odot)$	N_{stacked}	N_{detected}	$< F_{\text{stacked,2-10 keV}} >$ $10^{-17}\,\text{erg}\,\text{s}^{-1}\,\text{cm}^{-2}$	$< F_{\text{total,2-10 keV}} >$ $10^{-17}\,\text{erg}\,\text{s}^{-1}\,\text{cm}^{-2}$
Main sequence					
10.09–10.42	10.25 ± 0.10	7121	117	$1.53^{+0.77}_{-0.78}$	$4.41^{+0.77}_{-0.76}$
10.42–10.75	10.57 ± 0.09	4563	253	$4.12^{+0.92}_{-0.85}$	$17.1^{+1.1}_{-1.1}$
10.75–11.25	10.92 ± 0.12	2131	251	$8.0^{+1.4}_{-1.4}$	$42.1^{+2.1}_{-2.2}$
11.25–12	11.35 ± 0.11	71	21	$20.4^{+8.9}_{-8.5}$	169^{+23}_{-23}
Starbursts above MS					
10.5–11.0	10.52 ± 0.15	108	20	$4.5^{+5.9}_{-5.8}$	$60.5^{+9.0}_{-8.8}$
11.0–12.0	10.92 ± 0.13	57	15	$12.8^{+9.8}_{-11.7}$	123^{+18}_{-18}
Quiescents below MS					
10.42–10.75	10.61 ± 0.09	803	15	$4.3^{+2.0}_{-1.9}$	$7.9^{+2.1}_{-2.0}$
10.75–11.25	10.97 ± 0.13	1347	47	$2.7^{+1.7}_{-1.7}$	$9.8^{+1.8}_{-1.8}$
11.25–12.25	11.38 ± 0.11	188	8	$7.3^{+5.0}_{-4.5}$	87^{+31}_{-31}

cumulative curve with the values obtained from a continuous uniform distribution simulation and obtain a set of N_s simulated fluxes following the bootstrap distribution. Then we calculate equation (4.1) N_s times, one for each simulated flux (index j)

$$F_{ave,j} = F_{ave}(F_{\text{detected},j}, F_{\text{stacked},j}),$$

this gives us an average flux probability distribution and from its cumulative we take as F_{ave} the interpolated median value (50% of cumulative curve) and the 90% confidence levels (5% and 95% of the cumulative curve). We report on table 4.3 the fluxes obtained, for the stacking only and for stacking plus detected sources.

Finally we converted the average fluxes to average luminosities through the equation

$$< L_{\text{2-10 keV}} >= 4\pi D_L^2 \cdot F_{ave} \tag{4.4}$$

where $D_L = 15.74\,\text{Gpc}$ is the luminosity distance calculated with the cosmological parameters $\Omega_\lambda = 0.73$, $\Omega_M = 0.27$, $H_0 = 71\,\text{km}\,\text{s}^{-1}\,\text{Mpc}^{-1}$ and $z = 2$ (same as Rodighiero et al. (2015), already reported at the end of chapter 1). We report the average luminosities for each sub-catalogue in table 4.4 and in figure 4.1.

4.4 Hardness ratio analysis

In X-ray astronomy, a hardness ratio (HR) is the equivalent of a photometric color index, and is calculated as a normalized difference of the exposure corrected counts in two energy bands A (high energy), B (low energy). A typical definition is HR$= (A-B)/(A+B)$ but other schemes are also used (Giacconi et al. 2002).

Although most X-ray sources emit X-rays at a range of energies, different sources will have different emission profiles - for example, black holes and X-ray binaries typically

Table 4.4: Average X-ray luminosities for the sample of Rodighiero et al. (2015) computed with *COSMOS-Legacy* data.

Mass range $\log_{10}(M_\odot)$	$< M_* >$ $\log_{10}(M_\odot)$	$N_{stacked}$	$N_{detected}$	$< L_{2\text{-}10\ keV} >$ $10^{42}\,erg\,s^{-1}$
Main sequence				
10.09–10.42	10.25 ± 0.10	7121	117	$1.31^{+0.23}_{-0.23}$
10.42–10.75	10.57 ± 0.09	4563	253	$5.07^{+0.32}_{-0.32}$
10.75–11.25	10.92 ± 0.12	2131	251	$12.48^{+0.64}_{-0.63}$
11.25–12	11.35 ± 0.11	71	21	$50.1^{+6.8}_{-6.9}$
Starbursts above MS				
10.5–11.0	10.52 ± 0.15	108	20	$18.0^{+2.7}_{-2.7}$
11.0–12.0	10.92 ± 0.13	57	15	$35.2^{+5.3}_{-5.4}$
Quiescents below MS				
10.42–10.75	10.61 ± 0.09	803	15	$2.33^{+0.62}_{-0.59}$
10.75–11.25	10.97 ± 0.13	1347	47	$2.91^{+0.52}_{-0.53}$
11.25–12.25	11.38 ± 0.11	188	8	$25.7^{+9.1}_{-9.2}$

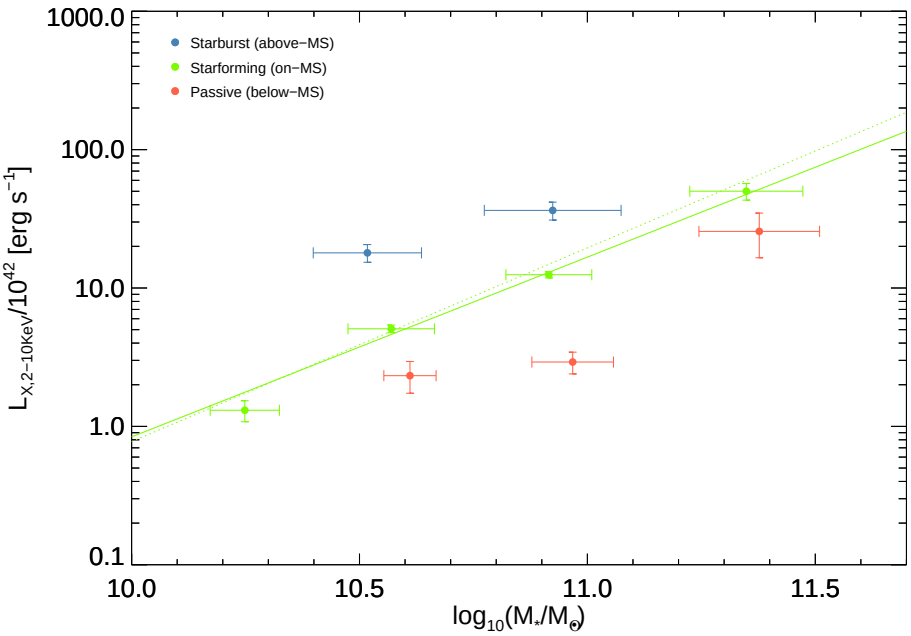

Figure 4.1: Stellar mass-average luminosity relation at $1.5 < z < 2.5$ from our X-ray stacking analysis for our three samples: starburst (blue), main sequence (green), quiescent sources (red). Horizontal error bars show the mass dispersion, vertical error bars show the 90% confidence interval. The green dotted line is the fit for the main sequence sample as in Rodighiero et al. (2015), $\log[L_X] = 1.40(\pm 0.09) \times \log[M_*] - 14.11$. The green solid line is the fit to our data $\log[L_X] = 1.30(\pm 0.15) \times \log[M_*] - 13.07$.

emit a large fraction of their X-rays at high energies, whereas the hot gas seen in elliptical galaxies and starbursts usually has only a small high energy component. These differences are a consequence of the different physical processes which produce the X-rays. It is also important to note that the energy of the X-rays emitted is often determined by the temperature of a thermal source: astronomical objects are sometimes found to have temperatures of millions of Kelvin, so the peak energy of the photons they emit is in the X-ray regime.

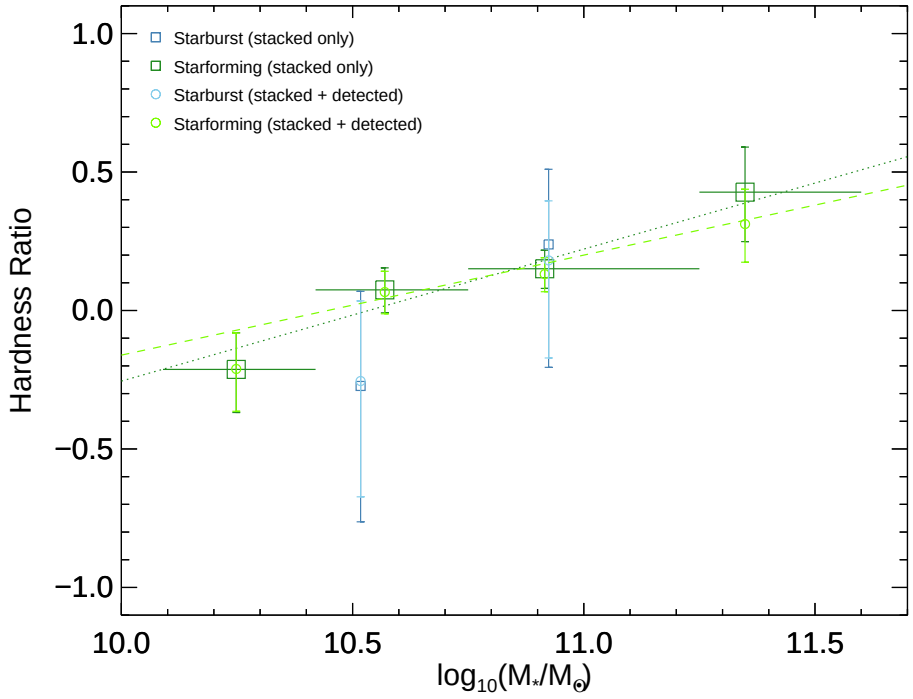

Figure 4.2: Stellar mass - hardness ratio relation at $1.5 < z < 2.5$ for the main sequence and starburst samples. For both samples the average ratio is reported for the stacked sources only and for the detections plus the stacked sources. The vertical error bars show the 68.3% confidence level, while the horizontal error bars show the mass dispersion. The dotted line is a linear fit for the main sequence stacked only sample ($\mathrm{HR} = 0.48(\pm 0.17) \times \log[\mathrm{M}_*] - 5.02$) and the dashed line for the main sequence stacked plus detected sources ($\mathrm{HR} = 0.36(\pm 0.27) \times \log[\mathrm{M}_*] - 3.77$).

In general terms, we refer to an X-ray source as being "hard" if a large percentage of its X-ray emission is at higher X-ray energies, or "soft" if it mainly produces lower energy photons. The "hardness" of a source therefore gives us a rough idea of what sort of X-ray emission we are looking at, and sometimes the temperature of the source. A more accurate estimate can be obtained by calculating hardness ratios. If we observe an X-ray source and then construct images in different energy bands, we can count the number of photons we have detected in each band, and calculate the ratios between them. By using standard bands when looking at different sources, we can find out what ratios we would expect for each different type of object. Then, an object's observed hardness ratio will allow us to classify it quickly.

From the ratio of the soft (S, 0.5–2 keV) and hard (H, 2–10 keV) bands count rates we derived the Hardness Ratio, HR

$$\mathrm{HR} = \frac{\mathrm{H} - \mathrm{S}}{\mathrm{H} + \mathrm{S}}. \tag{4.5}$$

The values of the HR are the average distribution values derived again using the Monte Carlo simulations as in section 4.3 simulating 10^6 times the distribution of the corresponding stacked count rate. We also simulated the detections' count rate (again, assuming a normal distribution with a 25% error) and averaged it with the HR of the stacked sample for each mass bin for the MS and starburst populations using the equation

$$\mathrm{HR}_{\mathrm{tot}} = \frac{\sum_{i=1}^{n_{\mathrm{detected}}} \mathrm{HR}_{i,\mathrm{detected}} + n_{\mathrm{stacked}} \cdot \mathrm{HR}_{\mathrm{stacked}}}{n_{\mathrm{detected}} + n_{\mathrm{stacked}}} \tag{4.6}$$

which is analogous to eq. (4.1).

4.5 Comparison with Rodighiero et al. (2015)

The plot showing the average $\mathrm{L_X}$ vs. $\mathrm{M_*}$ for the MS, staburst and quiescent samples is shown in figure 4.1. With respect to Rodighiero et al. (2015) we were able to add a point at higher mass for the quiescent population, thanks to the increased number of sources. This increase also allowed to reduce the error bars and to confirm the position in the $\mathrm{L_X}$-$\mathrm{M_*}$ plane of the three galaxy subsamples. We provide a fit for the MS sample (solid green line) with equation

$$\log[\mathrm{L_X}] = 1.30(\pm 0.15) \times \log[\mathrm{M_*}] - 13.07. \tag{4.7}$$

For comparison the relation from Rodighiero et al. (2015) is also shown (green dotted line). The two relations are compatible within the errors and indicate a superlinear dependence of X-ray luminosity on galactic mass.

In Fig. 4.2 we show the HR calculated for the stacked only and for the stacked plus detected galaxies. This shows a hardening of the X-ray spectra towards higher stellar masses. This trend was already found in the MS galaxies of Rodighiero et al. (2015), but the trend was also compatible with being flat. Furthermore they were not they able to say anything about the starburts. With our reduced error bars instead, we can assert that for this sample the MS' HR trend clearly hardens and the starbursts' HR is compatible, within the error bars, with the MS'. Since the HR is a measure of the average obscuration, this shows that the starbursts are obscured as much as the MS galaxies and therefore their X-ray luminosity $\mathrm{L_X}$ (see Fig. 4.1 and table 4.4) is not under or overestimated. This confirms that starburst galaxies are on average, not only more star-forming, but also more active in the nucleus than the MS galaxies.

Chapter 5

Constraints on the history of star formation and BH accretion in galaxies

We repeat the X-ray emission study in the COSMOS field this time selecting our galaxy sample from the COSMOS2015 catalogue. This will allow us to cover a much broader redshift range—so we will sort the sample in different redshift bins—and to reach lower masses than previously. The presence of many redshift bins will also give us the possibility to study the evolution of our sample. Starburst galaxies are on average more obscured in the optical-NIR bands, so classifications based on these observations often place them on the MS of star-forming galaxies (SFG) (Rodighiero et al. 2014). To select a sample of sturburst galaxies FIR observations—where the absorbed flux is re-emitted—are required. Unluckily the COSMOS2015 catalogue does not include it so we will be able to select just a SFG and passive galaxies sample.

5.1 Comparison between L_X from the BzK selection and from NUV-r/r-J

Before starting the real work with the new sample, we want to check whether gives similar results to the ones we got with the $sBzK$ sample so we choose a star-forming sample in the same redshift interval, $1.5 < z < 2.5$, in the UltraVISTA Ultra-deep area (see Fig. 2.4), with an apparent magnitude $K_s < 24.7$, which is the 3σ source detection limit. We use the same mass intervals as we are going to use in the rest of the work, separate the detected from the stacking sources, run CSTACK v4.2 and proceed as in section 4.3 for the flux and luminosity calculations. We report in table 5.1 the comparison sample's details and in Fig. 5.1 the L_X-stellar mass relations for the two samples. We notice that the slope obtained with the COSMOS2015 sample ($\log[L_X] = 1.17(\pm 0.18) \times \log[M_*] - 11.87$) is less steep than that of the $sBzK$ selected sample (eq. 4.7). If we compare the data in tables 4.4 and 5.1 we notice that the detected fraction is a bit lower for the COSMOS2015 sample (24% against 30% for the highest mass bin), so this could be the reason of the difference.

5.2 Stacking the entire sample

We divide the COSMOS2015 sample (SF and quiescent) in the mass and redshift intervals reported as in Fig. 2.8 (but we do not consider the $z > 3.5$ bin).

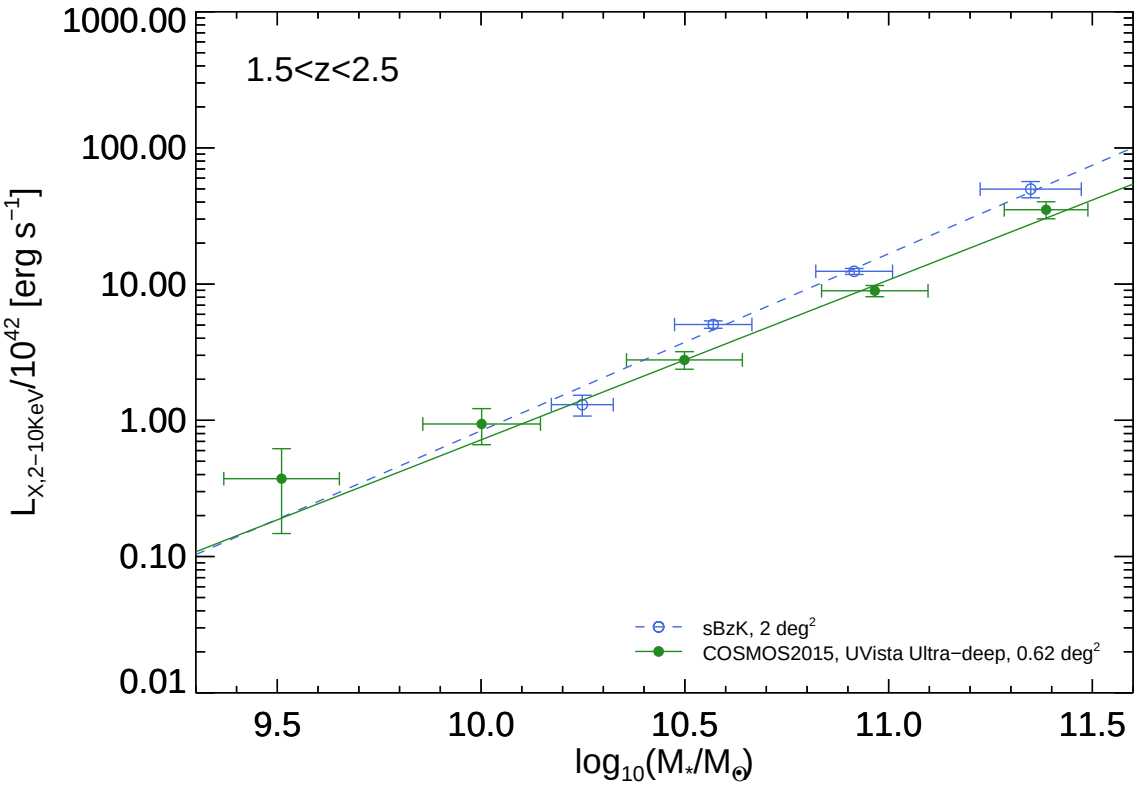

Figure 5.1: star-forming galaxies' main sequence for the $sBzK$ sample on the 2 deg^2 and for the COSMOS2015 Ultra-deep UVista (0.62 deg^2) with magnitude $K_s < 24.7$, whose best fit is $\log[L_X] = 1.17(\pm 0.18) \times \log[M_*] - 11.87$.

Table 5.1: Statistics for the SF NUV − r/r − J sample in $1.5 < z < 2.5$.

Mass range $\log_{10}(M_\odot)$	$< M_* >$ $\log_{10}(M_\odot)$	$< z >$	$N_{stacked}$	$N_{detected}$	$< L_{2\text{-}10\ keV} >$ 10^{42} erg s^{-1}
9.26–9.76	9.51 ± 0.14	1.95 ± 0.29	5189	5	$0.37^{+0.25}_{-0.23}$
9.76–10.26	10.00 ± 0.14	1.94 ± 0.28	3659	22	$0.94^{+0.28}_{-0.28}$
10.26–10.76	10.50 ± 0.14	1.92 ± 0.27	2219	81	$2.75^{+0.41}_{-0.40}$
10.76–11.26	10.97 ± 0.13	1.96 ± 0.27	856	83	$8.92^{+0.83}_{-0.86}$
11.26–11.76	11.39 ± 0.10	1.98 ± 0.27	88	21	$35.2^{+5.1}_{-5.0}$

We proceed as in section 4.1 for the catalogues' matching and then run CSTACK tool (see sec. 3.4 for a description) to stacking the selected sources. The numbers of stacked and detected sources are reported in tables 5.2 and 5.3.

5.3 X-ray luminosity evolution

We proceed as in sec. 4.3 for flux and luminosity calculations. This time for each mass and redshift interval we calculate the average redshift (tables 5.2 and 5.3) and use it for the K correction and for the luminosity distance computations, again via eq (4.3) and (4.4),

Table 5.2: Statistics for the SF NUV − r/r − J sample.

Mass range $\log_{10}(M_\odot)$	$< M_* >$ $\log_{10}(M_\odot)$	$< z >$	$N_{stacked}$	$N_{detected}$	$< L_{2\text{-}10\ keV} >$ $10^{42}\,erg\,s^{-1}$	$< SFR >$ $M_\odot\,yr^{-1}$	$\frac{L_{SF}}{<L_{tot}>}(2\text{-}10keV)$
$0.1 < z < 0.65$							
9.26–9.76	9.49 ± 0.14	0.45	5551	27	$0.0122^{+0.0061}_{-0.0050}$	$2.003^{+0.024}_{-0.024}$	0.29
9.76–10.26	10.0 ± 0.14	0.44	3209	60	$0.0807^{+0.0092}_{-0.0094}$	$6.375^{+0.028}_{-0.028}$	0.16
10.26–10.76	10.49 ± 0.14	0.44	1663	95	$0.295^{+0.023}_{-0.024}$	$19.358^{+0.069}_{-0.069}$	0.14
10.76–11.26	10.94 ± 0.13	0.43	516	83	$1.40^{+0.18}_{-0.18}$	$27.36^{+0.20}_{-0.20}$	0.05
11.26–11.76	11.38 ± 0.08	0.35	17	6	$0.88^{+0.18}_{-0.18}$	$18.99^{+0.30}_{-0.28}$	0.05
$0.65 < z < 1.3$							
9.26–9.76	9.5 ± 0.14	0.99	18592	47	$0.074^{+0.022}_{-0.020}$	$4.763^{+0.046}_{-0.046}$	0.14
9.76–10.26	10.0 ± 0.14	0.99	10872	90	$0.239^{+0.033}_{-0.035}$	$16.23^{+0.11}_{-0.11}$	0.14
10.26–10.76	10.49 ± 0.14	0.99	5868	287	$1.213^{+0.066}_{-0.065}$	$39.7^{+4.5}_{-4.3}$	0.07
10.76–11.26	10.95 ± 0.13	1.00	1756	195	$3.50^{+0.24}_{-0.23}$	$58.90^{+0.30}_{-0.30}$	0.04
11.26–11.76	11.37 ± 0.09	1.02	106	24	$6.04^{+0.76}_{-0.75}$	$73.8^{+1.6}_{-1.6}$	0.03
$1.3 < z < 2.25$							
9.26–9.76	9.55 ± 0.14	1.75	20402	38	$0.231^{+0.091}_{-0.093}$	$10.31^{+0.19}_{-0.17}$	0.10
9.76–10.26	10.00 ± 0.14	1.74	12643	84	$0.48^{+0.11}_{-0.11}$	$32.70^{+0.26}_{-0.26}$	0.14
10.26–10.76	10.50 ± 0.14	1.73	7845	295	$2.29^{+0.17}_{-0.16}$	$72.86^{+0.64}_{-0.64}$	0.07
10.76–11.26	10.96 ± 0.13	1.78	3038	289	$7.14^{+0.38}_{-0.39}$	$140.26^{+0.86}_{-0.86}$	0.05
11.26–11.76	11.39 ± 0.1	1.80	308	58	$21.7^{+2.6}_{-2.6}$	$199.0^{+3.3}_{-3.3}$	0.02
$2.25 < z < 3.5$							
9.26–9.76	9.51 ± 0.14	2.82	15900	4	—	$12.82^{+0.83}_{-1.74}$	—
9.76–10.26	9.99 ± 0.14	2.86	9910	44	$0.26^{+0.38}_{-0.38}$	$58.1^{+1.9}_{-1.4}$	0.36
10.26–10.76	10.49 ± 0.14	2.81	4523	126	$4.21^{+0.56}_{-0.58}$	$185.8^{+3.0}_{-3.0}$	0.10
10.76–11.26	10.97 ± 0.14	2.73	1680	141	$13.8^{+1.2}_{-1.2}$	$270.0^{+2.6}_{-2.7}$	0.05
11.26–11.76	11.41 ± 0.11	2.79	240	31	$25.8^{+3.3}_{-3.3}$	$542.4^{+3.9}_{-10.9}$	0.05

respectively. We also compute a luminosity error due to the redshift distribution of the sample. We consider the 5% and 95% percentiles of the redshift distribution in each redshift and mass bin, we compute the luminosity distance D_L at both redshift values and finally the corresponding X-ray luminosity, as in eq. (4.4). These two X-ray luminosity values make our error ΔL_2. The luminosity errorbars used are the sum of squared errors due to the count-rate uncertainty (ΔL_1, see sec. 4.3) and due to the redshift distribution just described:

$$\Delta L_{tot} = \sqrt{(\Delta L_1)^2 + (\Delta L_2)^2}. \tag{5.1}$$

From a first check we notice that the X-ray luminosity of SFG, especially in the lowest redshift and mass bins, is quite low (below $10^{42}\,erg\,s^{-1}$), therefore we cannot neglect the X-ray luminosity due to star formation. We consider the SFRs for each redshift and mass interval (see sec. 5.4) and estimate the resulting X-ray luminosity as in (Vattakunnel et al. 2012, eq. 6):

$$L_{2-10\,keV}[\,erg\,s^{-1}] = \frac{10^{40}}{1.40 \pm 0.32} \times SFR[\,M_\odot\,yr^{-1}]. \tag{5.2}$$

Table 5.3: Statistics for the quiescent NUV − r/r − J sample.

Mass range $\log_{10}(M_\odot)$	$< M_* >$ $\log_{10}(M_\odot)$	$< z >$	$N_{stacked}$	$N_{detected}$	$< L_{2\text{-}10\ keV} >$ $10^{42}\,erg\,s^{-1}$
$0.1 < z < 0.65$					
9.26–9.76	9.52 ± 0.15	0.44	614	2	$0.0076^{+0.0170}_{-0.0076}$
9.76–10.26	10.03 ± 0.14	0.46	764	7	$0.033^{+0.017}_{-0.017}$
10.26–10.76	10.53 ± 0.14	0.48	956	27	$0.165^{+0.024}_{-0.025}$
10.76–11.26	10.98 ± 0.14	0.48	678	41	$0.278^{+0.030}_{-0.030}$
11.26–11.76	11.43 ± 0.11	0.48	117	23	$0.80^{+0.15}_{-0.15}$
$0.65 < z < 1.3$					
9.26–9.76	9.53 ± 0.15	0.88	730	0	—
9.76–10.26	10.05 ± 0.14	0.91	1718	10	$0.056^{+0.059}_{-0.056}$
10.26–10.76	10.54 ± 0.14	0.93	3196	63	$0.293^{+0.049}_{-0.049}$
10.76–11.26	10.98 ± 0.14	0.94	2701	130	$1.204^{+0.091}_{-0.092}$
11.26–11.76	11.40 ± 0.10	0.92	416	29	$1.60^{+0.21}_{-0.22}$
$1.3 < z < 2.25$					
9.26–9.76	9.55 ± 0.14	1.77	238	2	—
9.76–10.26	10.07 ± 0.13	1.66	507	3	$0.09^{+0.54}_{-0.094}$
10.26–10.76	10.55 ± 0.14	1.65	991	38	$1.77^{+0.35}_{-0.36}$
10.76–11.26	10.98 ± 0.14	1.62	884	28	$2.50^{+0.46}_{-0.44}$
11.26–11.76	11.4 ± 0.12	1.64	125	3	$1.95^{+1.03}_{-0.99}$
$2.25 < z < 3.5$					
9.26–9.76	9.53 ± 0.14	2.68	90	1	$0.80^{+3.22}_{-0.80}$
9.76–10.26	10.04 ± 0.14	2.64	137	1	—
10.26–10.76	10.53 ± 0.15	2.66	183	4	$5.1^{+2.7}_{-2.6}$
10.76–11.26	10.96 ± 0.13	2.63	128	7	$9.3^{+3.4}_{-3.5}$
11.26–11.76	11.36 ± 0.08	2.45	8	1	18^{+13}_{-12}

As expected, the fraction of X-ray luminosity due to SF from eq. (5.2) is not negligible in many bins (up to $\sim 30\%$, see table 5.2), so we subtract it to the total X-ray luminosity estimated as in section 4.3. Finally we show the X-ray luminosity–mass average relation for both the star-forming and quiescent samples in our four redshift intervals in Fig. 5.2. The horizontal error bars show the mass dispersion while the vertical error bars show the 90% confidence interval (0.05 and 0.95 percentiles). The vertical light blue dashed lines show the mass completeness limit (90%) for each redshift bin from Laigle et al. (in prep.). We also report results from Mullaney et al. (2012b) (scaled to the same K correction adopted in this work) in the closest redshift bins (his are $0.5 < z < 1.5$ and $1.5 < z < 2.5$) and our main sequence from Fig. 4.1, which is within $1.5 < z < 2.5$.

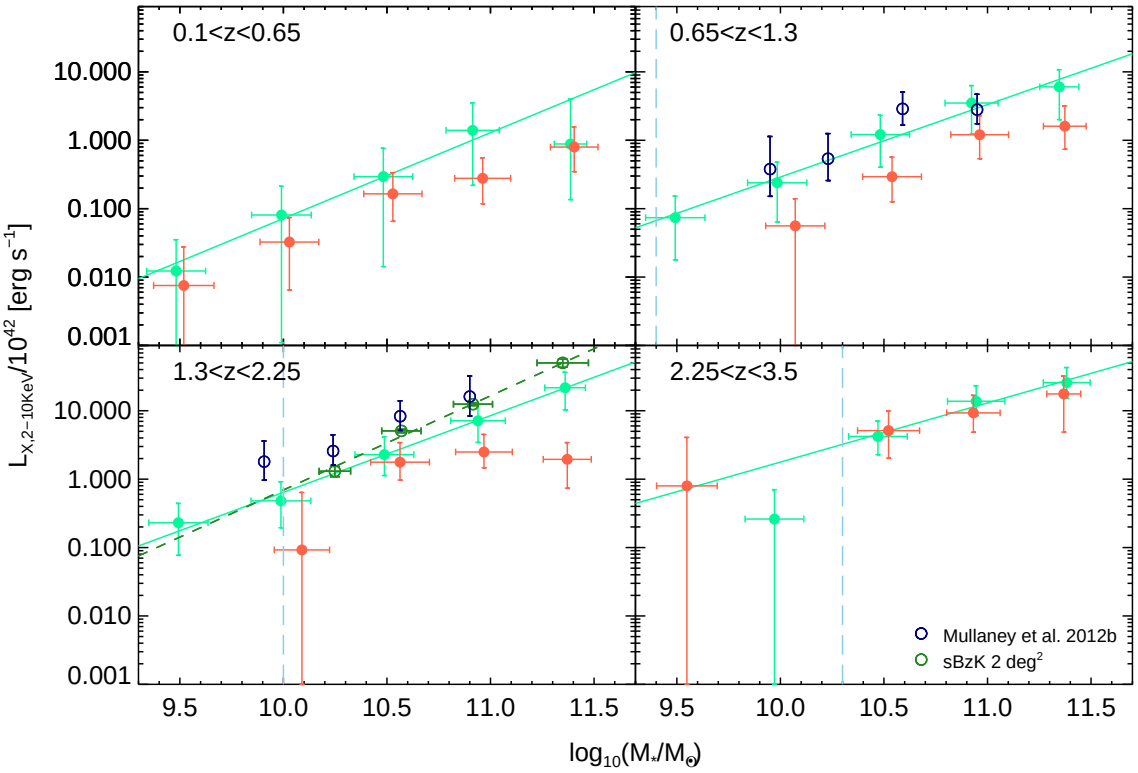

Figure 5.2: Stellar mass-average luminosity relation from our X-ray stacking analysis for COSMOS2015 sample after accounting for any host galaxy contribution. The sample is divided in main sequence (green), quiescent sources (red) and redshift bins. Horizontal error bars show the mass dispersion, vertical error bars show the 90% confidence interval. The green solid lines are the fit to our data (see table 5.4). Vertical light blue dashed lines show the mass completeness limit (90%) for each redshift bin from Laigle et al. (in prep.). We also report results from Mullaney et al. (2012b) (scaled to the same K correction adopted in this work) and our main sequence from Fig. 4.1. We display them in the closest redshift bins plots (Mullaney's are $0.5 < z < 1.5$ and $1.5 < z < 2.5$). Data in Mullaney et al. (2012b) are from GOODS-S field.

5.4 Star formation rate from stacking of PACS data

For the remaining part of the thesis we will focus on the star-forming sample, selected with the NUV-r/r-J criterion. We compute its SFR and then we will finally focus on the co-evolution of SF and BH accretion.

To obtain the SFR in the COSMOS2015 sample we stacked the Herschel data at the location of the galaxies. To this end, we split the SF sample into the same redshift and mass intervals as for the X-ray analysis, and stack all PACS-undetected in a residual 160μm map created by removing all PACS 160 µm detections with SNR$>$ 3 (stacking at 100 µm does not change our results). The stacking is performed using the IAS stacking library (Béthermin et al. 2010), PSF-fitting photometry, and applying an appropriate flux correction for faint, non-masked sources to the PACS stacks (Popesso et al. 2012). Using the formalism introduced by (Magnelli et al. 2009, eq. 3), that accounts both for detections and no-detections (analogous to eq. (4.1)), we then converted these stacked fluxes into bolometric luminosities $L_{\rm IR}$ by adopting an average K-correction (Chary &

Table 5.4: Fit parameters in the L_X plot (see Fig. 5.2) for a $\log[L_X] = m \times \log[M_*] + q$ law and in the BHAR/SFR ratio single plots (see Fig. 5.4) for a $\log[\mathrm{BHAR/SFR}] = m \times \log[M_*] + q$ law. All fits are performed above the mass completeness limit (dashed vertical lines in above figures).

Redshift	L_X		BHAR/SFR	
	m	q	m	q
$0.1 < z < 0.65$	1.04 ± 0.14	-11.4 ± 1.4	0.46 ± 0.12	-8.7 ± 1.3
$0.65 < z < 1.3$	1.04 ± 0.10	-10.9 ± 1.1	0.49 ± 0.10	-8.8 ± 1.1
$1.3 < z < 2.25$	1.11 ± 0.15	-11.3 ± 1.6	0.53 ± 0.15	-9.3 ± 1.6
$2.25 < z < 3.5$	0.87 ± 0.20	-8.4 ± 2.2	0.33 ± 0.20	-7.2 ± 0.3

Elbaz 2001) and then into SFR through the standard law of Kennicutt (1998), reported in eq (1.13).

The results of this procedure are presented in table 5.2. The obtained SFR-mass relations for all the redshift bins is shown in the top panel of Fig. 5.3. Here we find the already known Main Sequence in the SFR-M_* plane and its increase with redshift (see section 1.2).

The SF sample probably includes also starburst galaxies which, because of dust obscuration, are selected with the NUV-r/r-J criterion as MS galaxies (Rodighiero et al. 2014). These galaxies have a higher FIR luminosity, which may influence the SFR trend. However, it is known that their number density is about 2–3%, so we expect that their contribution should be very small and can be neglected in the overall budget (Rodighiero et al. 2011).

5.5 SFR vs. BHAR evolution

At this point we want to compare the evolution of the SF to that of the BH accretion. We use the X-ray luminosity of SFG to estimate the BHAR as in Mullaney et al. (2012b) and Rodighiero et al. (2015) using the relation

$$\mathrm{BHAR}(M_*, z) = \frac{(1-\epsilon) \cdot L_{\mathrm{bol}}(M_*, z)}{\epsilon c^2}, \tag{5.3}$$

where L_{bol} is the average AGN bolometric luminosity obtained as $L_{\mathrm{bol}} = 22.4 L_{\mathrm{X,2\text{–}10\ keV}}$ (i.e. using the median bolometric correction factor of a sample of local AGNs with $L_X = 10^{41-46}\,\mathrm{erg\,s^{-1}}$, from Vasudevan & Fabian (2007)). c is the speed of light in the vacuum and ϵ is the efficiency by which mass is converted into radiated energy via the accretion process. Here we assume $\epsilon = 0.1$ (e.g. Marconi et al. 2004), or that roughly 10% of the accreted rest-mass is converted into radiant energy, irrespective of M_{BH}.

In the central panel of Fig. 5.3 we show the BHAR-M_* relation for the four redshift intervals. A similar trend to that of the SFR (top panel) can be noticed, therefore to better compare them, we also show the BHAR to SFR ratio in the lower panel and in Fig. 5.4. This ratio shows an increasing trend with mass above the mass completeness limit (dashed vertical lines), and can also be seen in table 5.4. At all redshifts the slope is compatible with a constant value of $\alpha \sim 0.45$, so the scaling of the M_{BH}–M_* relation can be found considering that

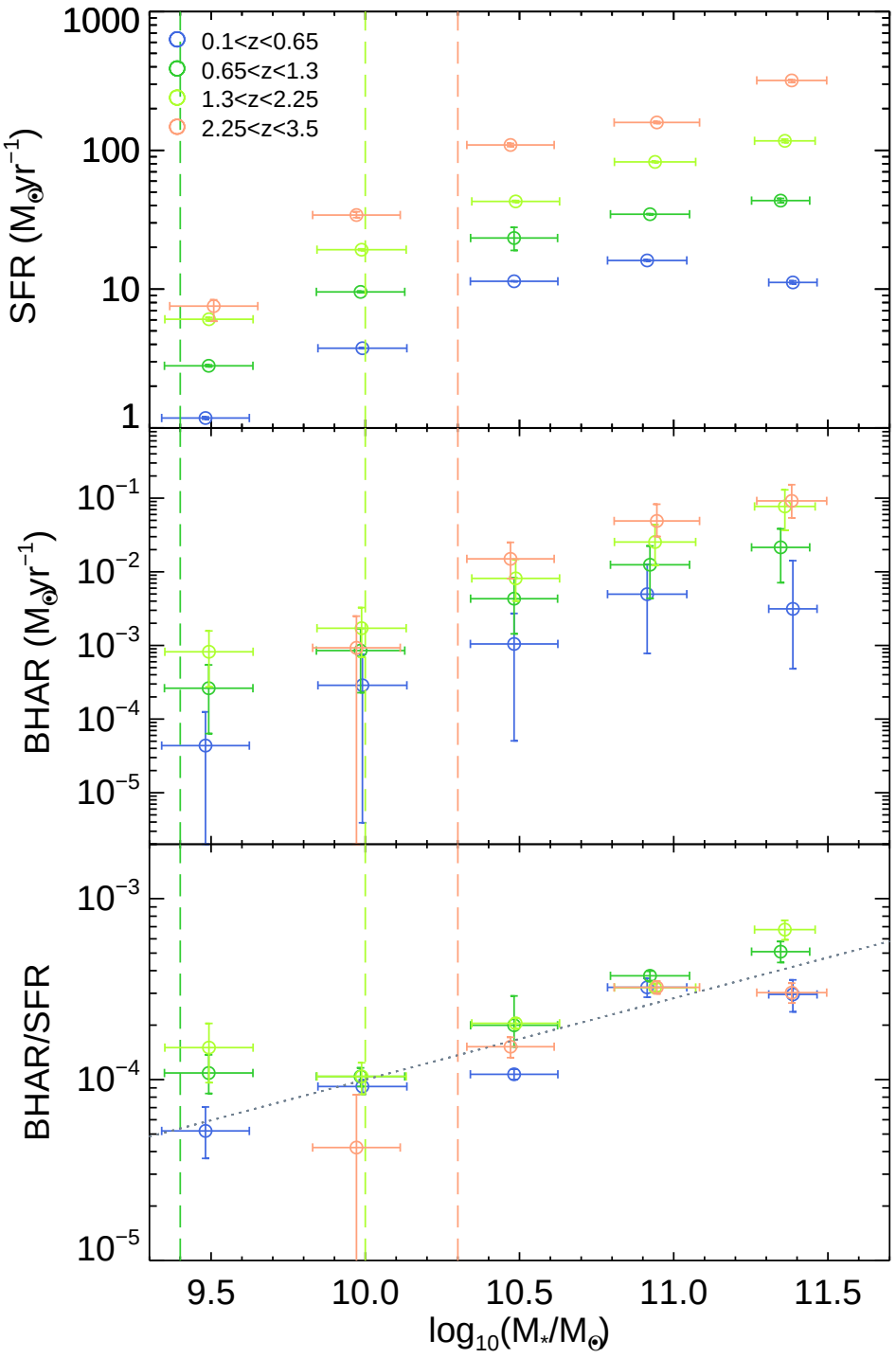

Figure 5.3: *Top panel* Average star formation rates vs. stellar mass for star-forming galaxies in our redshift bins for SFG. *Middle panel* Average X-ray luminosities of the SFG in our samples as in Fig. 5.2. *Bottom panel* Average BHAR to SFR ratio vs. stellar mass for our samples. The vertical dashed lines indicate the mass completeness limit for each redshift bin and follow the same color code as the data points. The grey dotted line is an average fit for all redshifts with equation $\log \frac{\mathrm{BHAR}}{\mathrm{SFR}} = 0.45(\log \mathrm{M}_* - 10) - 4$ and will be used in section 5.6 for the $\mathrm{M_{BH}}$ computation.

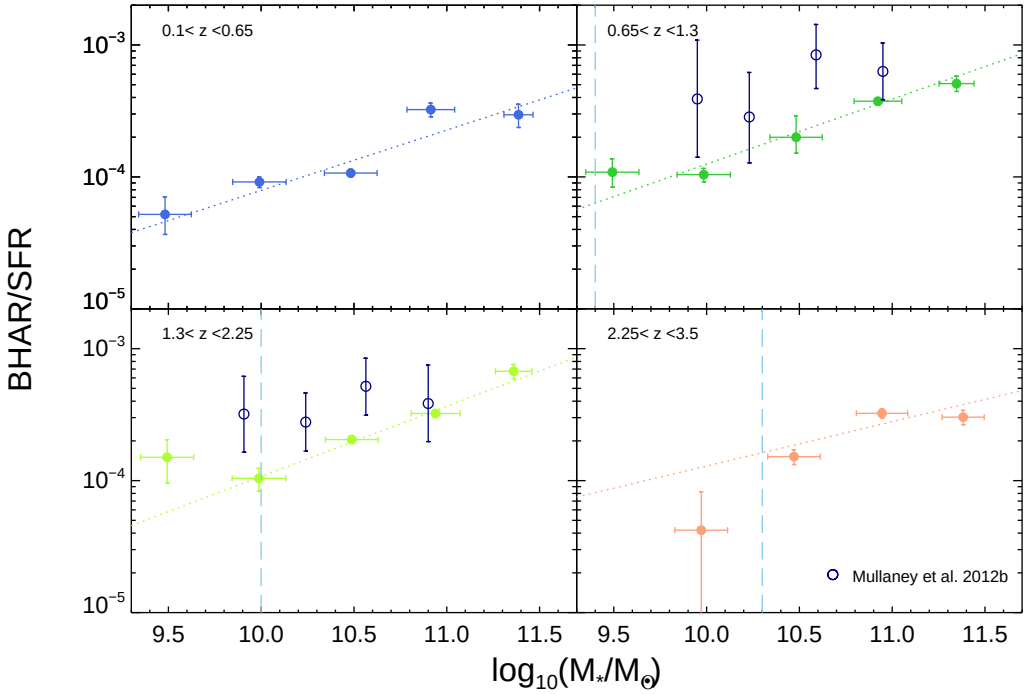

Figure 5.4: Same as bottom panel of Fig. 5.3 but with a plot for each redshift bin and with the best fit lines with parameters in table 5.4. We also report data points from Mullaney et al. (2012b) (navy circles) in the closest redshift bins.

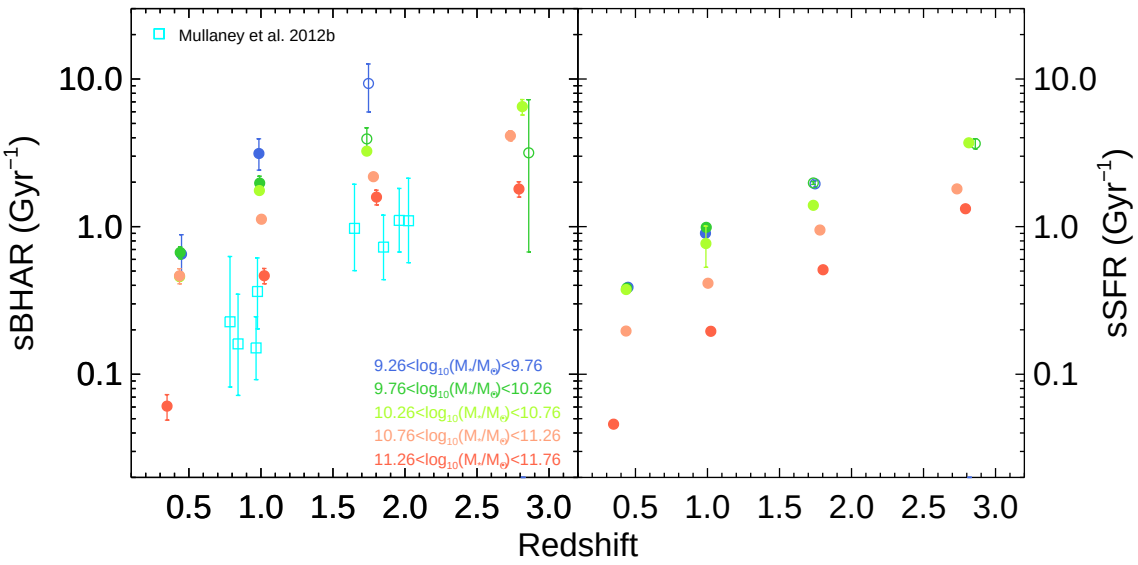

Figure 5.5: *Left panel* sBHAR (i.e. sBHAR=BHAR/M_{BH}, assuming $M_{BH} = \frac{10^{-8.5}}{1.45} M_*^{1.45}$) plotted as a function of redshift for our stellar mass and redshift bins. Open circles are data points below the mass completeness limit. We also report data points from (Mullaney et al. 2012b) (cyan open squares). Following Mullaney et al. (2012b) we have increased the sBHAR by a factor of two to account for missing AGNs, due to e.g. obscuration. *Right panel* sSFR (i.e. sSFR=SFR/M_*) as a function of redshift for our stellar mass and redshift bins.

$$\log \frac{\mathrm{BHAR}}{\mathrm{SFR}} = \log \frac{\dot{\mathrm{M}}_{\mathrm{BH}}}{\dot{\mathrm{M}}_*} = \log \frac{\partial \mathrm{M}_{\mathrm{BH}}}{\partial \mathrm{M}_*} \propto \alpha \cdot \log \mathrm{M}_* = \log \mathrm{M}_*^{\alpha}, \tag{5.4}$$

therefore

$$d\mathrm{M}_{\mathrm{BH}} \propto \mathrm{M}_*^{\alpha}\, d\mathrm{M}_* \tag{5.5}$$

and finally

$$\mathrm{M}_{\mathrm{BH}} \propto \frac{1}{1+\alpha}\, \mathrm{M}_*^{1+\alpha} = \frac{\mathrm{M}_*^{1.45}}{1.45} \tag{5.6}$$

which is valid only assuming that the growth rates of both stellar and BH mass are constant with time

$$\dot{\mathrm{M}}_{\mathrm{BH}} \simeq \mathrm{const}(t), \quad \dot{\mathrm{M}}_* \simeq \mathrm{const}(t). \tag{5.7}$$

5.6 sSFR vs. sBHAR evolution

Finally, we compare the average sSFR to the average sBHAR=BHAR/M_{BH}, in Fig. 5.5. To calculate the sSFR we use the data on table 5.2 while for the sBHAR, we take advantage of the growing trend of the ratio BHAR/SFR with M_*in the bottom panel of Fig. 5.3. There a best fit with equation:

$$\log \frac{\mathrm{BHAR}}{\mathrm{SFR}} = 0.45\,(\log \mathrm{M}_* - 10) - 4 \tag{5.8}$$

is shown, which has the average slope $\alpha = 0.45$ which all redshift bins are compatible with (table 5.4). With the considerations reported in eqs. (5.4) to (5.7) we can rewrite eq. (5.8) as

$$\mathrm{M}_{\mathrm{BH}} = \frac{10^{-4-10\cdot\alpha}}{1+\alpha}\, \mathrm{M}_*^{1+\alpha} = \frac{10^{-8.5}}{1.45}\, \mathrm{M}_*^{1.45}. \tag{5.9}$$

We estimate the sBHAR using this last equation for each of our mass and redshift bins and increase it by a factor of two to account for missing AGNs due to e.g. obscuration. The result of these computations is reported in Fig. 5.5 where data points from Mullaney et al. (2012b) are also reported as cyan open squares. The open circles are data points below the mass completeness limit.

5.7 Discussion

In this section we discuss and interpret the findings of this chapter in the context of current AGN/galaxy evolutionary scenarios. We find a less steep $\mathrm{L_X} - \mathrm{M}_*$ relation than previously

found with the *sBzK* selected sample (eq. 4.7). While in the first comparison the lower slope seemed to be compatible (section 5.1), in the following analysis this difference becomes pronounced and the results are not compatible any more (table 5.4). This difference could be due to, e.g. the different sample selection or to the higher fraction of stacked

sources in the COSMOS2015 sample, but only a further analysis will be able to explain this.

Our results show a robust $L_X - M_*$ correlation for SFG confirming its existence in all redshift bins. The slope of this relation obtained with the COSMOS2015 sample is independent of redshift and is compatible within the error bars with a constant value of ~ 1 (see table 5.4). This slope is less steep than the those with the BzK selected sample from Rodighiero et al. (2015) and in eq. (4.7). Also our first comparison showed a lower slope, even though it was still compatible with previous results (see section 5.1). Instead, in the following analysis this difference becomes pronounced and the results are not compatible any more (table 5.4). This difference could be due to, e.g. the different sample selection or to the higher fraction of stacked sources in the COSMOS2015 sample, but only a further analysis would be able to explain this (see chapter 6). Anyway we notice that our slope agrees with Mullaney et al. (2012b) (who found a slope of 0.86 ± 0.39—$z \sim 1$—and 1.05 ± 0.36—$z \sim 2$).

Studying figure 5.2 we notice that in the highest redshift bin, the X-ray luminosities of quiescent/quenched galaxies overlap those of the SFG. This may suggest a decoupling of the SF and BH activity at the early cosmic epochs. Nevertheless, we do not see an L_X trend with redshift for the quiescent population, so this could be due to a higher uncertainty of the data points. To discriminate between these alternatives a deeper investigation would be required.

In the $1.3 < z < 2.25$ redshift bin (again, figure 5.2) we notice that the quiescent highest mass data point shows a decreasing trend, while in Fig. 4.1 we had found an increasing trend. In the $sBzK$ sample the detections fraction was 4.2% while now it is only 2.4%, and also the massive early type (therefore quiescent) galaxies are usually associated to radio galaxies which have an accretion rate much lower than the Eddington limit, so it is possible that they have an intrinsically lower X-ray luminosity. For the $0.65 < z < 1.3$ redshift bin we notice that our data points are in good agreement with results from Mullaney et al. (2012b), while in $1.3 < z < 2.25$ ours are a bit less luminous. This could simply be due to our lower redshift interval.

The result in eq. (5.6) may seem to be in contrast with the local $M_{BH}/M_* \simeq M_{BH}/M_{bulge}$ linear ($\alpha = 0$) relation (Kormendy et al. 2011) and in contrast with Mullaney et al. (2012b) who also find a linear relation (see navy circles in Fig. 5.4). This can be explained by considering that the local linear M_{BH}/M_{bulge} relation is valid only for spheroids, i.e. elliptical galaxies and bulges. The COSMOS2015 catalog does not include any morphological information, therefore we are considering in our analysis disk and irregular galaxies too, which are the predominant component a the lower masses. These galaxies have on average a smaller bulge and a less active BH, so they bias our result by producing lower M_{BH}/M_* ratio at lower masses, i.e. a steeper slope $1 + \alpha$.

We relate the trends of BHAR and SFR with M_* and redshift (figs. 5.3, 5.4, 5.5) to gas content and the redshift evolution of the gas fraction:

$$f_{gas} = \frac{M_{gas}}{M_{gas} + M_*} \tag{5.10}$$

which represents the ratio between total (i.e. molecular + neutral) gas mass and total baryonic mass of a galaxy. Several studies have investigated the evolution of f_{gas} in main-sequence galaxies from the local Universe to $z \sim 1$ (Leroy et al. 2008; Geach et al. 2011; Saintonge et al. 2011b,a, 2012), at $z \sim 1.5 - 2$ (Daddi et al. 2010b; Tacconi et al. 2010, 2013), finding a strong ($f_{gas} \propto (1+z)^2$) evolution up to $z \sim 2$ and a *plateau* at higher

redshift ($z \sim 3$ Magdis et al. 2013). Direct CO observations presented by (Daddi et al. 2010b; Tacconi et al. 2010, 2013) provided first empirical evidence for the existence of very large gas fractions in $z \sim 1-2$ main-sequence galaxies, with mass in gas even larger than the mass in stars (i.e. f_{gas} >0.5). These gas rich systems have also higher SFRs (Daddi et al. 2010a; Genzel et al. 2010)), as expected from the Schmidt–Kennicutt relation (Schmidt 1959; Kennicutt 1998). This gas-dominated phase in z ∼1–2 main-sequence galaxies is also reflected in a difference in morphology. Indeed, while local main-sequence galaxies are preferentially regular disks, their $z \sim 2$ analogs show a larger fraction of irregular morphologies and/or clumpy disks (e.g. Elmegreen et al. 2007; Förster Schreiber et al. 2009; Kocevski et al. 2012), which make them potentially more efficient in funnelling the cold gas inward onto the SMBH (Bournaud et al. 2011). In the light of the above-mentioned literature, it is justified to expect that the relationship between average BHAR and SFR becomes stronger with increasing redshift, where the fraction of actively star-forming gas becomes larger. Vito et al. (2014) found that AGN hosts are significantly more gas rich than inactive galaxies, at a given M_* and redshift, suggesting that the probability that a SMBH is active is strongly connected to the amount of cold gas supply. This supports M_{gas} as the key ingredient to explain the mutual evolution of star formation and AGN accretion activity (e.g. Santini et al. 2012a; Mullaney et al. 2012b; Rosario et al. 2013).

In the right panel of Fig. 5.5 we find the well known evolution of the specific SFR with mass for our data (e.g. Whitaker et al. 2014; Madau & Dickinson 2014; Bauer et al. 2005), while in the left panel we show our new results for the sBHAR. Both sBHAR and sSFR have a clear increasing trend with redshift and with decreasing stellar mass, and the normalisation of the sBHAR is higher than that of the sSFR. The explanation we give for the decline with cosmic time is the already discussed decrease in the amount of cold gas in galaxies which seems to feed both phenomena in a similar way.

The trend found in mass (see Fig. 5.5) can be explained in terms of the downsizing effect, for both galaxy (e.g. Madau & Dickinson 2014) and BH (e.g. Alexander & Hickox 2012) growth: all over the investigated redshift range we find for the higher masses a more pronounced decrease in both sSFR and sBHAR than for the low mass galaxies, implying that high-mass objects increased the bulk of their BH and stellar mass at early cosmic epoch, while low-mass galaxies have had more steady activity down to the present epoch. Both activities follow a similar trend in mass and this result is quite at variance with Mullaney et al. (2012b).

The higher normalisation of the BHAR can be explained taking into account the mass-doubling time-scale: the inverse of the sSFR (sBHAR) is often interpreted as a physical time-scale for the formation of the stellar population (the accretion into a BH) and is equivalent to the time it would take for the stellar mass of a galaxy (the BH mass) to double. The fact that the sBHAR is always higher that the sSFR for the relative mass and redshift bins implies that the mass doubling time of a BH is shorter that of the galaxy, again suggesting that the time scales of the BH accretion process are shorter than those of SF.

The apparent disagreement with the data from (Mullaney et al. 2012b) (see Fig. 5.5) can be explained in terms of our lower BH masses, consequence of the lower values of our BHAR/SFR ratio (see Fig. 5.4). These make our sBHAR have higher values, and—as already said—reflect the higher efficiency of the BH accretion process, contrary to the equal growth speed found by Mullaney et al. (2012b).

Chapter 6

Future prospects

This thesis work brings new insights on the co-evolution of SFG and SMBH. However these preliminary results need to be deepened increasing the data sample and can still give us much more information, for example by means of comparison with models.

A first and easy check on the stability of the results would be to derive dust corrections to compute the intrinsic L_X from the Hardness Ratio as a function of redshift and mass (instead of adopting an average K-correction).

A second check to perform is the effect of the color selection. In fact the NUV-r/r-J criterion may include quiescent galaxies in the SF sample or vice versa. Therefore it would be useful to perform different color selections, or a selection based on morphological criteria and study how they influence the sample luminosity.

A third check could be to extend our stacked analysis on deeper Chandra surveys (GOODS-S and GOODS-N) to see how the fraction of detected sources influences the average L_X derived from the combination of stacked and detected sources and to better constrain our results in the highest redshift bin.

It would also be very interesting to extend our sample including a selection of starburst galaxies at all redshifts from the PEP catalog, as done at $z \sim 2$ in chapter 4, and study their behaviour and evolution.

We should also include a detailed analysis of the passive/quenched population, that has not been performed in this thesis.

Last but not least we plan to compare our results with hydrodinamical simulations of galaxies withfeedback from a central BH (Volonteri et al. 2015; Hopkins & Quataert 2011; Di Matteo et al. 2005) and also with a physical model based on analytic approximations (e.g. Lapi et al. 2014) to find new physical constraints on the evolution of galaxies.

Bibliography

Aird, J., Coil, A. L., Moustakas, J., et al. 2012, ApJ, 746, 90

Alexander, D. M., & Hickox, R. C. 2012, New A Rev., 56, 93

Alexander, D. M., Smail, I., Bauer, F. E., et al. 2005, Nature, 434, 738

Antonucci, R. 1993, ARA&A, 31, 473

Antonucci, R. R. J. 1984, ApJ, 278, 499

Antonucci, R. R. J., & Miller, J. S. 1985, ApJ, 297, 621

Arav, N., Barlow, T. A., Laor, A., Sargent, W. L. W., & Blandford, R. D. 1998, MNRAS, 297, 990

Arnouts, S., Walcher, C. J., Le Fèvre, O., et al. 2007, A&A, 476, 137

Avni, Y., & Tananbaum, H. 1986, ApJ, 305, 83

Azadi, M., Aird, J., Coil, A., et al. 2014, ArXiv e-prints, arXiv:1407.1975

Bauer, A. E., Drory, N., Hill, G. J., & Feulner, G. 2005, ApJ, 621, L89

Beckmann, V., & Shrader, C. R. 2012, Active Galactic Nuclei (Wiley-VCH)

Berta, S., Magnelli, B., Lutz, D., et al. 2010, A&A, 518, L30

Berta, S., Magnelli, B., Nordon, R., et al. 2011, A&A, 532, A49

Berta, S., Lutz, D., Santini, P., et al. 2013, A&A, 551, A100

Béthermin, M., Dole, H., Beelen, A., & Aussel, H. 2010, A&A, 512, A78

Béthermin, M., Wang, L., Doré, O., et al. 2013, A&A, 557, A66

Boissier, S., & Prantzos, N. 2009, A&A, 503, 137

Bongiorno, A., Merloni, A., Brusa, M., et al. 2012, MNRAS, 427, 3103

Booth, C. M., & Schaye, J. 2009, MNRAS, 398, 53

Bournaud, F., Dekel, A., Teyssier, R., et al. 2011, ApJ, 741, L33

Bower, R. G., Benson, A. J., Malbon, R., et al. 2006, MNRAS, 370, 645

Boyle, B. J., & Terlevich, R. J. 1998, MNRAS, 293, L49

Brandt, W. N., & Alexander, D. M. 2015, A&A Rev., 23, 1

Brandt, W. N., Laor, A., & Wills, B. J. 2000, ApJ, 528, 637

Brinchmann, J., Charlot, S., White, S. D. M., et al. 2004, MNRAS, 351, 1151

Bruzual, G., & Charlot, S. 2003, MNRAS, 344, 1000

Bryant, P. M., & Scoville, N. Z. 1999, AJ, 117, 2632

Calzetti, D., Armus, L., Bohlin, R. C., et al. 2000, ApJ, 533, 682

Calzetti, D., Harris, J., Gallagher, III, J. S., et al. 2004, AJ, 127, 1405

Cano-Díaz, M., Maiolino, R., Marconi, A., et al. 2012, A&A, 537, L8

Cardelli, J. A., Clayton, G. C., & Mathis, J. S. 1989, ApJ, 345, 245

Chabrier, G. 2003, PASP, 115, 763

Chary, R., & Elbaz, D. 2001, ApJ, 556, 562

Cimatti, A., Daddi, E., Mignoli, M., et al. 2002a, A&A, 381, L68

Cimatti, A., Mignoli, M., Daddi, E., et al. 2002b, A&A, 392, 395

Cimatti, A., Pozzetti, L., Mignoli, M., et al. 2002c, A&A, 391, L1

Cisternas, M., Jahnke, K., Inskip, K. J., et al. 2011, ApJ, 726, 57

Civano, F. M., & Chandra COSMOS Legacy Survey Team. 2013, in AAS/High Energy Astrophysics Division, Vol. 13, AAS/High Energy Astrophysics Division, 116.18

Clavel, J., Wamsteker, W., & Glass, I. S. 1989, ApJ, 337, 236

Comastri, A. 2004, in Astrophysics and Space Science Library, Vol. 308, Supermassive Black Holes in the Distant Universe, ed. A. J. Barger, 245

Condon, J. J. 1992, ARA&A, 30, 575

Croton, D. J., Springel, V., White, S. D. M., et al. 2006, MNRAS, 365, 11

da Cunha, E., Charlot, S., & Elbaz, D. 2008, MNRAS, 388, 1595

Daddi, E., Cimatti, A., Renzini, A., et al. 2004, ApJ, 617, 746

Daddi, E., Cimatti, A., Broadhurst, T., et al. 2002, A&A, 384, L1

Daddi, E., Dickinson, M., Chary, R., et al. 2005, ApJ, 631, L13

Daddi, E., Dickinson, M., Morrison, G., et al. 2007, ApJ, 670, 156

Daddi, E., Elbaz, D., Walter, F., et al. 2010a, ApJ, 714, L118

Daddi, E., Bournaud, F., Walter, F., et al. 2010b, ApJ, 713, 686

Dekel, A., & Birnboim, Y. 2006, MNRAS, 368, 2

Dekel, A., Birnboim, Y., Engel, G., et al. 2009, Nature, 457, 451

Delvecchio, I., Gruppioni, C., Pozzi, F., et al. 2014, MNRAS, 439, 2736

Delvecchio, I., Lutz, D., Berta, S., et al. 2015, ArXiv e-prints, arXiv:1501.07602

Di Matteo, T., Springel, V., & Hernquist, L. 2005, Nature, 433, 604

Dickinson, M., Papovich, C., Ferguson, H. C., & Budavári, T. 2003, ApJ, 587, 25

Done, C. 2010, ArXiv e-prints, arXiv:1008.2287

Downes, D., & Solomon, P. M. 1998, ApJ, 507, 615

Doyle, D., Pilbratt, G., & Tauber, J. 2009, IEEE Proceedings, 97, 1403

Dunne, L., Ivison, R. J., Maddox, S., et al. 2009, MNRAS, 394, 3

Elbaz, D., Daddi, E., Le Borgne, D., et al. 2007, A&A, 468, 33

Elbaz, D., Dickinson, M., Hwang, H. S., et al. 2011, A&A, 533, A119

Elmegreen, D. M., Elmegreen, B. G., Ravindranath, S., & Coe, D. A. 2007, ApJ, 658, 763

Elvis, M., Maccacaro, T., Wilson, A. S., et al. 1978, MNRAS, 183, 129

Elvis, M., Civano, F., Vignali, C., et al. 2009, ApJS, 184, 158

Engelbracht, C. W., Gordon, K. D., Rieke, G. H., et al. 2005, ApJ, 628, L29

Engelbracht, C. W., Rieke, G. H., Gordon, K. D., et al. 2008, ApJ, 678, 804

Erb, D. K., Steidel, C. C., Shapley, A. E., et al. 2006, ApJ, 647, 128

Fabian, A. C. 2006, Astronomische Nachrichten, 327, 943

Farrah, D., Afonso, J., Efstathiou, A., et al. 2003, MNRAS, 343, 585

Farrah, D., Urrutia, T., Lacy, M., et al. 2012, ApJ, 745, 178

Fath, E. A. 1909, Lick Observatory Bulletin, 5, 71

Ferrarese, L. 2002, ApJ, 578, 90

Fontana, A., Pozzetti, L., Donnarumma, I., et al. 2004, A&A, 424, 23

Förster Schreiber, N. M., Genzel, R., Bouché, N., et al. 2009, ApJ, 706, 1364

Franceschini, A., Hasinger, G., Miyaji, T., & Malquori, D. 1999, MNRAS, 310, L5

García-Burillo, S., Combes, F., Schinnerer, E., Boone, F., & Hunt, L. K. 2005, A&A, 441, 1011

Garmire, G. P., Bautz, M. W., Ford, P. G., Nousek, J. A., & Ricker, Jr., G. R. 2003, in Society of Photo-Optical Instrumentation Engineers (SPIE) Conference Series, Vol. 4851, X-Ray and Gamma-Ray Telescopes and Instruments for Astronomy., ed. J. E. Truemper & H. D. Tananbaum, 28–44

Geach, J. E., Smail, I., Moran, S. M., et al. 2011, ApJ, 730, L19

Gebhardt, K., Bender, R., Bower, G., et al. 2000, ApJ, 539, L13

Genzel, R., Lutz, D., Sturm, E., et al. 1998, ApJ, 498, 579

Genzel, R., Tacconi, L. J., Gracia-Carpio, J., et al. 2010, MNRAS, 407, 2091

Georgantopoulos, I. 2013, International Journal of Modern Physics Conference Series, 23, 1

George, I. M., Turner, T. J., Netzer, H., et al. 1998, ApJS, 114, 73

George, I. M., Turner, T. J., Yaqoob, T., et al. 2000, ApJ, 531, 52

Giacconi, R., Zirm, A., Wang, J., et al. 2002, ApJS, 139, 369

Gibson, R. R., Brandt, W. N., & Schneider, D. P. 2008, ApJ, 685, 773

Gilfanov, M., & Merloni, A. 2014, Space Sci. Rev., 183, 121

Granato, G. L., Silva, L., Danese, L., de Zotti, G., & Bressan, A. 2004, in Multiwavelength AGN Surveys, ed. R. Mújica & R. Maiolino, 379–384

Gruppioni, C., Pozzi, F., Rodighiero, G., et al. 2013, MNRAS, 432, 23

Gültekin, K., Cackett, E. M., Miller, J. M., et al. 2009, ApJ, 706, 404

Haardt, F., & Maraschi, L. 1993, ApJ, 413, 507

Häring-Neumayer, N., Cappellari, M., Rix, H.-W., et al. 2006, ApJ, 643, 226

Harrison, F. A., Craig, W. W., Christensen, F. E., et al. 2013, ApJ, 770, 103

Harwit, M., & Pacini, F. 1975, ApJ, 200, L127

Hickox, R. C., Mullaney, J. R., Alexander, D. M., et al. 2014, ApJ, 782, 9

Hickox, R. C., Jones, C., Forman, W. R., et al. 2009, ApJ, 696, 891

Hong, S., Calzetti, D., Dopita, M. A., et al. 2011, ApJ, 731, 45

Hopkins, A. M., & Beacom, J. F. 2006, ApJ, 651, 142

Hopkins, P. F., Hernquist, L., Cox, T. J., & Kereš, D. 2008, ApJS, 175, 356

Hopkins, P. F., Hernquist, L., Cox, T. J., Robertson, B., & Krause, E. 2007, ApJ, 669, 67

Hopkins, P. F., Hickox, R., Quataert, E., & Hernquist, L. 2009, MNRAS, 398, 333

Hopkins, P. F., & Quataert, E. 2011, MNRAS, 415, 1027

Ilbert, O., Capak, P., Salvato, M., et al. 2009, ApJ, 690, 1236

Ilbert, O., Salvato, M., Le Floc'h, E., et al. 2010, ApJ, 709, 644

Ilbert, O., McCracken, H. J., Le Fèvre, O., et al. 2013, A&A, 556, A55

Ishibashi, W., & Courvoisier, T. J.-L. 2011, A&A, 525, A118

Jansen, F., Lumb, D., Altieri, B., et al. 2001, A&A, 365, L1

Karim, A., Schinnerer, E., Martínez-Sansigre, A., et al. 2011, ApJ, 730, 61

Kellermann, K. I., Sramek, R. A., Schmidt, M., Green, R. F., & Shaffer, D. B. 1994, AJ, 108, 1163

Kennicutt, R. C., & Evans, N. J. 2012, ARA&A, 50, 531

Kennicutt, Jr., R. C. 1998, ARA&A, 36, 189

Kocevski, D. D., Faber, S. M., Mozena, M., et al. 2012, ApJ, 744, 148

Kormendy, J., Bender, R., & Cornell, M. E. 2011, Nature, 469, 374

Krolik, J. H. 1999, Nature, 398, 678

Kroupa, P. 2001, MNRAS, 322, 231

Laor, A., Fiore, F., Elvis, M., Wilkes, B. J., & McDowell, J. C. 1997, ApJ, 477, 93

Lapi, A., Raimundo, S., Aversa, R., et al. 2014, ApJ, 782, 69

Leroy, A. K., Walter, F., Brinks, E., et al. 2008, AJ, 136, 2782

Lilly, S. J., Carollo, C. M., Pipino, A., Renzini, A., & Peng, Y. 2013, ApJ, 772, 119

Lilly, S. J., Le Fevre, O., Hammer, F., & Crampton, D. 1996, ApJ, 460, L1

Lutz, D., Poglitsch, A., Altieri, B., et al. 2011, A&A, 532, A90

Maccacaro, T., Gioia, I. M., Wolter, A., Zamorani, G., & Stocke, J. T. 1988, ApJ, 326, 680

Madau, P., & Dickinson, M. 2014, ARA&A, 52, 415

Madau, P., Ferguson, H. C., Dickinson, M. E., et al. 1996, MNRAS, 283, 1388

Magdis, G. E., Daddi, E., Béthermin, M., et al. 2012, ApJ, 760, 6

Magdis, G. E., Rigopoulou, D., Helou, G., et al. 2013, A&A, 558, A136

Magnelli, B., Elbaz, D., Chary, R. R., et al. 2009, A&A, 496, 57

Magorrian, J., Tremaine, S., Richstone, D., et al. 1998, AJ, 115, 2285

Maraston, C. 2005, MNRAS, 362, 799

Maraston, C., Strömbäck, G., Thomas, D., Wake, D. A., & Nichol, R. C. 2009, MNRAS, 394, L107

Marconi, A., & Hunt, L. K. 2003, ApJ, 589, L21

Marconi, A., Pastorini, G., Pacini, F., et al. 2006, A&A, 448, 921

Marconi, A., Risaliti, G., Gilli, R., et al. 2004, MNRAS, 351, 169

Martin, D. C., Wyder, T. K., Schiminovich, D., et al. 2007, ApJS, 173, 342

McCracken, H. J., Capak, P., Salvato, M., et al. 2010, ApJ, 708, 202

Merloni, A., & Heinz, S. 2008, MNRAS, 388, 1011

Mignoli, M., Cimatti, A., Zamorani, G., et al. 2005, A&A, 437, 883

Miller, B. P., Brandt, W. N., Schneider, D. P., et al. 2011, ApJ, 726, 20

Mineo, T., Fiore, F., Laor, A., et al. 2000, A&A, 359, 471

Moran, E. C., Filippenko, A. V., & Chornock, R. 2002, ApJ, 579, L71

Mullaney, J. R., Pannella, M., Daddi, E., et al. 2012a, MNRAS, 419, 95

Mullaney, J. R., Daddi, E., Béthermin, M., et al. 2012b, ApJ, 753, L30

Mushotzky, R. 2004, in Astrophysics and Space Science Library, Vol. 308, Supermassive Black Holes in the Distant Universe, ed. A. J. Barger, 53

Mushotzky, R. F., Done, C., & Pounds, K. A. 1993, ARA&A, 31, 717

Noeske, K. G., Faber, S. M., Weiner, B. J., et al. 2007a, ApJ, 660, L47

Noeske, K. G., Weiner, B. J., Faber, S. M., et al. 2007b, ApJ, 660, L43

Osterbrock, D. E. 1981, ApJ, 249, 462

Padmanabhan, T. 2002, Theoretical Astrophysics - Volume 3, Galaxies and Cosmology

Page, M. J., Symeonidis, M., Vieira, J. D., et al. 2012, Nature, 485, 213

Papovich, C., Rudnick, G., Le Floc'h, E., et al. 2007, ApJ, 668, 45

Peng, Y.-j., Lilly, S. J., Renzini, A., & Carollo, M. 2014, ApJ, 790, 95

Peng, Y.-j., Lilly, S. J., Kovač, K., et al. 2010, ApJ, 721, 193

Perola, G. C., Matt, G., Cappi, M., et al. 2002, A&A, 389, 802

Peterson, B. M. 1997, The Observatory, 117, 314

Pilbratt, G. L., Riedinger, J. R., Passvogel, T., et al. 2010, A&A, 518, L1

Pope, E. C. D., Mendel, J. T., & Shabala, S. S. 2012, MNRAS, 419, 50

Popesso, P., Magnelli, B., Buttiglione, S., et al. 2012, ArXiv e-prints, arXiv:1211.4257

Pozzetti, L., Cimatti, A., Zamorani, G., et al. 2003, A&A, 402, 837

Reddy, N., Dickinson, M., Elbaz, D., et al. 2012, ApJ, 744, 154

Reddy, N. A., Steidel, C. C., Fadda, D., et al. 2006, ApJ, 644, 792

Reynolds, C. S., & Nowak, M. A. 2003, Phys. Rep., 377, 389

Rieke, G. H., & Lebofsky, M. J. 1979, ARA&A, 17, 477

Rodighiero, G., Vaccari, M., Franceschini, A., et al. 2010, A&A, 515, A8

Rodighiero, G., Daddi, E., Baronchelli, I., et al. 2011, ApJ, 739, L40

Rodighiero, G., Renzini, A., Daddi, E., et al. 2014, MNRAS, 443, 19

Rodighiero, G., Brusa, M., Daddi, E., et al. 2015, ApJ, 800, L10

Rosario, D. J., Santini, P., Lutz, D., et al. 2012, A&A, 545, A45

Rosario, D. J., Mozena, M., Wuyts, S., et al. 2013, ApJ, 763, 59

Rowan-Robinson, M. 1977, ApJ, 213, 635

—. 2001, ApJ, 549, 745

Rudnick, G., Rix, H.-W., Franx, M., et al. 2003, ApJ, 599, 847

Saintonge, A., Kauffmann, G., Kramer, C., et al. 2011a, MNRAS, 415, 32

Saintonge, A., Kauffmann, G., Wang, J., et al. 2011b, MNRAS, 415, 61

Saintonge, A., Tacconi, L. J., Fabello, S., et al. 2012, ApJ, 758, 73

Salpeter, E. E. 1955, ApJ, 121, 161

Sanders, D. B., & Mirabel, I. F. 1996, ARA&A, 34, 749

Sanders, D. B., Soifer, B. T., Elias, J. H., et al. 1988, ApJ, 325, 74

Santini, P., Fontana, A., Grazian, A., et al. 2009, A&A, 504, 751

Santini, P., Rosario, D. J., Shao, L., et al. 2012a, A&A, 540, A109

Santini, P., Fontana, A., Grazian, A., et al. 2012b, A&A, 538, A33

Sargent, M. T., Béthermin, M., Daddi, E., & Elbaz, D. 2012, ApJ, 747, L31

Schmidt, M. 1959, ApJ, 129, 243

Schnittman, J. D., & Krolik, J. H. 2013, ApJ, 777, 11

Schreiber, C., Pannella, M., Elbaz, D., et al. 2015, A&A, 575, A74

Schweitzer, M., Lutz, D., Sturm, E., et al. 2006, ApJ, 649, 79

Scoville, N., Aussel, H., Brusa, M., et al. 2007, ApJS, 172, 1

Shakura, N. I., & Sunyaev, R. A. 1973, A&A, 24, 337

Shankar, F., Weinberg, D. H., & Miralda-Escudé, J. 2009, ApJ, 690, 20

Shao, L., Lutz, D., Nordon, R., et al. 2010, A&A, 518, L26

Shields, G. A. 1978, Nature, 272, 706

Silverman, J. D., Lamareille, F., Maier, C., et al. 2009, ApJ, 696, 396

Smith, J. D. T., Draine, B. T., Dale, D. A., et al. 2007, ApJ, 656, 770

Springel, V., Di Matteo, T., & Hernquist, L. 2005, MNRAS, 361, 776

Stanley, F., Harrison, C. M., Alexander, D. M., et al. 2015, ArXiv e-prints, arXiv:1502.07756

Stringer, M., Cole, S., Frenk, C. S., & Stark, D. P. 2011, MNRAS, 414, 1927

Strüder, L., Briel, U., Dennerl, K., et al. 2001, A&A, 365, L18

Tacconi, L. J., Genzel, R., Neri, R., et al. 2010, Nature, 463, 781

Tacconi, L. J., Neri, R., Genzel, R., et al. 2013, ApJ, 768, 74

Treister, E., Schawinski, K., Urry, C. M., & Simmons, B. D. 2012, ApJ, 758, L39

Turner, M. J. L., Abbey, A., Arnaud, M., et al. 2001, A&A, 365, L27

Turner, T. J., & Miller, L. 2009, A&A Rev., 17, 47

Urry, C. M., & Padovani, P. 1995, PASP, 107, 803

Vasudevan, R. V., & Fabian, A. C. 2007, MNRAS, 381, 1235

Vattakunnel, S., Tozzi, P., Matteucci, F., et al. 2012, MNRAS, 420, 2190

Vito, F., Maiolino, R., Santini, P., et al. 2014, MNRAS, 441, 1059

Volonteri, M., Capelo, P. R., Netzer, H., et al. 2015, MNRAS, 449, 1470

Weedman, D. W., Feldman, F. R., Balzano, V. A., et al. 1981, ApJ, 248, 105

Weisskopf, M. C., Tananbaum, H. D., Van Speybroeck, L. P., & O'Dell, S. L. 2000, in Society of Photo-Optical Instrumentation Engineers (SPIE) Conference Series, Vol. 4012, X-Ray Optics, Instruments, and Missions III, ed. J. E. Truemper & B. Aschenbach, 2–16

Whitaker, K. E., van Dokkum, P. G., Brammer, G., & Franx, M. 2012, ApJ, 754, L29

Whitaker, K. E., Franx, M., Leja, J., et al. 2014, ApJ, 795, 104

Williams, R. J., Quadri, R. F., Franx, M., van Dokkum, P., & Labbé, I. 2009, ApJ, 691, 1879

Wilms, J., Allen, A., & McCray, R. 2000, ApJ, 542, 914

Worrall, D. M. 2009, A&A Rev., 17, 1

Zamorani, G., Henry, J. P., Maccacaro, T., et al. 1981, ApJ, 245, 357